

University of Nevada, Reno

HYBRID SYSTEMS: COLD ATOMS COUPLED TO MICRO MECHANICAL  
OSCILLATORS

A Dissertation Submitted in Partial Fulfillment  
of the Requirements for the Degree of Doctor of Philosophy in  
Physics

by

Cris A Montoya Monge

Dr. Andrew Geraci / Dissertation Advisor

December 2017

© 2017 Cris A Montoya Monge

ALL RIGHTS RESERVED

UNIVERSITY  
OF NEVADA  
RENO

THE GRADUATE SCHOOL

We recommend that the dissertation prepared  
under our supervision by

CRIS A MONTOYA MONGE

entitled

HYBRID SYSTEMS: COLD ATOMS COUPLED TO MICRO MECHANICAL  
OSCILLATORS

be accepted in partial fulfillment of the  
requirements for the degree of

DOCTOR OF PHILOSOPHY

Andrew Geraci, Ph.D. – Advisor

Jonathan Weinstein, Ph.D. – Committee Member

Andrei Derevianko, Ph.D. – Committee Member

Aaron Covington, Ph.D. – Committee Member

Jonathan Baker, Ph.D. – Graduate School Representative

David W. Zeh, Ph.D. – Dean, Graduate School

December 2017

## ABSTRACT

Micro mechanical oscillators can serve as probes in precision measurements, as transducers to mediate photon-phonon interactions, and when functionalized with magnetic material, as tools to manipulate spins in quantum systems. This dissertation includes two projects where the interactions between cold atoms and mechanical oscillators are studied.

In one of the experiments, we have manipulated the Zeeman state of magnetically trapped Rubidium atoms with a magnetic micro cantilever [1]. The results show a spatially localized effect produced by the cantilever that agrees with Landau-Zener theory. In the future, such a scalable system with highly localized interactions and the potential for single-spin sensitivity could be useful for applications in quantum information science or quantum simulation.

In a second experiment, work is in progress to couple a sample of optically trapped Rubidium atoms to a levitated nanosphere via an optical lattice [2]. This coupling enables the cooling of the center-of-mass motion of the nanosphere by laser cooling the atoms. In this system, the atoms are trapped in the optical lattice while the sphere is levitated in a separate vacuum chamber by a single-beam optical tweezer. Theoretical analysis of such a system has determined that cooling the center-of-mass motion of the sphere to its quantum ground state is possible, even when starting at room temperature, due to the excellent environmental decoupling achievable in this setup. Nanospheres cooled to the quantum regime can provide new tests of quantum behavior at mesoscopic scales and have novel applications in precision sensing.



To my parents,  
Maritza Monge Bonilla  
and  
Cristóbal Montoya Marín

## ACKNOWLEDGEMENTS

During my senior year in high school, my friend Juan Diego Acuña Castillo, one of the smartest people I've ever met, told me he was reading some physics theory the night before, which he did not get to understand. He asked me to please explain it to him in a few years, after I'd become a physicist. Juan Diego and I, both went to the University of Costa Rica, and we remained friends during college; together we summited Cerro Chirripó, Costa Rica's highest mountain. A week before moving to Reno for grad school, I had a farewell party at the bar we frequented. Little did we know, that was the last time we would see Juan Diego, as a month later he unexpectedly passed away. I never got to explain him that theory he had read, probably because we both forgot about it. For some reason though, during my time as a grad student, every time I needed extra motivation to continue; the promise of learning physics so I could explain that obscure theory to my friend came to mind. The moral of this story is we don't know the effect our actions, or our words, might have on others, or even on ourselves. In my case, some silly promise in high school kept me going throughout my Ph.D. and I have Juan Diego to thank for that.

David Atherton and I started working at the lab on the same day, our first task involved scavenging for chairs and benches around the physics building. Although David worked in a different project, we made a good team by supporting each other in our projects. Later, Gambhir Ranjit joined us and added experience to the team. I appreciate all of their help, and their friendship.

Our lab has had great undergraduate students work with us, some of which I've had the honor of collaborating with: Kirsten Casey, Jason Lim, Jacob Faucett, and William Eom. However, two undergrads in particular worked closely with me on a daily basis: Jose and Apryl. At the time he started working in our lab, Jose Valencia was a sophomore. We worked together on the atom-cantilever experiment,

and by the time he was a senior I talked him into changing his name to Jose "Master of collimation" Valencia. Having him around the lab was great, I could count on him to help me with anything from laser alignment to taking a coffee break. Apryl Witherspoon worked closely with me during the design stage of the bead experiment. Together we figured out the procedure for polishing the drive masses for the gravity project, and later she took charge of all of the polishing. This is how she got the royal title: Queen of polishing. Apryl, along with labmembers Isabella Rodriguez, and Chloe Lohmeyer provided me with great emotional support during my last months as a grad student. I consider myself lucky to have them as friends.

During the last years, I often had to mix two-part epoxy for which I needed a scale. Since our lab didn't have a precise scale, the solution was going to the chemistry department. I'd like to thank the labmembers of Ana de Bettencourt-Dias' research group for kindly allowing us to use their scale and even to borrow a hot plate a few times! In particular I'd like to thank Alejandro Gracia-Nava, Rodney Tigaa, and Jorge Monteiro, who later turned into my soccer buddies.

I'd also like to acknowledge the work of Joel Desormeau who trained me and assisted me with the use of the SEM. Wade Cline and Carl Davison, their machining experience was very important throughout the development of these experiments. Marvin Wakefield, Mercy Balderrama, and the student workers at the physics office; who were always on top of any paperwork and administrative tasks needed. I'd also like to express gratitude to the physics faculty for sharing their knowledge and passion for physics with me, and the members of my committee for agreeing to all the work that comes with being in a PhD committee.

A large portion of this dissertation was written during late nights at Starbucks. During these productive evenings, Priscilla Acosta provided the necessary distraction via text message whenever I had the urge of some outside contact, the smiles she

provided me were of great help, and highly appreciated. Kathrine Wright also seemed to appear in my life at right moment, she has been incredibly helpful to the point of helping me out with one of the figures on this dissertation! Some of the writing was also done together with Elena Atanasiu who, at the time, was also writing her dissertation. It seems like it was yesterday that Elena and I went together to the new grad student orientation! I thank her for her support and friendship. Marcela Loria and I, enjoyed most of our grad student life next to each other, it was great having her at my side.

I'd like to credit my parents Cristóbal and Maritza because I know I can always count on them, my sisters Itzi and Laura for their empathy, my nieces for brightening my life, and my grandmother Nelly for her prayers.

I'd also like to acknowledge the mentorship provided by Dr. Andrew Geraci, I'm grateful our paths crossed, and that I've had the opportunity to learn from him. John Kitching has collaborated with both of the projects presented on this dissertation via phone meetings, his insights have been very useful, and the impact he has had on this dissertation is enormous. Matt Eardley's graduate work also influenced my work as a graduate student, having access to his notes and presentation slides has been of great help.

To summarize, thank you to all the network of people who have in many ways helped me survive my Ph.D. journey.

November, 2017

”Nadie llega a ningún lado sin la ayuda de otro”

”Nobody gets anywhere without the help of another”

Franklin Chang-Diaz

## Citations to Previously Published Work

Portions of this dissertation have appeared previously in the following publications:

- G. Ranjit, C. Montoya, and A. A. Geraci, “Cold atoms as a coolant for levitated optomechanical systems,” *Physical Review A*, vol. 91, p. 013416, Jan. 2015
- C. Montoya, J. Valencia, A. A. Geraci, M. Eardley, J. Moreland, L. Hollberg, and J. Kitching, “Resonant interaction of trapped cold atoms with a magnetic cantilever tip,” *Physical Review A*, vol. 91, p. 063835, June 2015

## TABLE OF CONTENTS

Abstract . . . . .	i
Dedication . . . . .	ii
Acknowledgements . . . . .	iii
Citations to Previously Published Work . . . . .	vii
Table of Contents . . . . .	viii
List of Tables . . . . .	xi
List of Figures . . . . .	xii
 1 Introduction . . . . .	 1
1.1 Experiment 1: Magnetic Coupling . . . . .	6
1.2 Experiment 2: Optical Coupling . . . . .	6
 2 Trapping and Cooling of Atoms . . . . .	 8
2.1 Cooling of Atoms . . . . .	8
2.1.1 Doppler Cooling Limit . . . . .	10
2.1.2 Polarization Gradient Cooling . . . . .	11
2.2 Trapping of Atoms . . . . .	12
2.3 Magneto-Optical Traps . . . . .	14
2.4 Atom Chips . . . . .	15
 3 Magnetic Coupling of Atomic Zeeman State to Cantilever . . . . .	 18
3.1 Rubidium . . . . .	18
3.1.1 Energy Levels . . . . .	18
3.2 Laser System . . . . .	21
3.2.1 Saturated Absorption Spectroscopy . . . . .	22
3.2.2 Optical Layout . . . . .	26
3.3 Imaging . . . . .	33
3.3.1 Fluorescence Imaging . . . . .	34
3.3.2 Absorption Imaging . . . . .	35
3.4 Magnetic Coils . . . . .	36
3.5 Atom Chip . . . . .	38
3.5.1 Cantilever Layer . . . . .	40
3.5.2 U-trap Layer . . . . .	48
3.5.3 Guiding / P-trap Layer . . . . .	51
3.6 Diagnostics . . . . .	53
3.6.1 MOT Temperature . . . . .	54
3.6.2 MOT Population . . . . .	56
3.6.3 Magnetic Trap Lifetime . . . . .	58
3.7 Landau-Zener Theory . . . . .	59
3.8 Magnetic Coupling of Atoms to Cantilever . . . . .	60
3.8.1 Zeeman-State Transitions . . . . .	61
3.8.2 Zeeman-State Transition Detection . . . . .	62

3.9	Results . . . . .	63
3.10	Conclusions and Future Directions . . . . .	67
4	Optical Traps . . . . .	70
4.1	Gaussian Optics . . . . .	70
4.2	Dipole Force . . . . .	72
4.2.1	Ray Optics Visualization . . . . .	73
4.2.2	Dipole Force Theory . . . . .	74
4.2.3	Dipole Force for Dielectric Spheres . . . . .	75
4.2.4	Dipole Force for Atoms . . . . .	79
4.3	Optical Lattice . . . . .	80
5	Sympathetic Cooling of Nanospheres with Atoms . . . . .	82
5.1	Proposed/Ongoing Experiment . . . . .	83
5.1.1	Atoms-Bead Coupling . . . . .	84
5.2	Coupling to the Lattice . . . . .	85
5.2.1	Atom-Light Coupling . . . . .	85
5.2.2	Sphere-Light Coupling . . . . .	86
5.3	Cooling Terms . . . . .	87
5.4	Heating Terms . . . . .	88
5.4.1	Momentum Diffusion of the Atoms . . . . .	88
5.4.2	Momentum Diffusion of the Sphere . . . . .	88
5.5	Steady State . . . . .	90
5.6	Advantages of Sympathetic Cooling . . . . .	92
5.7	Projected Results . . . . .	93
6	Sphere's Experimental Setup . . . . .	96
6.1	Trapped Atoms in an Optical Lattice . . . . .	96
6.1.1	Optical Layout . . . . .	96
6.1.2	Trapped Atoms Characterization . . . . .	98
6.2	Vacuum Chamber . . . . .	100
6.2.1	V-Block . . . . .	101
6.2.2	Optical Cavity . . . . .	104
6.3	Bead Launching . . . . .	107
6.3.1	Van der Waals Force . . . . .	108
6.3.2	Diving Board Launcher . . . . .	109
6.3.3	Trapping of Beads . . . . .	111
6.4	Bead Imaging . . . . .	114
6.4.1	Live Imaging . . . . .	114
6.4.2	Bead Spectra . . . . .	117
6.5	Current State of the Experiment and Next Steps . . . . .	122
6.5.1	Parametric Feedback Cooling . . . . .	122
7	Future Outlook . . . . .	125



Appendices	128
A Labview Program used in magnetic coupling experiment	128
A.1 State Table . . . . .	128
A.2 Time Table . . . . .	129
A.3 Voltage Table . . . . .	129
B Minimum detectable force of a harmonic oscillator	133
B.0.1 Cantilever Response . . . . .	133
B.0.2 Thermal Noise Limitation . . . . .	134
C Mathematica code used to numerically calculate field from magnet	135
D Optical Cavity and V-block Design	137
E Nanofabrication of Cantilever and Drive Mass for Gravity Experiment	140
E.1 Cantilever Fabrication . . . . .	140
E.1.1 Cantilever fabrication steps . . . . .	143
E.2 Drive Mass Fabrication . . . . .	145
E.2.1 Drive Mass Fabrication steps . . . . .	145
F Electroplating and Polishing of Drive Mass	148
F.1 Electroplating . . . . .	148
F.1.1 Preparing the Samples . . . . .	148
F.1.2 Deposition Time Calculation . . . . .	149
F.1.3 Materials . . . . .	150
F.1.4 Procedure . . . . .	151
F.2 Polishing of Drive Mass . . . . .	153
F.2.1 Materials . . . . .	153
F.2.2 Procedure . . . . .	154
Bibliography	159

## LIST OF TABLES

3.1	Coil construction details . . . . .	37
3.2	Magnetic bias coils . . . . .	38
3.3	Anti-Helmholtz coils . . . . .	38
3.4	Thermo-elastic constants for silicon . . . . .	50
3.5	Experimental measurements of cloud after molasses cooling. . . . .	57
3.6	Example values for highly sensitive cantilever . . . . .	68
4.1	Bead experiment parameters . . . . .	79
5.1	Sympathetic cooling of bead experimental parameters . . . . .	92
5.2	Sympathetic cooling of bead experimental derived parameters . . . . .	93
5.3	Sympathetic cooling of bead measured parameters . . . . .	95
5.4	Sympathetic cooling of bead derived parameters from measurements . . . . .	95
6.1	Optical lattice trap characterization . . . . .	100
6.2	Focal length of optical tweezer lens . . . . .	117
E.1	Fabrication steps for the front side of the cantilever . . . . .	143
E.2	Fabrication steps for the back side of the cantilever . . . . .	144
E.3	Final cantilever fabrication step . . . . .	144
E.4	Fabrication steps for the front side of drive mass . . . . .	145
E.5	Fabrication steps for the back side of drive mass . . . . .	146
E.6	Final mass fabrication steps . . . . .	146

## LIST OF FIGURES

1.1	Optomechanical devices . . . . .	4
2.1	Doppler cooling of atoms . . . . .	9
2.2	Polarization gradient cooling . . . . .	11
2.3	Anti Helmholtz coils . . . . .	14
2.4	Energy diagram of an atom in a quadrupole trap . . . . .	15
2.5	Magnetic field produced by a wire and a bias homogeneous field . . .	17
3.1	$^{87}\text{Rb}$ D2 transition energy diagram . . . . .	20
3.2	Saturated absorption spectroscopy signal . . . . .	22
3.3	Saturated spectroscopy optical layout . . . . .	23
3.4	Transition spectra of $^{87}\text{Rb}$ D2 line . . . . .	25
3.5	Repump laser optical layout . . . . .	27
3.6	Acousto-optical modulator double-pass layout . . . . .	28
3.7	Laser beams preparation layout . . . . .	29
3.8	Imaging and optical pumping beams layout . . . . .	31
3.9	Chamber vicinity layout . . . . .	32
3.10	Optical layout of imaging beams on atom chip . . . . .	32
3.11	Imaging of atoms . . . . .	33
3.12	Fluorescence image of MOT . . . . .	35
3.13	Absorption image of molasses cooled atoms . . . . .	36
3.14	Anti-Helmholtz coils . . . . .	37
3.15	Atom chip's wire fabrication . . . . .	39
3.16	Cantilever layer assembly . . . . .	40
3.17	Diagram for calculating magnetic field from a current loop at a distant point . . . . .	41
3.18	SEM image of cantilever . . . . .	43
3.19	Layout of cantilever resonance measurement system . . . . .	45
3.20	Cantilever resonance . . . . .	46
3.21	Cantilever tip displacement measurement layout . . . . .	47
3.22	Atom chip layers . . . . .	49
3.23	Atom chip architectures . . . . .	49
3.24	Side view of U-trap . . . . .	50
3.25	P-trap rotation . . . . .	51
3.26	Time progression of the guiding trap . . . . .	53
3.27	Guide trap transport . . . . .	54
3.28	Molasses-cooled cloud temperature . . . . .	55
3.29	Atom cloud lineout on North-South axis . . . . .	57
3.30	P-trap lifetime . . . . .	59
3.31	Diagram of the atom-cantilever experiment . . . . .	61
3.32	Energy diagram of $m_F$ magnetic sublevels in $^{87}\text{Rb}$ ground state . . .	62

3.33	Atom preparation flow chart . . . . .	64
3.34	Trap population after interacting with cantilever . . . . .	65
3.35	Trap population after varying time of interaction with the cantilever . . . . .	66
3.36	Thermal-noise limited force sensitivity of proposed cantilever . . . . .	69
4.1	Intensity profile of a Gaussian beam . . . . .	71
4.2	Spot size of a Gaussian beam . . . . .	71
4.3	Ray optics diagram of scattering and gradient forces . . . . .	73
4.4	Scattering and gradient forces on axial direction . . . . .	76
4.5	Bead trap depth plots . . . . .	77
4.6	Optical lattice representation . . . . .	80
5.1	Experimental setup of sympathetic cooling of bead experiment . . . . .	83
5.2	Nanosphere in a node of the optical lattice . . . . .	84
5.3	Phonon number of the sphere . . . . .	90
5.4	Strong coupling dynamics plot . . . . .	91
5.5	U-MOT temperature measured after various molasses cooling times. . . . .	94
6.1	Optical layout of lattice beam . . . . .	97
6.2	Front image of optical lattice . . . . .	99
6.3	Side image of optical lattice . . . . .	100
6.4	Bead vacuum chamber design . . . . .	101
6.5	Bead vacuum chamber picture . . . . .	102
6.6	V-block holder for the trap lenses . . . . .	102
6.7	Optical layout inside bead chamber . . . . .	103
6.8	Beam width measurement plots . . . . .	104
6.9	Beam width evolution near waist . . . . .	105
6.10	Optical cavity . . . . .	105
6.11	Optical cavity diagram . . . . .	107
6.12	Diving board assembly diagram . . . . .	109
6.13	Piezo driver circuit diagram . . . . .	111
6.14	Trap potential as a function of bead size . . . . .	112
6.15	SEM images of launched spheres . . . . .	112
6.16	Picture of trapped sphere using 1596 nm light . . . . .	114
6.17	Picture of trapped sphere using 632 nm light . . . . .	115
6.18	Segmented photodiode diagram . . . . .	117
6.19	Diagram of quadrant photodetector circuit . . . . .	119
6.20	Imaging of light scattered by bead . . . . .	119
6.21	Bead spectra . . . . .	121
6.22	Parametric feedback cooling diagram . . . . .	123
6.23	Parametric feedback cooling setup diagram . . . . .	124
7.1	Bead interferometry diagram . . . . .	126
A.1	Sequence state table (part 1) . . . . .	130

A.2	Sequence state table (part 2) . . . . .	131
A.3	Sequence voltage table . . . . .	132
E.1	Short-range force experiment . . . . .	141
E.2	Cantilever for gravity experiment . . . . .	141
E.3	Drive mass before gold coat . . . . .	147
E.4	Gold coated drive mass . . . . .	147
F.1	SEM images of drive mass . . . . .	149
F.2	Electroplating setup . . . . .	151
F.3	Drive mass representation . . . . .	154
F.4	SEM image of drive mass . . . . .	158

## CHAPTER 1

### INTRODUCTION

Classical mechanics, the field that studies the motion of objects in the macroscopic world, has been widely studied for hundreds of years. In the last century, quantum mechanics has been studied on objects at the atomic and molecular scale, yet a question to be determined is what occurs at the boundary between these two regimes, the so called mesoscopic domain. At what point do the quantum mechanical effects takeover the classical mechanics effects? [3, 4, 5, 6, 7], and viceversa. Because of their simplicity, mechanical oscillators have been studied to understand both classical and quantum mechanics [8, 9, 10], which makes them a promising candidate to study the boundary between the two [11]. Cooling mechanical oscillators enables the study of quantum mechanical phenomena at large scales. Recently, oscillators cooled to their lowest energy state, or ground state, was demonstrated [12, 13, 14]. This important milestone represent the first step towards using these devices in fields like quantum metrology.

As a tool for probing and manipulating mechanical oscillators, the force from radiation pressure can be used. Although radiation pressure has been a subject of study since it was first predicted by Maxwell, since the construction of the first laser by Maiman in 1960 [15], and the subsequent advent of laser technology, research involving radiation pressure has rapidly increased. In 1970, Ashkin [16] proposed using radiation pressure to hold and manipulate micron-sized particles. This lead to the demonstration of optical tweezers, and eventually to the optical atom trap in 1986 [17], which along with the observation of magnetically trapped neutral atoms [18], started the field of laser cooling. In 1997, the Nobel prize was awarded to Chu, Cohen-Tannoudji, and Phillips "for development of methods to cool and trap atoms

with laser light” [19]. Laser cooling enabled the creation of Bose-Einstein condensates [20] which also led to a Nobel prize in 2001 to Cornell, Ketterle, and Wieman. Many more applications have been possible thanks to laser cooling, microwave [21] and optical [22] atomic clocks probably being the most well known.

Recently, the field of optomechanics has emerged to probe and study the interaction between light and mechanical motion. In particular, manipulation of the center-of-mass motion of mechanical oscillators through radiation pressure [9] and cooling these oscillators to their ground state, has become one of the goals of the field. Observation of photon shot noise, which causes a random backaction force on optical measurements has also become a major goal in the field [23], and it has been recently observed in a membrane resonator in a cavity [24]. The study of quantum superposition in mesoscopic objects, for applications in information science and precision metrology, has become more relevant as these mechanical oscillators are cooled to their quantum mechanical ground state [4].

The first approaches to single-phonon control have been made possible through cryogenic cooling [12] and cavity optomechanics, a field that pairs mechanical oscillators to optical or microwave cavities [25]. Development of gravitational wave antennas at the Laser Interferometer Gravitational Wave Detector Observatory (LIGO) in the 1980’s led to the understanding of cavity optomechanical systems. These gravitational wave detectors are kilometer-long interferometers with mirrors of several kilograms of mass on the ends, forming an optical cavity. Precise measurements of the changes in the position of these mirrors was predicted to be needed to detect gravitational waves [26]. An other approach studied was to precisely measure the end-to-end vibrations of a massive cylinder inside a microwave cavity [27]. Both of these approaches created the challenge of manipulating macroscopic objects at their quantum limit using

electromagnetic radiation [25] and raised the question of the role of quantum noise in these measurements [28, 29].

Experimentally, many aspects of cavity optomechanics and optomechanical coupling have been demonstrated recently. For example, optical feedback cooling was first demonstrated in 1999 by cooling the Brownian motion of a mirror on a mechanical oscillator on a high-finesse optical cavity via the radiation pressure of a laser reflected on the mirror [30]; in 2007 the fundamental mode of a cantilever was cooled to its base temperature of 2.9 mK starting at cryogenic temperatures by active feedback produced by reflecting a laser from the tip of the cantilever into an optical interferometer [31]; in 2006 Kawamura and Kanegae, reported cooling a cantilever to the minimum vibration amplitude by feedback cooling, using a Michelson interferometer starting at room temperature [32]. In 2005, radiation pressure instability [33] was observed in a micro-toroidal cavity where the optical modes of a cavity were coupled to the mechanical modes of a mirror [34, 35]. This phenomena occurs when an optical cavity is driven out of resonance due to the forces from circulating radiation [36]. Cooling of micromirrors has since been observed using this effect [37, 38]. In 2013, observation of radiation pressure shot noise and optomechanical squeezing of light was reported [24].

With advancing technology in nanofabrication, optomechanical coupling has been proposed and demonstrated through a wide range of mechanical oscillators [25], including membranes inside of a cavity [40, 41, 42], where the resonance frequency of the cavity is modulated by the membrane's position, and membranes coupled to a nearby cloud of atoms via Casimir-Polder forces [43]; nanorods inside an optical cavity [44]; nano-oscillators coupled to a microdisk cavity in which flexural oscillations of the nano-oscillator are monitored by studying the intensity modulations it causes on



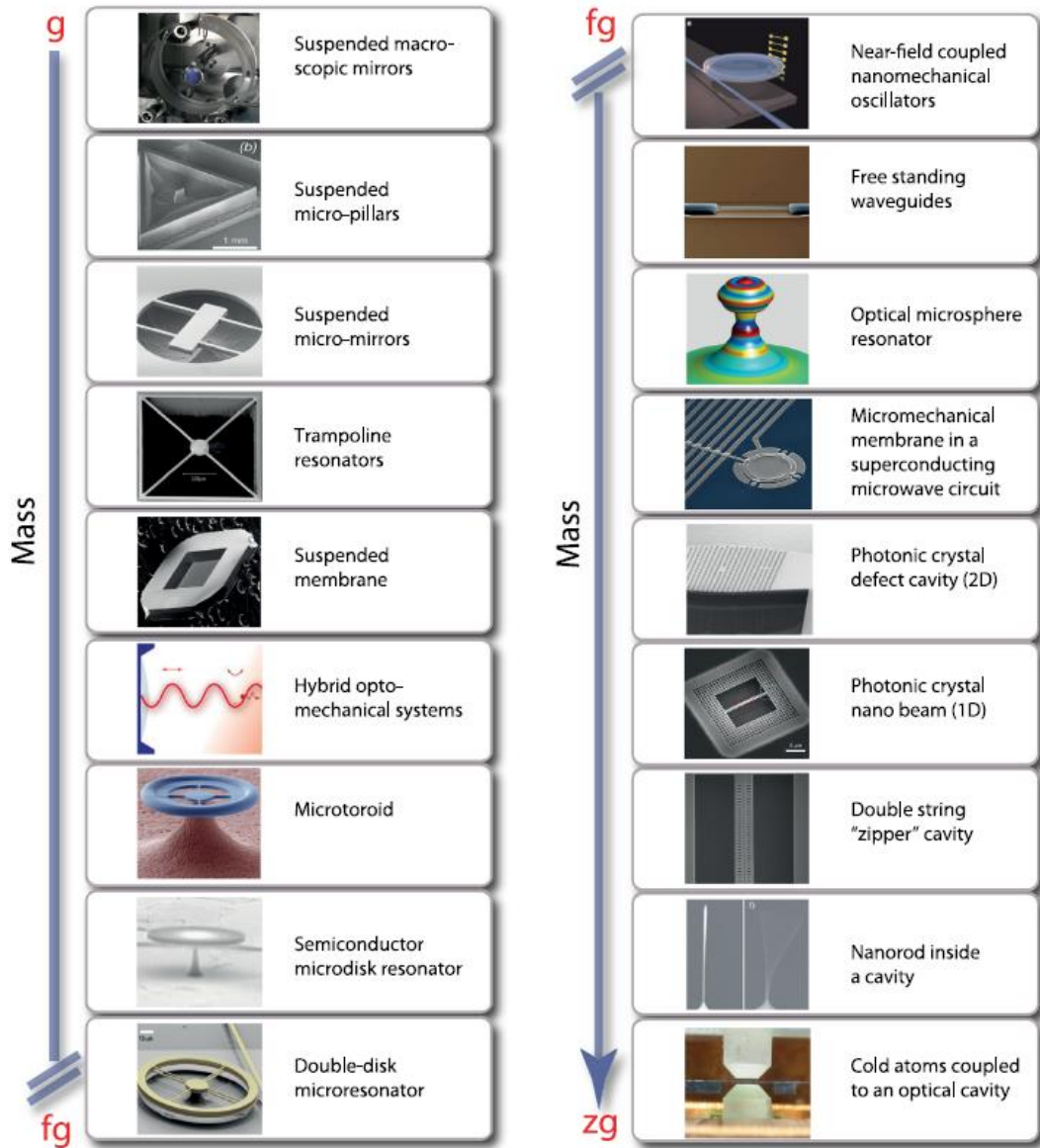


Figure 1.1: (Figure reproduced from ref. [39].) Illustrations of various optomechanical devices. Pictures from: N. Mavalvala, A. Heidmann, M. Aspelmeyer, D. Bouwmeester, J. Harris, P. Treutlein, T. J. Kippenberg, I. Favero, M. Lipson, T. J. Kippenberg/E. Weig/J. Kotthaus, H. Tang, K. Vahala/T. Carmon, J. Teufel/K. Lehnert, I. Robert, O. Painter, O. Painter, I. Favero/E. Weig/K. Karrai, and D. Stamper-Kurn.

the nearby cavity [45]; cantilevers coupled to a microdisk, where the displacements in the cantilever are transduced to frequency changes in the optical microdisk [46, 47]; cantilevers coupled to a Bose-Einstein condensate, where oscillations of the cantilever are coupled to mechanical modes of the BEC [48]; toroidal resonators that support optical whispering-gallery modes, which are closed circular waves trapped inside a dielectric by total internal reflection [49], and whispering-gallery modes coupled to the mechanical radial modes of a toroid [50]; levitated particles, where a levitated silica sphere is cavity cooled [51], laser feedback cooled silica spheres used to develop precise sensors [52], and levitated nanodiamonds with nitrogen-vacancy centers (NV center) to study quantum superpositions of the center-of-mass motion, using induced spin-optomechanical coupling [53].

As mentioned previously, ground state cooling of mechanical modes of oscillators has been possible via laser cooling [14], sideband cooling [13], and cryogenically through dilution refrigeration [12]. Alternative methods, such as sympathetic cooling [40], are currently under study as they may offer advantages over other methods.

The long coherence times of cold atoms has made coupling them to mechanical oscillators an attractive research avenue. Optomechanical systems can be coupled to both the external and the internal degrees of freedom of atoms, which might enable ground-state cooling outside the resolved sideband regime [54, 55], and establishing Einstein-Podolsky-Rosen entanglement [56]. Cold atoms optically coupled to a mechanical oscillator has been proposed to develop a quantum force sensor that beats the standard quantum limit [57], and magnetically coupling of atoms to a resonator has been performed with possible applications in high resolution microscopy [58]. Also, coupling the two systems enables the study of both; for example, the oscillator can be used to probe the atoms and the atoms can be used to cool the center of mass

motions of the oscillator, as in ref. [59].

In this dissertation two projects involving coupling of cold atoms to mechanical oscillators are discussed. In the first project, cold atoms were magnetically coupled to a micro-fabricated cantilever. In the second ongoing project, the cold atoms will be optically coupled to a levitated silica nanosphere.

## 1.1 Experiment 1: Magnetic Coupling

Microcantilevers have high spatial resolution [58] and can even have single spin force sensitivity [10]. This makes them a promising candidate to probe and manipulate atomic spin states for applications in quantum computing.

In our experiment, we trap a sample of Rubidium 87 atoms with the magnetic field produced by an atom chip. The cloud of atoms is transported near the tip of a cantilever which has a magnet on its tip. The oscillatory magnetic field produced by the magnet induces Zeeman state transitions in the atoms causing them to fall out of the trap. The effect of the cantilever is therefore observed as the trapped atom population decays when the cantilever is driven on resonance with the Larmor precession frequency of the atoms.

## 1.2 Experiment 2: Optical Coupling

Ground state cooling of a mechanical oscillator can enable the study of quantum mechanical properties in larger objects, and of coupling mechanical oscillators to other quantum mechanical systems, which allows quantum control of the system [12].

In our setup, a nanosphere acts as a mechanical oscillator. This nanosphere is optically levitated by a tightly focused beam forming an optical tweezer. In a separate chamber, a sample of Rubidium atoms is trapped in an optical lattice. The optical lattice that traps the atoms is formed by a laser beam that strikes the atoms, then strikes the nanosphere and is then reflected back onto itself by the back mirror of an optical cavity in which the sphere is located. The lattice provides the coupling between the sphere and the atoms. As the atoms move away from the equilibrium position, a redistribution of photons produces a change in the intensity of the laser striking the sphere, therefore applying a force on the sphere. As the sphere moves away from its equilibrium position, the phase of the laser exiting the cavity changes, which in turn shifts the equilibrium position of the atoms. The coupling of the nanosphere to the atoms allows the cooling of the center of mass motion of the sphere when the atoms are cooled with well known techniques like molasses cooling. Moreover, if the atom cooling is turned off, the dynamics of the warming bead can be studied. Calculations predict that this experimental setup can be used to cool the vibrational mode of the sphere down to its quantum ground state, a goal that has been recently achieved in macroscopic objects, but not yet observed in levitated systems like the one we propose.

## CHAPTER 2

### TRAPPING AND COOLING OF ATOMS

In both of the projects discussed in this dissertation, a sample of cold Rubidium atoms is used. Two simultaneous processes must be done to produce the sample: trapping and cooling of the atoms.

#### 2.1 Cooling of Atoms

The first observation of acceleration due to the forces of radiation pressure from a laser, were reported in 1970 [16]. In his paper, Ashkin proposes extending the idea to atoms and molecules, to accelerate, trap or separate them with the use of lasers. Photons carries momentum  $\hbar k$ , where  $k$  is the wavenumber. When an atom absorbs a photon, it receives a momentum impulse. If the atom is moving against the radiation, this momentum impulse slows the atom. The energy gained from absorbing the photon is stored by going to an excited state [60]. When the radiation scattering force is velocity dependent, repeated absorptions of photons can be used to reduce the kinetic energy of atoms [61, 62].

Reducing the kinetic energy of atoms through radiation pressure is possible via Doppler cooling. In this technique, a pair of counter-propagating laser beams strike the atoms. The laser is slightly red detuned from the the atomic resonance. Due to the Doppler effect, from the reference frame of the atoms, photons traveling opposite to the atoms are perceived on resonance (figure 2.1). Photons traveling in the same direction as the atoms are perceived as further red detuned. The atoms will preferentially absorb photons traveling in the direction opposing their movement, receiving a change in momentum,  $\Delta p = \hbar/\lambda$  for every photon scattered, where  $\lambda$  is the laser's

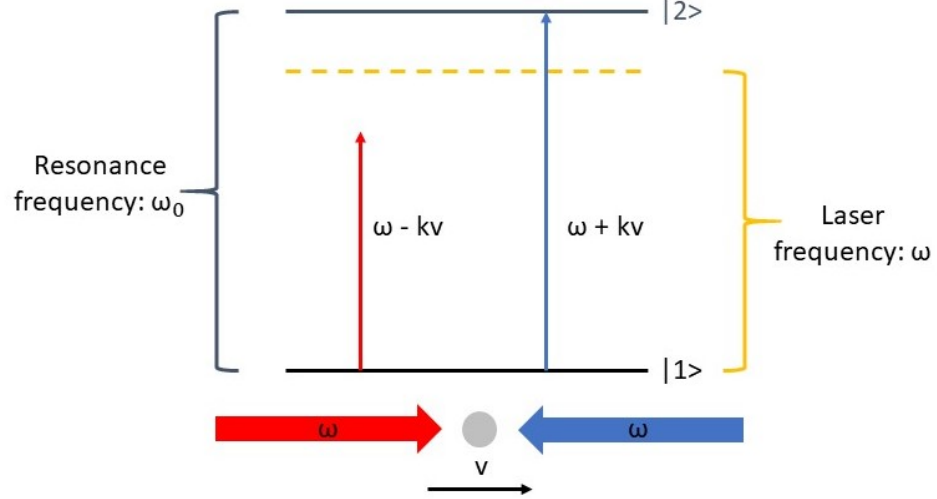


Figure 2.1: Doppler cooling of atoms in a 2-level system. A red-detuned laser is seen on resonance by the atom when traveling opposite to the direction of propagation of the laser, while a laser traveling on the same direction as the atom is seen further red-detuned, in the reference frame of the atom.

wavelength, and  $p$  the momentum of the atom. A second momentum kick is received when the atom re-emits the photon, but since this occurs in random directions, the effect averages to zero.

In practice, atoms in a gas move in all directions; to reduce their temperature, laser cooling must be performed in all three dimensions. Three orthogonal pairs of counter-propagating beams are needed, all slightly red detuned from resonance. The net effect is a viscous damping force at the intersection of all the beams, given by

$$\vec{F} = -\alpha \vec{v}, \quad (2.1)$$

where  $\alpha$  is the damping parameter [63]. This technique is called optical molasses.

Following Foot [64], we can derive the exact viscous force produced by molasses cooling for a 2-level atom. First, we must consider the force imparted by a laser beam

onto an atom, the scattering force:

$$F_{scatt} = \hbar k \frac{\Gamma}{2} \frac{I/I_{sat}}{1 + I/I_{sat} + 4\delta^2/\Gamma^2}, \quad (2.2)$$

where  $k=\omega/c$  is the laser's wavenumber,  $\Gamma$  is the spontaneous decay rate of the atoms,  $I$  is the laser intensity,  $I_{sat}$  is the saturation intensity, and  $\delta$  is the laser's frequency detuning from resonance in the atom's reference frame

$$\delta = \omega - \omega_0 + kv, \quad (2.3)$$

where  $\omega_0$  is the atomic resonance frequency, and the term  $kv$  is included to take into account the Doppler shift.

From equation 2.2, we can deduce the force on an atom due to a pair of counter-propagating beams, as in the case of optical molasses cooling

$$F_{molasses} = F_{scatt}(\omega - \omega_0 - kv) - F_{scatt}(\omega - \omega_0 + kv). \quad (2.4)$$

For  $kv \ll \Gamma$ , and  $I \ll I_{sat}$

$$F_{molasses} = 8\hbar k^2 \frac{I}{I_{sat}} \frac{2\delta/\Gamma}{[1 + (\delta/\Gamma)^2]^2} v. \quad (2.5)$$

Comparing to equation 2.1, the damping coefficient is

$$\alpha = -8\hbar k^2 \frac{I}{I_{sat}} \frac{2\delta/\Gamma}{[1 + (\delta/\Gamma)^2]^2}. \quad (2.6)$$

To damp the atoms,  $\alpha$  must be positive. Therefore, the detuning must be negative ( $\delta < 0$ ). This agrees with the previous statement that the laser frequency must be red-detuned.

### 2.1.1 Doppler Cooling Limit

Fluctuations in the direction of the recoil kicks due to spontaneous emission, and fluctuations in the number of photons absorbed over a given time period, cause a

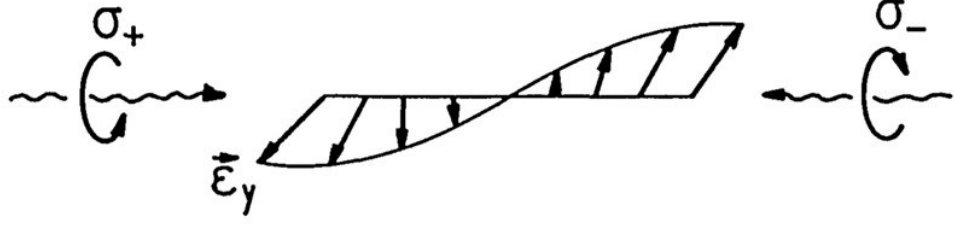


Figure 2.2: (Figure reproduced from ref. [67].) Polarization gradient cooling. A pair of counter-propagating beams with polarization  $\sigma^+$  and  $\sigma^-$  create a standing wave with a resulting linear polarization vector that rotates along the axis of propagation.

random walk in the velocity of the atoms. These fluctuations set the lowest temperature expected from molasses cooling. The Doppler cooling limit is reached when the detuning  $\delta = \omega - \omega_0 = -\Gamma/2$  [64, 65]

$$T_D = \frac{\hbar\Gamma}{2k_B}. \quad (2.7)$$

For the D2 line of  $^{87}\text{Rb}$ ,  $\Gamma = 38.11 \times 10^6 \text{ s}^{-1}$  [66], so  $T_D = 146 \text{ } \mu\text{K}$ .

### 2.1.2 Polarization Gradient Cooling

A standing wave formed by two counter-propagating laser beams with orthogonal polarization, result in a variation, along the standing wave axis, of the total electric field polarization vector (Figure 2.2). If the two laser beams are circularly polarized, the total polarization will be linear and will rotate over about the propagation axis [67] thorough an angle of  $2\pi$  over one optical wavelength [60]. In this configuration, commonly called  $\sigma^+ - \sigma^-$ , only  $\pi$  transitions ( $\Delta m_F = 0$ ) occur between magnetic sublevels. In the presence of a light field, an atom will experience a shift in its energy sublevels. These energy shifts depend on the polarization of the laser and on the orientation of the dipole moment of the atom.



Consider a sample of atoms with 2  $m_F$  levels on the ground state. As the atoms travel along the laser beam, they will experience a rotation on the quantization axis corresponding to the rotation of the laser polarization, this means the light shift will vary with position along the standing wave. For cooling to occur, the atoms must absorb photons with low frequency, and emit photons with higher frequency. If the laser is red-detuned, the ground state energy sublevel closest to resonance is the one shifted towards higher energy, and therefore the atoms in this sublevel are more likely to absorb a photon. The atoms will decay back to the ground state by re-emitting a photon via spontaneous emission. The atom will decay to the ground state to either the same  $m_F$  sublevel it started at, in which case, there is no net effect; or to the other  $m_F$  sublevel which is at a lower energy than its original  $m_F$  level, in this case, the emitted photon has a higher frequency than the absorbed photon.

When the loss in energy per cycle is the same as the recoil energy acquired in spontaneous emission, the limit of polarization gradient cooling is reached. This limit depends on the mass of the atom  $m$ , and the laser's wavelength  $\lambda$ :

$$T_r = \frac{h^2}{m\lambda^2 k_B}. \quad (2.8)$$

For  $^{87}\text{Rb}$ ,  $T_r = 392$  nK. Typical optical molasses setups can reach temperatures an order of magnitude above  $T_r$  [64].

## 2.2 Trapping of Atoms

To confine the atoms in a particular volume, inhomogeneous magnetic fields are used. The potential energy of a magnetic dipole  $\vec{\mu}$  in a field  $\vec{B}$  is given by

$$U = -\vec{\mu} \cdot \vec{B}. \quad (2.9)$$

The force field derived from a potential is given by

$$\vec{F} = -\nabla U. \quad (2.10)$$

Therefore, the magnetic force exerted on the magnetic dipole is

$$\vec{F} = \nabla(\vec{\mu} \cdot \vec{B}). \quad (2.11)$$

For an atom in the state  $|IJFm_F\rangle$ , equation 2.9 corresponds to a Zeeman energy [64]:

$$U = g_F \mu_B m_F B, \quad (2.12)$$

where  $g_F$  is the Landé factor, and  $\mu_B$  is the Bohr magneton. From equation 2.11 and 2.12, the force exerted on the atoms by the magnetic field in the z-direction is

$$F = -g_F \mu_B m_F \frac{dB}{dz}. \quad (2.13)$$

As can be seen in equation 2.12 and 2.13, the atoms with  $g_F m_F > 0$  will experience a lower potential energy as they move towards lower magnetic field region. These low-seeking state atoms will remain in the local magnetic field minima.

The magnetic field from a pair of coils in an Anti-Helmholtz configuration, as seen in figure 2.3 produces a quadrupole field that cancels at the center point of the two coils and increases toward the coils

$$B = A\sqrt{\rho^2 + 4z^2}, \quad (2.14)$$

where  $\rho^2 = x^2 + y^2$ , and A is the constant field gradient [60].

The low-field-seeking atoms will find their equilibrium position at the center of the coils and a restoring force will act on them as they move away from their equilibrium.

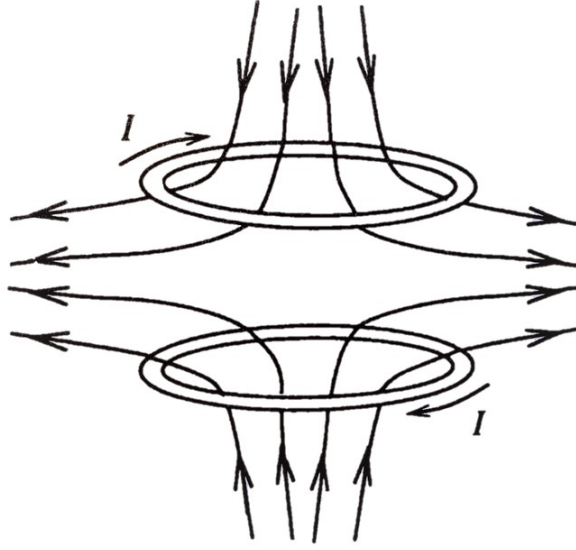


Figure 2.3: (Figure reproduced from ref. [60].) Diagram of an Anti-Helmholtz coil configuration, which produce a quadrupole trap.

### 2.3 Magneto-Optical Traps

Magneto-Optical traps, also called MOTs, are widely used to trap and cool atoms since they were first demonstrated in 1987 [68]. To understand the basic principle of atom trapping, consider an atom with spin  $J=0$  ( $m_J = 0$ ) ground state, and  $J=1$  ( $m_J = -1, 0, +1$ ) excited state. The atoms are subjected to a magnetic field which Zeeman splits the energy levels by

$$\Delta E = \mu m_J B. \quad (2.15)$$

If the magnetic field varies linearly ( $B(z) = bz$ ), like in the case of a quadrupole configuration, the excited state  $m_J = +1$  is shifted up for  $B > 0$ , while for  $B < 0$ ,  $m_J = -1$  is shifted up, as illustrated in figure 2.4. A pair of counter-propagating red-detuned laser beams is directed to the trap. A left-handed circularly polarized ( $\sigma^-$ ) beam is propagated in the  $-\hat{z}$  direction, and a right-handed circularly polarized

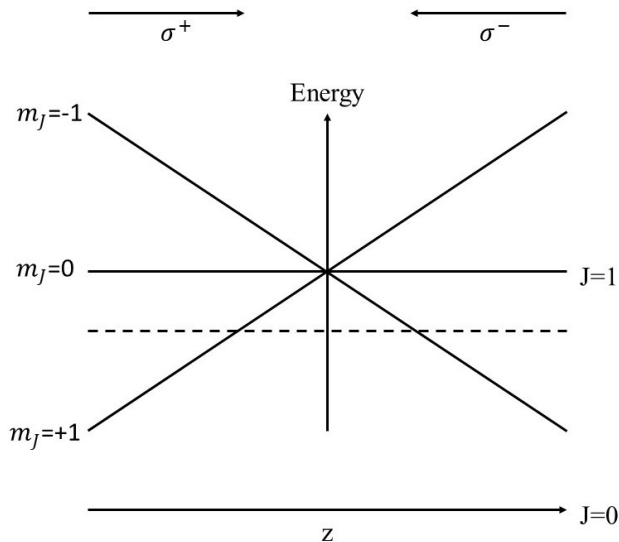


Figure 2.4: Zeeman energy splitting of an atom in a linearly inhomogeneous magnetic field. The dashed line represents the laser frequency seen by an atom at rest.

( $\sigma^+$ ) laser is propagated in the  $+\hat{z}$  direction. For atoms located at  $z < 0$  in figure 2.4; the level  $m_J = 1$  is closer to resonance and will therefore preferentially absorb the  $\sigma^+$  beam, which pushes the atoms to the center of the trap [60]. This technique enables a position dependent force on the atoms similar to how molasses cooling provides a velocity dependent force.

## 2.4 Atom Chips

In 1995, Weinstein and Libbrecht [69], published a description of a planar geometry for magnetically trapping neutral atoms near the surface of a chip containing embedded wires. The wires produce high magnetic field gradients and curvatures needed for trapping atoms. The surface in which the wires are embedded serve as a heat sink allowing higher currents to be run through the wires, enabling the production of

high magnetic fields [70]. Recently, atom chips have been developed as a way of integrating trapping and manipulation of cold matter in a single compact device [71], they are popular in the BEC community [72, 73, 74], and present great potential for use in quantum computing applications [75, 76]. Atom chips have enabled the study of phenomena like Johnson noise [74], Casimir-Polder potential [74, 77, 78], and degenerate Bose gases [79, 80, 81, 82].

The principle of operation of an atom chip is to provide highly localized magnetic field gradients for atom trapping and manipulating. Some atom chip architectures are self-sufficient, while others are used in combination with external magnetic fields. For trapping of neutral atoms, quadrupole traps are typically desired. A 2-dimensional quadrupole trap can be created by superimposing the magnetic field produced by a conducting wire with a constant magnetic field perpendicular to the wire axis [83]. As seen on figure 2.5, the circular magnetic field of the wire is canceled out by the bias field at a distance

$$r_0 = \left(\frac{\mu_0}{2\pi}\right) \frac{I_w}{B_b}, \quad (2.16)$$

where  $I_w$  is the wire's current, and  $B_b$  is the bias magnetic field [84]. This configuration, allows trapping low field seeking atoms along the wire at a very close distance to the surface. Similar traps can be created by designing the appropriate combinations of wires and external magnetic fields.

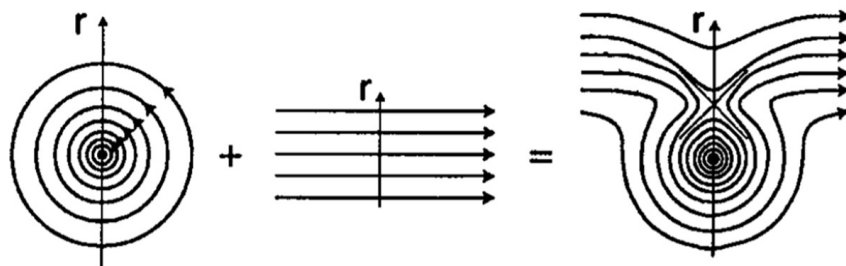


Figure 2.5: (Figure adapted from ref. [83].) Magnetic field produced by a wire, bias homogeneous magnetic field, and superposition of the two fields.

## CHAPTER 3

### MAGNETIC COUPLING OF ATOMIC ZEEMAN STATE TO CANTILEVER

Cantilevers present very high sensitivity and their effect is highly localized, which makes them a strong candidate to be used in quantum simulators involving ultra-cold atoms where single lattice site addressing is required [85]. This chapter covers the details of an experiment coupling a cantilever to a sample of Rubidium atoms.

#### 3.1 Rubidium

Alkali atoms have been widely studied for cooling and trapping as they have a simple hydrogen-like electronic structure. Rubidium is an alkali atom that presents two naturally occurring isotopes:  $^{85}\text{Rb}$  which is stable, and  $^{87}\text{Rb}$ , which is slightly radioactive with a half-life of 48.8 billion years decaying to  $^{87}\text{Sr}$  [86]. In our experiment, we use  $^{87}\text{Rb}$ . For optical Doppler cooling, a transition where the atoms decay back to the state they were excited from is needed. This is called a closed cycling transition or cooling transition. Rubidium is widely used for cooling, as its electronic structure contains a cooling transition.

##### 3.1.1 Energy Levels

The total electron angular momentum  $\vec{J}$ , which is a result of the coupling between the orbital angular momentum  $\vec{L}$  of an electron with its spin angular momentum  $\vec{S}$  is given by,

$$\vec{J} = \vec{L} + \vec{S}, \quad (3.1)$$

where

$$|L - S| \leq J \leq L + S. \quad (3.2)$$

As discussed by Steck [66], in the case of  $^{87}\text{Rb}$  at the ground state,  $L = 0$ ,  $S = 1/2$ . At the first excited state,  $L = 1$ ,  $S = 1/2$ . Therefore, from 3.2 we conclude that for the ground state,  $J=1/2$ ; and for the excited state,  $J = 1/2$  or  $J = 3/2$ . This fine structure transition is called the D line. In particular, the transition from  $L = 0$ ,  $J = 1/2$  to  $L = 1$ ,  $J = 1/2$  is called the D1 line, also labeled  $5^2S_{1/2} \longrightarrow 5^2P_{1/2}$ . The transition from  $L = 0$ ,  $J = 1/2$  to  $L = 1$ ,  $J = 3/2$  is called the D2 line, or  $5^2S_{1/2} \longrightarrow 5^2P_{3/2}$ . In the experiment described in this dissertation, we use the D2 transition line.

The total electron angular momentum couples with the total nuclear angular momentum  $\vec{I}$ , this results in the total atomic angular momentum  $\vec{F}$ , given by,

$$\vec{F} = \vec{J} + \vec{I}, \quad (3.3)$$

where

$$|J - I| \leq F \leq J + I \quad (3.4)$$

and  $m_F\hbar$  is the eigenvalue of  $F_z$ .

For  $^{87}\text{Rb}$ ,  $I = 3/2$ . Therefore from 3.4, in the ground state:  $F = 1$ , or  $F = 2$ . For the excited state of the D2 line:  $F = 0$ ,  $1$ , or  $2$ . An energy diagram of the hyperfine structure of  $^{87}\text{Rb}$  D2 line is presented on figure 3.1.

Optical dipole transitions between energy states are allowed, provided they follow the transition rules [64]:

$$\Delta F = 0, \pm 1 \quad (3.5)$$



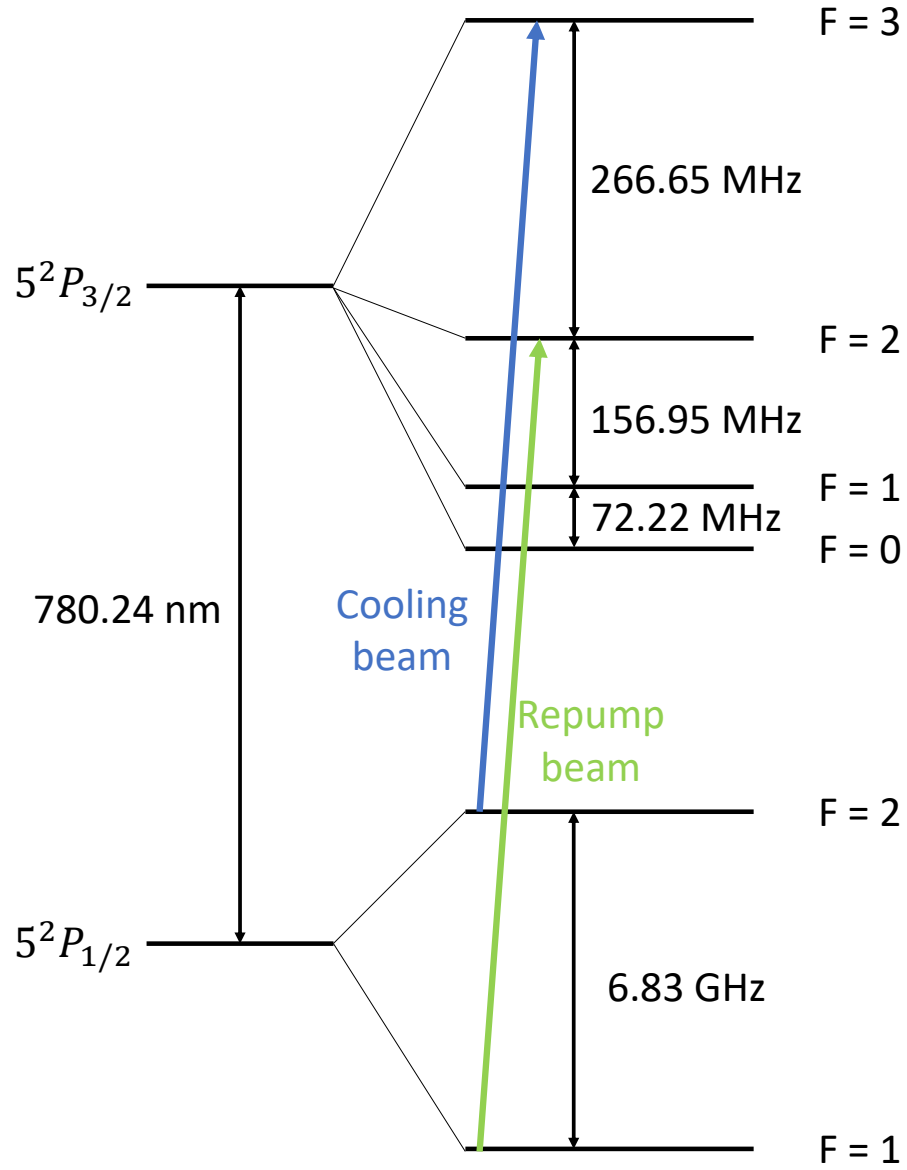


Figure 3.1: (Adapted from ref. [66].) Hyperfine structure of  $^{87}\text{Rb}$  D2 transition. The cooling and imaging beams are tuned to the  $F = 2 \rightarrow F' = 3$  transition. The repump beams are tuned to the  $F = 1 \rightarrow F' = 2$  transition.

$$\Delta M_F = 0, \pm 1 \quad (3.6)$$

if  $\Delta F = 0$ , and  $M_F = 0$ , then:

$$\Delta M_F \neq 0. \quad (3.7)$$

The cooling laser's frequency is tuned to match the  $F = 2 \rightarrow F' = 3$  cooling transition. According to the transition rule 3.5, atoms in the  $F' = 3$  excited state will decay back to the  $F = 2$  state, but off-resonance excitation into the  $F' = 2$  state is possible. In this case, the atoms can either decay to  $F = 2$ , or to  $F = 1$ . A repump beam is used to pump the atoms on the  $F = 1$  state back to the  $F = 2 \rightarrow F' = 3$  transition. This repump laser is tuned to the  $F = 1 \rightarrow F' = 2$  transition. That way, according to 3.5, the atoms will decay to  $F = 2$  which is what we want, or to  $F = 1$ , in which case they will again be pumped to  $F' = 2$ . The D2 transition line of  $^{87}\text{Rb}$  has a natural linewidth of  $2\pi \times 6.065$  MHz

## 3.2 Laser System

Two lasers are used in our experiment: a master laser and a repump laser. The master laser is used to produce the MOT beams, imaging beams, and optical pumping beams. The repump laser is used to optically pump the atoms to the desired hyperfine energy level. The master laser is a 780 nm Littrow configuration, extended cavity diode laser (MOGLabs: ECD-003) with an output power of 60 mW and a linewidth of about 200 kHz. This laser is seeded into a fiber-coupled tapered amplifier (Newport: TA-7613-H) which amplifies the input power to about 700 mW. The repump is a 780 nm distributed Bragg reflector (DBR) laser (Vescent photonics: D2-100) with an output

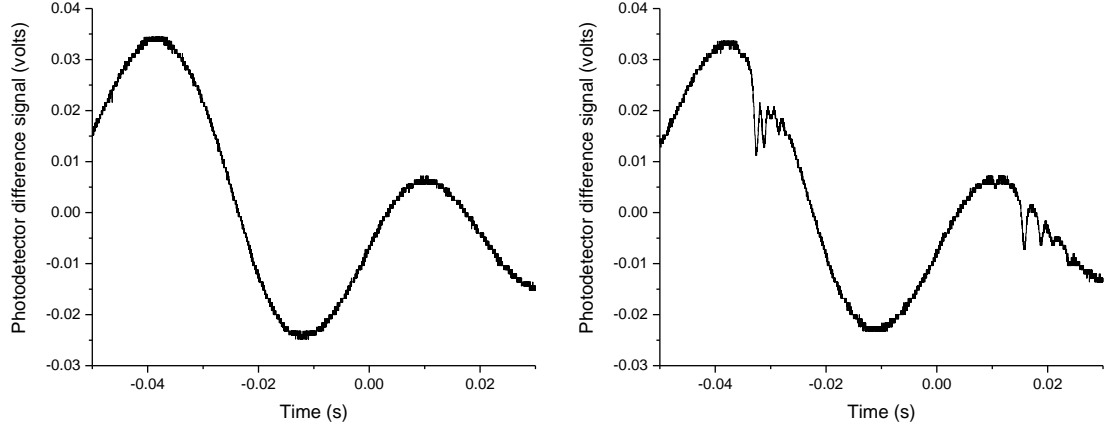


Figure 3.2: Photodetector signal from a  $^{87}\text{Rb}$  vapor cell. The laser's frequency is scanned as a function of time. (Left) Signal from probe beam crossing vapor cell with no pump beam. (Right) Doppler-free spectra from probe beam when counter-propagating pump beam is used.

power of 100 mW, and a linewidth of 1 MHz. Each of the lasers are locked to a specific frequency. Once locked, the frequency of each laser can be shifted by using an Acousto-Optical Modulator.

### 3.2.1 Saturated Absorption Spectroscopy

To address the specific energy transitions we desire, the lasers must be tuned to the specific frequencies we care about and remain locked at the chosen frequency. To solve this issue, spectroscopy on a sample of Rubidium atoms in a vapor cell is done. The basic idea is to lock the laser's frequency to an absorption peak. The issue with this method is the atoms present a distribution of velocities in the vapor cell; because of the Doppler effect, a broad range of laser frequencies will produce absorption in the cell.

Saturated absorption spectroscopy is a Doppler-free approach used to resolve hy-

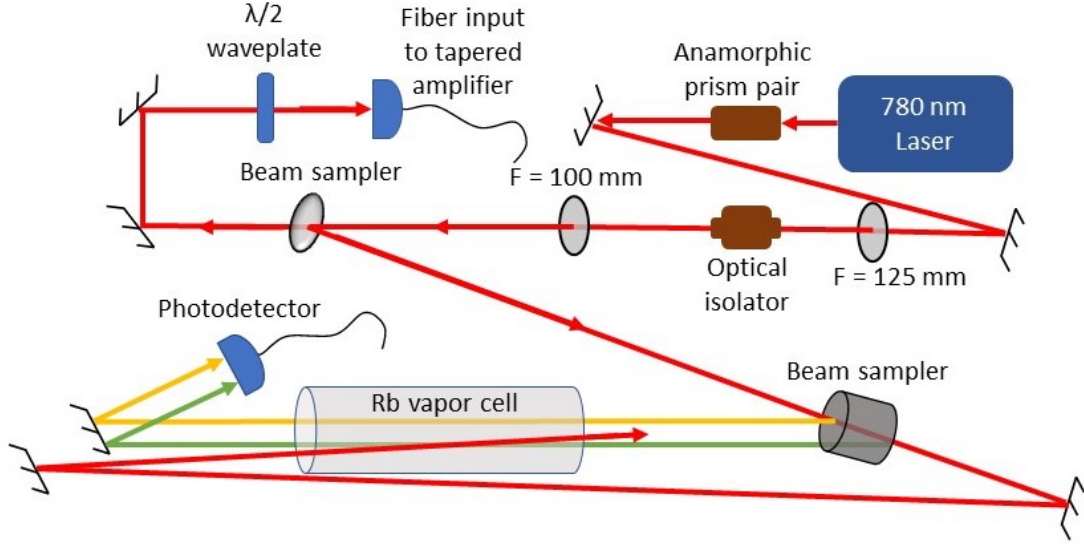


Figure 3.3: Saturated spectroscopy optical layout. The cooling laser is split after an optical isolator. The majority of the laser power is sent to a fiber input that seeds the tapered amplifier. A sample of the laser is further split into 3 beams: the pump beam (red), which is the one with highest power, a probe beam (green), and a reference beam (orange). All 3 beams are ran through a Rubidium vapor cell. The pump beam and the probe beam are overlapped, while the reference beam freely crosses the vapor cell.

perfine absorption peaks. In this method, two counter-propagating laser beams of the same frequency are sent through a sample of atoms. The power of one of the beams, the pump beam, is higher than that of the second one, the probe beam. Due to the Doppler effect, the pump beam excites atoms that have a velocity [64]

$$v = \frac{\omega - \omega_0}{k}, \quad (3.8)$$

where  $\omega$  is the frequency of the pump and probe beams,  $\omega_0$  is the resonance frequency of the atoms, and  $k$  is the wavenumber. When close to resonance, both the pump and probe will interact with the same atoms: those with a velocity near 0 (or with its velocity direction perpendicular to the laser beam). The high power pump beam will then excite the atoms to the point of saturation. The low power probe beam

will induce stimulated emission. When on resonance, the probe beam will show a dip in its absorption peak at the atomic transitions, as can be seen on figure 3.2. The optical layout of the saturated spectroscopy in our setup is shown in figure 3.3.

### Cross-over Resonances

In a saturated absorption spectra, peaks that correspond to each allowed energy transition are present, but peaks also appear midway between the allowed energy transitions. These cross-over resonance peaks occur because absorption from one transition reduces the absorption for the other transition [64]. These cross-over peaks only occur when the separation between energy levels is less than the Doppler width.

By resolving the hyperfine transitions of  $^{87}\text{Rb}$ , both lasers can be locked to the desired frequencies. In our system, the cooling laser is locked to the  $F'=1-3$  cross-over peak, which is located half way between the  $F'=1$  and the  $F'=3$  transitions, therefore the laser's frequency must be shifted by 211.80 MHz to be tuned to the  $F=2 \longrightarrow F'=3$  transition. The repump laser is locked to the  $F'=1-2$  cross-over peak, so it must be shifted by half the energy difference between the  $F'=1$  and the  $F'=2$  transitions (78.48 MHz) to be tuned to the  $F=1 \longrightarrow F'=2$  transition.

### Acousto-Optical Modulators

For both of the lasers, an Acousto-Optical Modulator (AOM) (Gooch & Housego 46080-1-LTD) is used to shift the laser frequencies. An AOM consists of a crystal through which acoustic waves are propagated. Photons crossing through the crystal can exchange momentum with the crystal's phonons, therefore the incoming light's frequency can be modulated by varying the frequency of the acoustic waves traveling

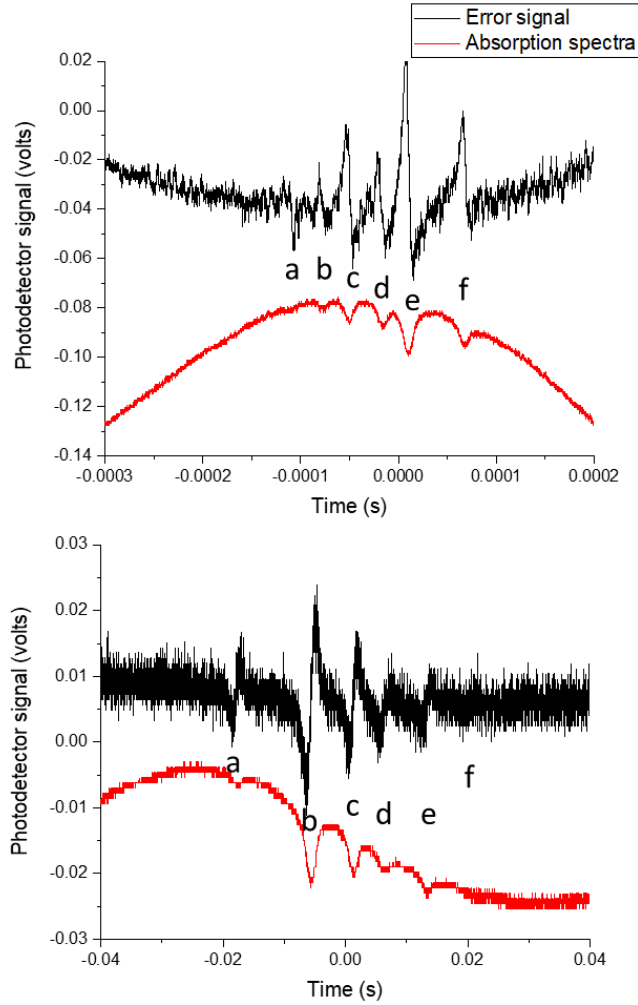


Figure 3.4: (Top)  $F = 1$  transition spectra of  $^{87}\text{Rb}$  D2 line. Absorption peaks: a)  $F' = 0$ . b)  $F' = 0-1$  cross-over. c)  $F' = 1$ . d)  $F' = 0-2$ . e)  $F' = 1-2$  cross-over. f)  $F' = 2$ . (Bottom)  $F = 2$  transition spectra of  $^{87}\text{Rb}$  D2 line. Absorption peaks: a)  $F' = 3$ . b)  $F' = 2-3$  cross-over. c)  $F' = 1-3$ . d)  $F' = 2$ . e)  $F' = 1-2$  cross-over. f)  $F' = 1$ . In both graphs, the black trace represents the error signal which is used to lock the laser. The red curve is the Doppler-free absorption spectra taken from the photodetector.

through the crystal.

The cooling laser's frequency is shifted by passing twice through an AOM, where on each pass, the frequency gets shifted by 105.9 MHz. This method not only enables the large detuning to be achieved, but by passing through the AOM twice, any beam deflection occurring when the laser's frequency is changed is canceled out.

### 3.2.2 Optical Layout

The optical table (TMC: 784-759-02R) used in our experiment is designed to damp external vibrations. It is also floating on Nitrogen for maximum vibration isolation. Describing the totality of the optical elements on the table would be an overwhelming task. For convenience, the layout of the optical elements can be divided into several sections, although the sections might be intertwined with each other, a more didactic approach might be to study each section individually.

#### Master Laser

The master laser shown on figure 3.3 is first run through an anamorphic prism pair to transform the elliptical profile of the laser into a circular profile. An optical isolator prevents back-reflections from reaching the laser, which could cause a number of instabilities in the laser. The optical isolator is located in the center of a beam-resizing telescope consisting of a lens with a focal length of 125 mm and a second lens with a focal length of 100 mm, resulting in a magnification of 0.8x. The beam is then split into two by a beam sampler. One of the beams is coupled into the input fiber of the tapered amplifier, previously going through a  $\lambda/2$  waveplate to align the laser

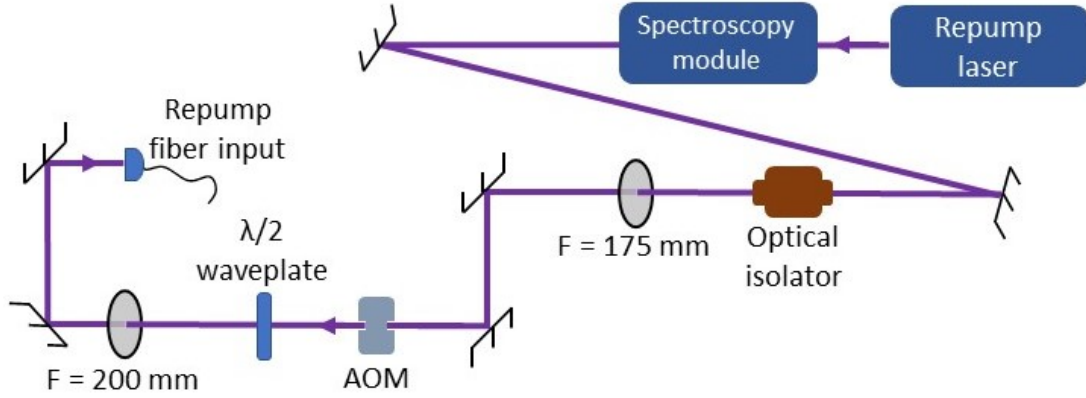


Figure 3.5: Repump laser optical layout. The repump laser is run through an AOM to allow tuning of the laser's frequency before it is coupled into an optical fiber.

polarization with the fiber's polarization axis. The second beam is used to create a saturated absorption spectroscopy signal (see section 3.2.1).

### Repump Laser

To lock the repump laser, we use a commercial saturated absorption spectroscopy module (Vescent: D2-110 Rubidium). The compact architecture of this spectroscopy module allows to reduce the footprint of the spectroscopy setup from  $640 \text{ cm}^2$  to  $100 \text{ cm}^2$ . After the spectroscopy module, an optical isolator is used to prevent feedback in the laser. The beam is then resized for optimal coupling into a polarization maintaining optical fiber with two lenses of focal lengths 175 mm and 200 mm (see figure 3.5); this results in a magnification of 1.14x. In the middle of the telescope, when the beam is small, an acousto-optical modulator is placed to allow tuning of the laser's frequency (see section 3.2.1). Also, before the optical fiber input, a  $\lambda/2$  waveplate is used to align the polarization of the laser with the fiber's polarization axis.



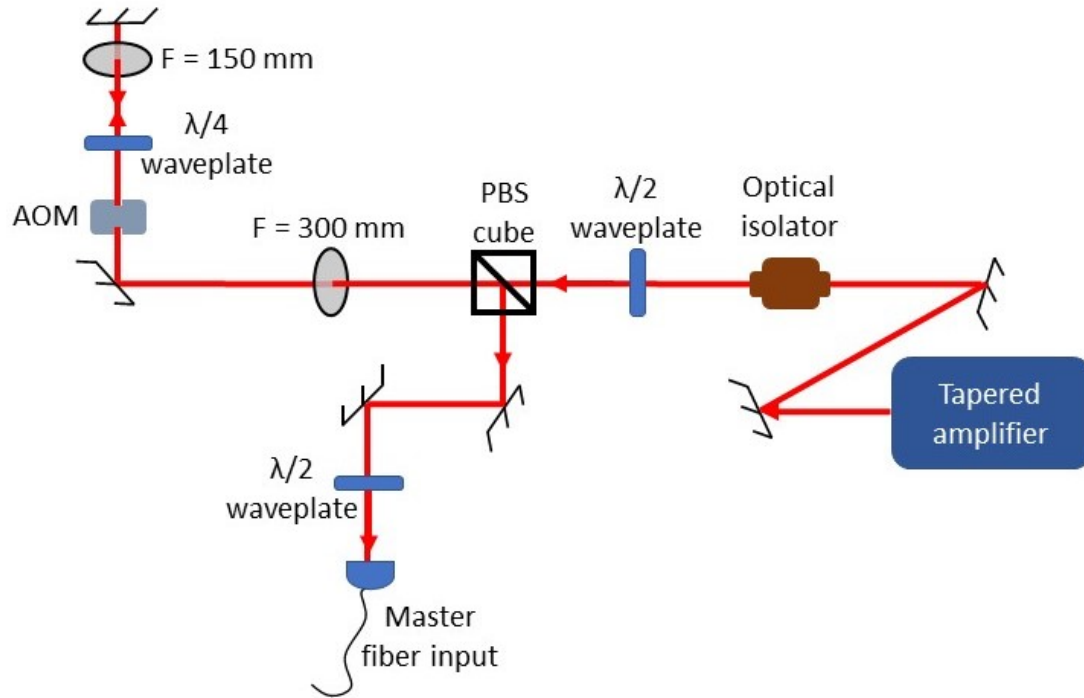


Figure 3.6: Acousto-optic modulator double-pass layout. An AOM is used to allow tuning of the master laser's frequency. By going through the AOM twice, a broader tuning range is achieved, as well as also canceling out beam deflections.

### Double-Pass AOM

As can be seen in figure 3.6 the tapered amplifier, which is set to output about 700 mW of power, is followed by an optical isolator that prevents back-reflections from returning into the amplifier. A  $\lambda/2$  waveplate is used to control the polarization axis of the laser. The AOM is located in the middle of a telescope consisting of two lenses with focal lengths 300 mm and 150 mm. The double-pass AOM provides a large tunability range and cancels out beam deflections caused when changing the frequency of the laser (see section 3.2.1). A  $\lambda/4$  waveplate alters the polarization of the beam from linear to circular. After the beam is reflected back by a mirror, the polarization is converted back to linear such that at the polarizing-beam-splitter cube,



have a Gaussian profile out of the fiber. As can be seen on figure 3.7, the repump beam is resized by a telescope with two lenses of focal lengths 25 mm and 200 mm, for a magnification of 8x, resulting in a beam diameter of about 2.3 cm, and 6 mW of power. A  $\lambda/2$  waveplate is placed before a beam splitter cube to control the polarization axis of the repump laser. Out of the fiber, the master laser is split into two by a beam splitter cube. One of the beams is used for imaging and for optical pumping, while the other beam is the cooling beam. The cooling beam is resized using a lens of focal length 35 mm and a second lens with focal length 200 mm for a 5.7x magnification, resulting in a beam diameter of about 2 cm. In the middle of this telescope, a mechanical shutter (Uniblitz electronics: LS3ZM2) is placed to provide on/off control of the cooling beam, the shutters used in our experiment take about 2 ms to fully open or close. After the repump and the cooling beams are resized, they are combined by a beam splitter cube and will remain overlapped.

### Imaging and Optical Pumping Beams

The imaging and optical pumping beams shown in figure 3.8 (which come from figure 3.7), are split into two using a beam-splitter cube. Both of these beams are independently expanded by 5x. The optical pumping beam is resized using lenses with focal lengths 35 mm and 175 mm, while the imaging beam is resized with lenses of focal length 300 mm and 60 mm, resulting in a beam diameter of 1.1 cm. A mechanical shutter (Uniblitz electronics: Optical pumping shutter: LS6T2. Imaging shutter: LS3T2) is placed between the lenses, near the focus, to provide the ability of independently switching on or off, the imaging beam and/or the optical pumping beam. The imaging beam is split into two: the front imaging beam, and the side imaging beam, which gets combined with the optical pumping beam by a beam splitter cube.

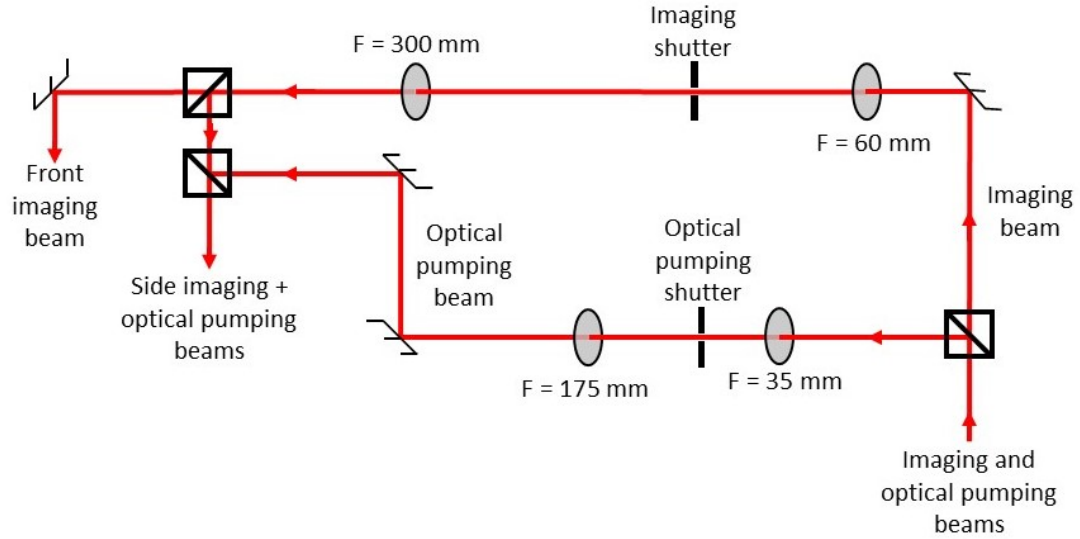


Figure 3.8: The imaging and optical pumping beams are each resized and ran through a mechanical shutter to allow individual on/off control of these beams.

### Chamber Vicinity Layout

As shown in figure 3.9, the combined repump and cooling beams from figure 3.7 are split into two by a beam-splitter cube. Each of the two beams are then split again into two by using a second beam-splitter cube. The resulting 4 beams are the east, west, north and up beams. The up beam will be reflected on the mirror mounted on the top of the atom chip layer to create a "south" beam, while the north beam will create a "down" beam by reflecting on the mirror. This way, close to the mirror surface, 3 pairs of counter-propagating beams are crossing each other. Each of the 4 beams are ran through a  $\lambda/4$  waveplate to modify the laser's polarization from linear to circular before entering the vacuum chamber.

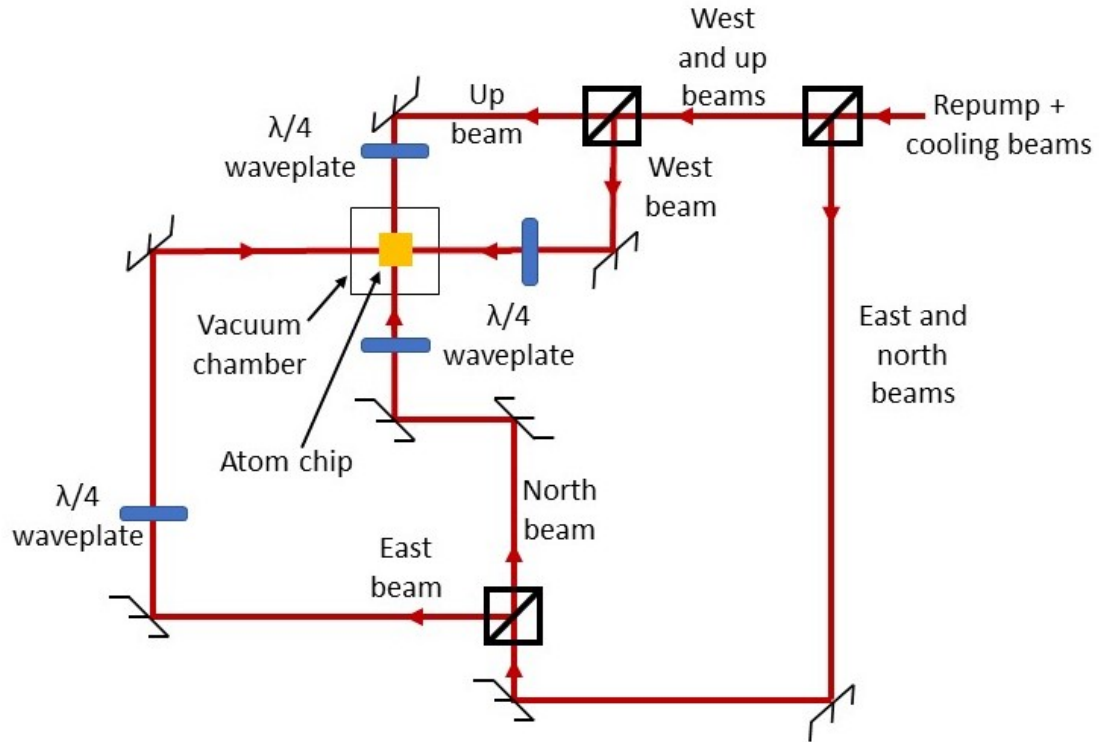


Figure 3.9: The repump and cooling beams are split into 4 and are directed to the chamber.

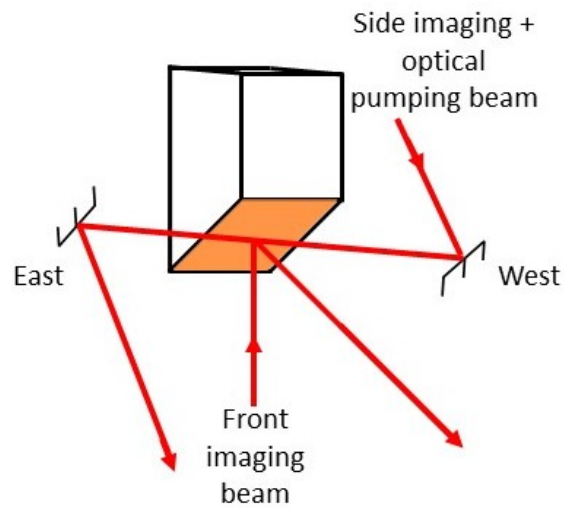


Figure 3.10: The side imaging and optical pumping beam are directed from west to east parallel to the mirror surface. The front imaging beam is directed upwards and reflected onto the mirror surface, exiting on the north side of the chamber.

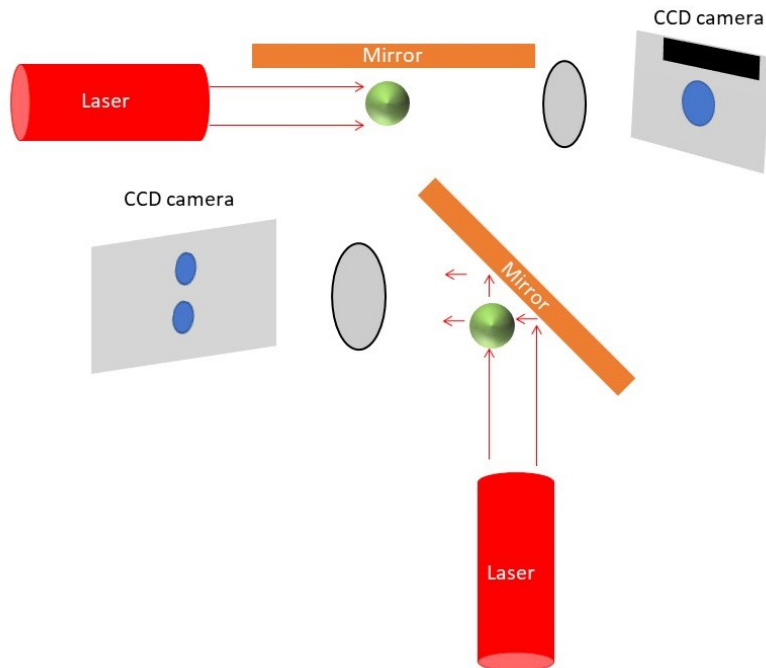


Figure 3.11: Method for imaging atoms. (Top) Side imaging. (Bottom) Front imaging.

### Imaging Beams on Chamber

To image the atoms, we use two beams. As shown on figure 3.10, the side imaging and optical pumping beam are directed from west to east parallel to the mirror surface. The front imaging beam is directed upwards and reflected onto the mirror surface, exiting on the north side of the chamber.

## 3.3 Imaging

To detect the atoms in our system, we use two 12 bit CCD cameras (pco.pixelfly qe) each with a pixel size of  $6.45 \mu\text{m}$ . The cameras are connected to a computer from which they can be triggered using Labview. One camera is pointed at the side of

the copper block that holds the atom chip. With the side camera we can study the atom cloud's width on the vertical axis and on the north-south axis. Also, we can study the cloud's optical density on the east-west axis. The second camera is pointed directly towards the atom chip. As can be seen on figure 3.11, because the atoms are very close to the mirror surface, the front camera produces a double image of the atoms. One of the images is produced when the laser strikes the atoms and then gets reflected on the mirror. This image can be used to study the optical density on the vertical axis. The second image is created when the laser first hits the mirror, then the atoms. This image can be used to study the optical density on the north-south axis. In addition, the two images from the front camera can be used to study the cloud's width on all three axis.

To image the atoms, a single lens system is used. The lens and the camera are placed such that the following condition is met:

$$\frac{1}{f} = \frac{1}{o} + \frac{1}{i}, \quad (3.9)$$

where  $f$  is the focal length of the lens,  $o$  is the distance from the atoms to the lens, and  $i$  is the distance from the lens to the camera.

### 3.3.1 Fluorescence Imaging

The MOT can be easily imaged by collecting the light emitted by the atoms as they absorb and re-emit photons from the MOT-forming laser beams. The advantage of this method of imaging is that it can be used to watch the MOT "live". A disadvantage is that the signal is weak because the atoms scatter light in all directions, but only a small solid angle reaches the camera.

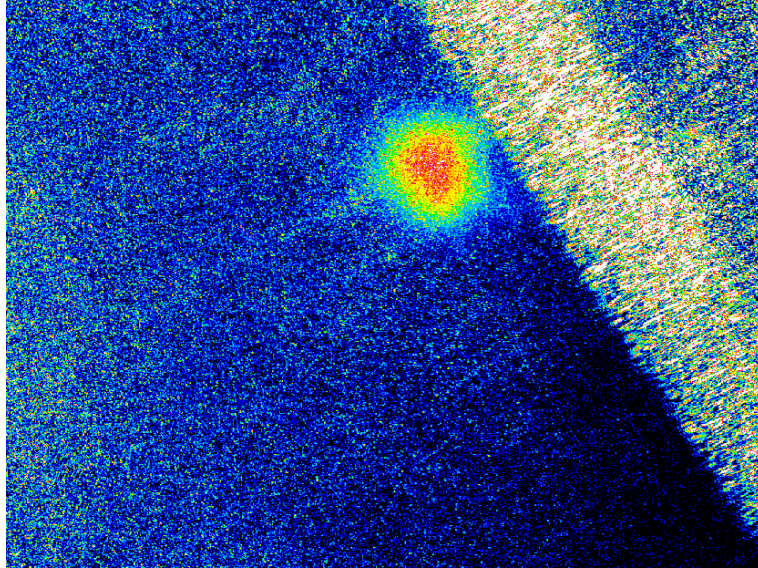


Figure 3.12: Fluorescence image of MOT containing  $10^8$  atoms. The red area in the center of the cloud represents the most optically dense region, while the yellow and green areas represent less dense regions.

### 3.3.2 Absorption Imaging

When shining a near-resonance laser onto the atoms, a portion of the photons, which depends on the cloud's optical density, will be absorbed by the atoms. By collecting the laser's light on a CCD camera, the shadow cast by the atoms is imaged. To reduce background noise from the images, a picture with no atoms present is taken. Dividing the image with atoms by the image with no atoms eliminates the background, and results in an image of the transmitted light only. A transmission of 1 means all the light from the laser was collected on the camera, and a transmission of 0 means all of the laser light was blocked during the image taken with atoms. Two methods have been used to take the image with no atoms. The first method is to turn the lasers and magnetic fields off so that the atoms fall and get dispersed. After waiting a period of time, the image is recorded with the atoms gone. If mechanical vibrations on the



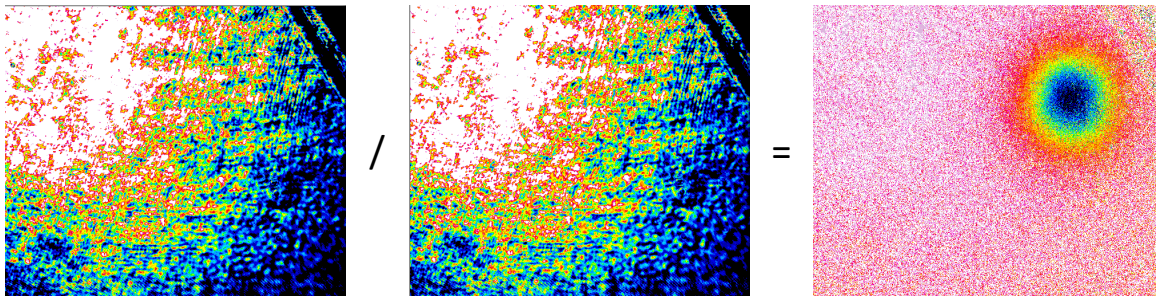


Figure 3.13: Absorption image of molasses cooled atoms. Two images are taken with a CCD camera. One with atoms present, and a background image with no atoms. The two images are divided to calculate the transmission. The dark blue region in the picture on the right is the area with most atoms. The atom cloud in this picture has a radius of about 1 mm.

table occur faster than the time period between the first and second image is recorded, motional shifts between the two images might occur. To minimize this effect, the wait time between the two images must be reduced. To reduce this time, the atoms must be quickly moved out of the interest region, or they can be pumped to a state that is dark to the imaging beam. This second method is achieved in our setup, by pulsing a hyperfine depump beam that optically pumps the atoms into the  $F = 1$  state. Using this depump method, the period between the two images is reduced from 80 ms to 0.1 ms.

### 3.4 Magnetic Coils

To produce the magnetic fields required to trap Rubidium 87 atoms, 3 pairs of coils are used. Attached to these coils there is a hollow copper block through which we run water circulated by a commercial chiller (Optitemp: OTI-10WL-03-116-SC1-M1L). This prevents the coils from overheating as high currents are ran through the coils.

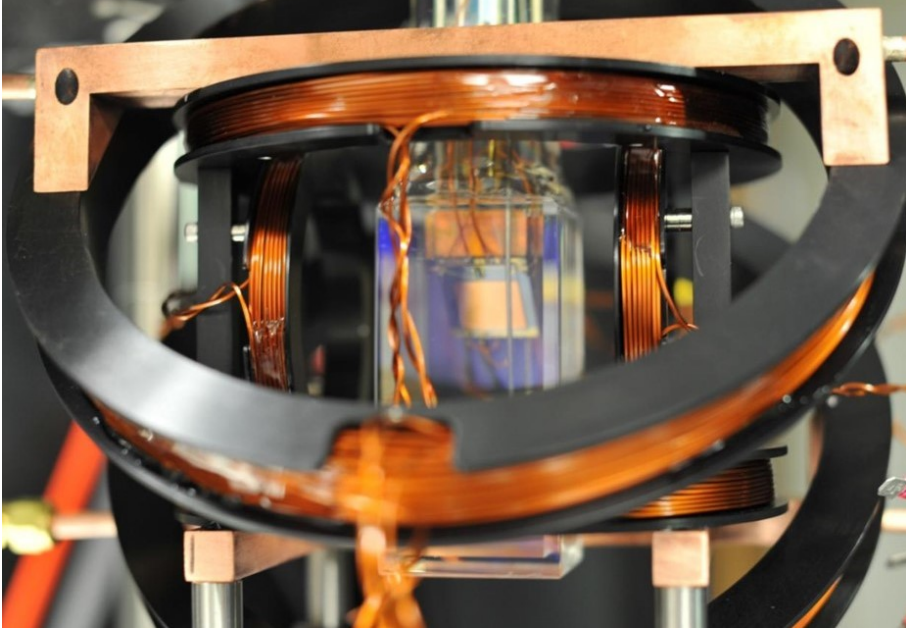


Figure 3.14: Anti-Helmholtz coils used in our experiment. Each coil is bolted to a water-cooled copper block to prevent overheating of the coils.

We have labeled each pair of coils according to their orientation with respect to the lab frame. On figure 3.14, the east-west coils are the smaller, inner coils; the vertical coils are the medium-sized ones, and the diagonal coils are the biggest ones. The diagonal coils, although not strictly orthogonal to the other two pairs of coils, do have an orthogonal component. The diagonal orientation is chosen to match the orientation of the atom chip in the chamber, which will need external fields in that direction later in the experiment. The construction details of each coil are described in table 3.1.

	East-west	Vertical	Diagonal
Diameter (cm)	10	15	20
Coil separation (cm)	9.5	9.5	10

Table 3.1: Coil construction details

Each pair of coils is wound with 16 AWG square wires around an anodized alu-

minum holder. Two pairs of coils contain two layers of wires. One set of wires is connected in a Helmholtz configuration to create a constant bias magnetic field, while the second set is connected in an anti-Helmholtz configuration. The bias fields can be used to cancel external magnetic fields, for example from the ion pump. Also, the bias fields are used to fine tune the position of the cloud of atoms when they are magnetically trapped by the atom chip. The details of the bias coils are on listed on table 3.2. Table 3.3 shows the details of the second set of wires, which create a gradient magnetic field by connecting the coils in an Anti-Helmholtz configuration.

	East-West	Vertical	Diagonal
Turns	30	19	29
Bias magnetic field	2.67 G/A	1.83 G/A	2.61 G/A

Table 3.2: Magnetic bias coils

	Vertical	Diagonal
Turns	57	91
Magnetic gradient	1.02 G/(A cm)	0.98 G/(A cm)

Table 3.3: Anti-Helmholtz coils

### 3.5 Atom Chip

As previously discussed in section 2.4, atom chips can be used to magnetically trap and manipulate atoms at very close proximity to a surface. This can be done with or without external magnetic fields, depending on the atom chip architecture. One of the advantages of atom chips is that they can be stacked, this way several configurations can be used. In our experiment, we have used a 3-layer atom chip fabricated at NIST. The 3 layers are stacked behind a copper mirror, which is used to produce a mirror-MOT. The mirror was fabricated by depositing copper onto pyrex. Copper

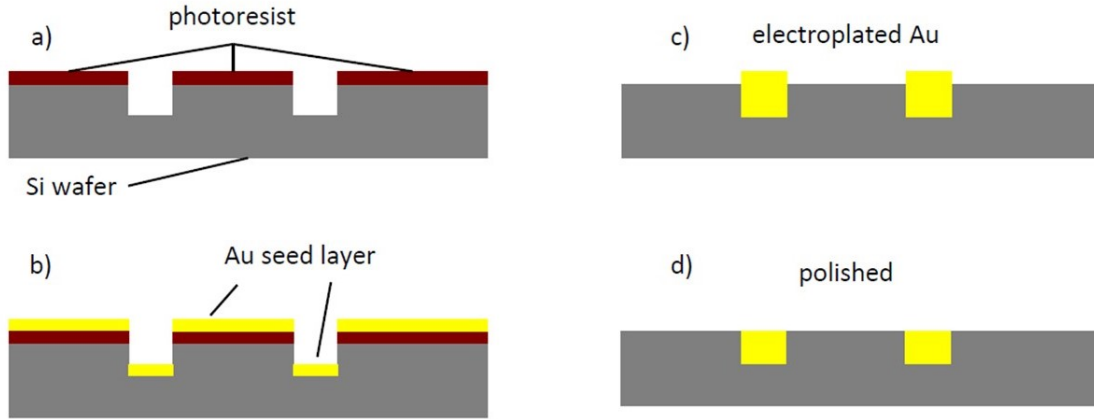


Figure 3.15: (Figure reproduced from ref. [87].) Atom chip's wire fabrication. a) Trenches are etched on a silicon wafer, the wafer is coated with photoresist except for the bottom of the trenches. b) A seed layer of gold is evaporated onto the wafer. c) After removing the photoresist + gold from the top of the wafer, gold is electroplated to fill the trenches and create the square wires. d) Excess gold is removed by polishing the surface.

was chosen over gold as it is less reactive with Rubidium.

The embedded wires in the atom chips were fabricated by etching 15-25  $\mu\text{m}$  deep trenches on a silicon wafer. A seed layer of titanium is evaporated onto the wafer to improve the adhesion of the following evaporated gold layer. By performing a photoresist liftoff, the evaporated gold is removed from the wafer except for the bottom of the trenches. Gold is electroplated on top of the gold seed layer to fill the trenches and form the wires. At the JILA workshop, the surface was then polished flat to remove any excess gold. Because the wires are surrounded by silicon on 3 out of their 4 sides, heat removal into the silicon surface is maximized, allowing higher currents through the wires. Additionally, the atom chip stack is mounted on a water-cooled copper block to ensure heat removal from the atom chip surface.

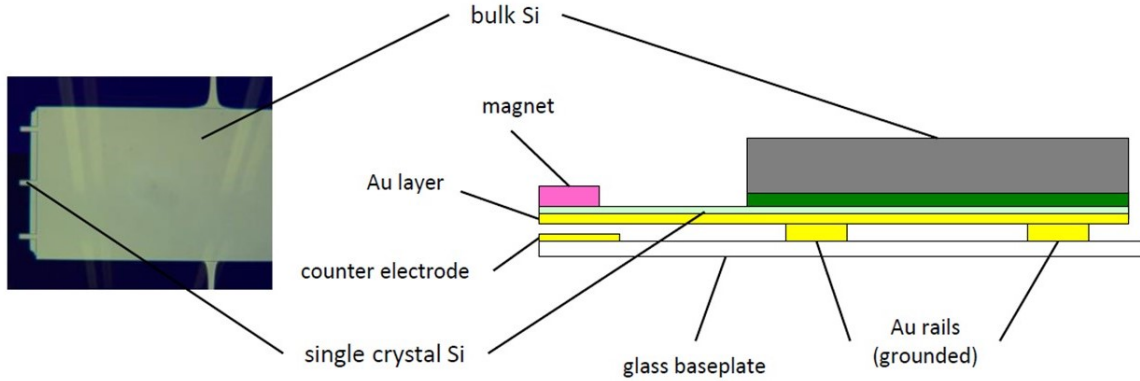


Figure 3.16: (Figure reproduced from ref. [87].) Cantilever layer assembly. The cantilevers are made of Silicon with a gold coating on the bottom. A magnet is epoxied to the tip of the cantilever beam.

### 3.5.1 Cantilever Layer

The first layer contains 3 cantilevers. Each cantilever is  $130\text{ }\mu\text{m}$  long,  $60\text{ }\mu\text{m}$  wide, and  $25\text{ }\mu\text{m}$  thick. On this experiment, we only use one of the cantilevers. The other two cantilevers were built in anticipation of future experiments. Gold is evaporated onto the bottom of each cantilever to make them electrically conductive. The cantilever assembly sits on  $9\text{ }\mu\text{m}$  thick gold rails which elevate the cantilever to provide a gap between the bottom of the cantilever and its counter electrode. The counter electrode is  $700\text{ nm}$  thick and made of gold. Finally, an electroplated CoNiMnP magnet [88] is epoxied to the tip of the cantilever. The magnet is  $60\text{ }\mu\text{m}$  wide,  $85\text{ }\mu\text{m}$  long, and  $9\text{ }\mu\text{m}$  thick with a total magnetic moment of approximately  $2 \times 10^{-9}\text{ J/T}$  directed outward from the cantilever.

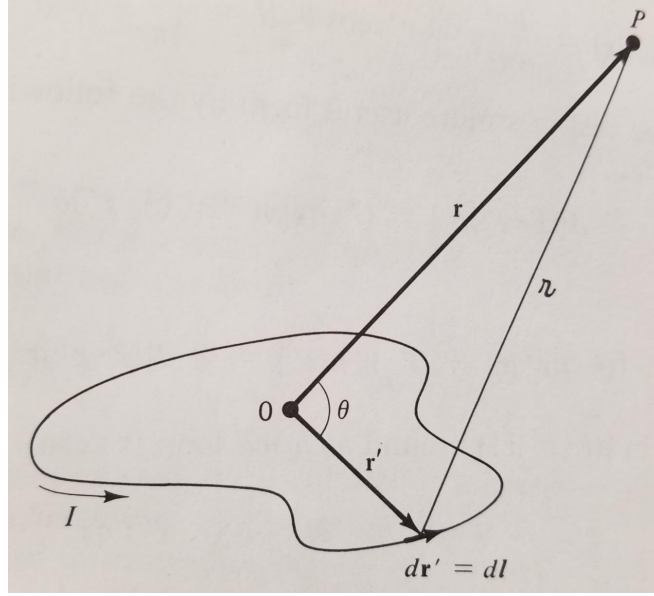


Figure 3.17: (Figure reproduced from ref. [89].) Diagram for calculating magnetic field from a current loop at a distant point.

### Magnetic Field from Cantilever

The magnetic vector potential in magnetostatics obeys the following equation

$$\vec{B} = \nabla \times \vec{A}, \quad (3.10)$$

where  $\vec{B}$  is the magnetic field. Using the above equation, Amperes law can be expressed as

$$\nabla^2 \vec{A} = -\mu_0 \vec{J}, \quad (3.11)$$

where  $\vec{J}$  is the current density and  $\mu_0$  is the vacuum permeability. For line currents  $\vec{I}$ , this equation can be expressed as

$$\vec{A} = \frac{\mu_0}{4\pi} \int \frac{\vec{I}}{r} dl. \quad (3.12)$$

A multipole expansion of the  $1/r$  term can be performed to approximate the

solution at distant points

$$\frac{1}{z} = \frac{1}{r} \left( \frac{r'}{r} \right)^n P_n(\cos\theta), \quad (3.13)$$

where  $P_n(\cos\theta)$  are the Legendre polynomials,  $z$ ,  $r$ , and  $r'$  are defined in figure 3.17.

Using the multipole expansion on equation 3.12, and taking only the second term yields the approximation for a dipole field

$$\vec{A} = \frac{\mu_0 I}{4\pi r^2} \int r' \cos\theta d\vec{l} = \frac{\mu_0 I}{4\pi r^2} \int (\hat{r} \cdot \vec{r}') d\vec{l}. \quad (3.14)$$

Following the algebraic steps from ref. [89], the magnetic vector potential for a dipole can be expressed as

$$\vec{A} = \frac{\mu_0 I}{4\pi r^2} \left[ -\frac{1}{2} \hat{r} \times \int r' \times d\vec{l} \right] = \frac{\mu_0 I}{4\pi r^2} \frac{\vec{m} \times \hat{r}}{r^2}, \quad (3.15)$$

where  $\vec{m}$  is the magnetic dipole moment. If the magnetic moment  $m$  is at the origin, and points in the  $z$ -direction, equation 3.15 can be expressed as

$$\vec{A} = \frac{\mu_0 I}{4\pi r^2} m \sin\theta \hat{\phi}, \quad (3.16)$$

where  $\phi$  and  $\theta$  are the radial and azimuthal angles respectively. The magnetic field is then given by

$$\vec{B} = \vec{\nabla} \times \vec{A} = \frac{\mu_0 m}{4\pi r^3} (2\cos\theta \hat{r} + \sin\theta \hat{\theta}). \quad (3.17)$$

In our experiment, the atoms will be at  $\theta = 0$ , so the magnetic field when the atoms are at distances far compared to  $\vec{m}$  is

$$\vec{B} = \frac{\mu_0 m}{2\pi r^3} \hat{r}. \quad (3.18)$$

The amplitude of oscillation of the magnetic field gradient due to the magnet displacement is given by

$$B_m = \frac{3m\mu_0\delta z}{2\pi r^4}, \quad (3.19)$$

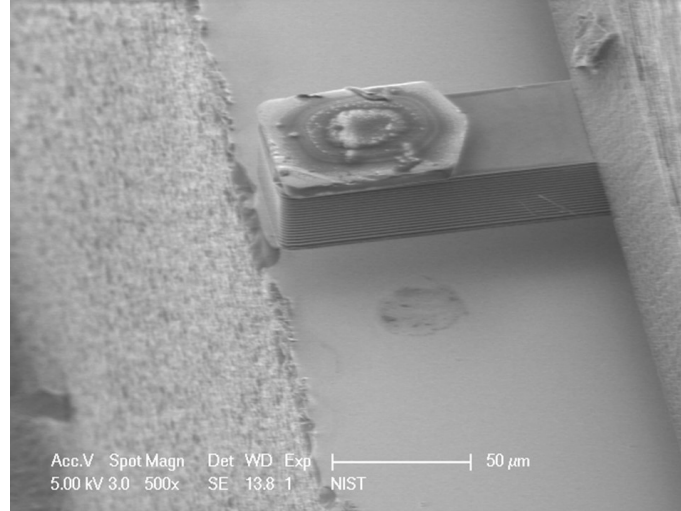


Figure 3.18: Scanning electron microscope image of cantilever. The silicon cantilever has a  $60 \times 85 \times 9 \mu\text{m}$  CoNiMnP magnet glued to it's tip.

where  $\delta z$  is the cantilever tip displacement and  $r$  is the distance from the tip of the cantilever. This expression is a good approximation at large distances. For a more realistic estimate of the field closer to the tip of the cantilever, we numerically integrated over the magnet geometry assuming a single domain [90] (see appendix C).

### Capacitive Driving of Cantilever

As can be seen on figure 3.16, the gold coated side of the cantilever is grounded through the gold rails. Directly below the cantilever there is a gap, followed by a gold counter electrode. The cantilever can be capacitively driven by applying a dc + ac voltage between the electrodes, given by

$$v = v_{dc} + v_{ac} \cos(\omega_0 t), \quad (3.20)$$

where  $\omega_0$  is the resonance frequency of the cantilever which is given by



$$\omega_0 = \frac{\kappa}{0.24m_c + M}, \quad (3.21)$$

where  $m_c$  is the mass of the cantilever, and  $M$  is the mass of the magnet, and  $\kappa$  is the spring constant of the cantilever

$$\kappa = \frac{1}{4}Ew\left(\frac{h}{l}\right)^3, \quad (3.22)$$

where  $E$  is the Young's modulus, and  $w$ ,  $h$ , and  $l$  are the cantilever's width, height, and length, respectively. In our setup,  $w = 60 \mu\text{m}$ ,  $l = 85 \mu\text{m}$ ,  $h = 9 \mu\text{m}$ , and  $E = 190 \times 10^9 \text{ Nm}^{-2}$ , so  $\kappa = 3 \times 10^3 \text{ N/m}$ .

If we approximate the cantilever as a parallel-plate capacitor, the tip displacement is given by

$$\delta z = \frac{Q}{\kappa} \frac{\epsilon_0 A v_{dc} v_{ac}}{d^2}, \quad (3.23)$$

where  $A$  is the area of the plates,  $d$  is the distance between the electrodes,  $\epsilon_0$  is the electric permittivity, and  $Q$  is the mechanical quality factor.

### Cantilever Frequency Measurement

To measure the frequency, quality factor, and displacement of our cantilever, a Helium-Neon gas laser (Thorlabs: HNL020L-JP) with a wavelength of 632.8 nm and a power of 2 mW was used. The laser is bounced on the tip of the cantilever, onto a quadrant photodetector with a bandwidth of 1 MHz (see figure 3.19). The photodiode (Hamamatsu: s4349) on this photodetector is segmented onto 4 different quadrants which allow position sensing, as the laser beam is deflected by the cantilever [91]. The signal from the quadrant photodetector is then processed through an rf lock-in amplifier (Stanford Research Systems: SR844) which is tuned to extract and amplify

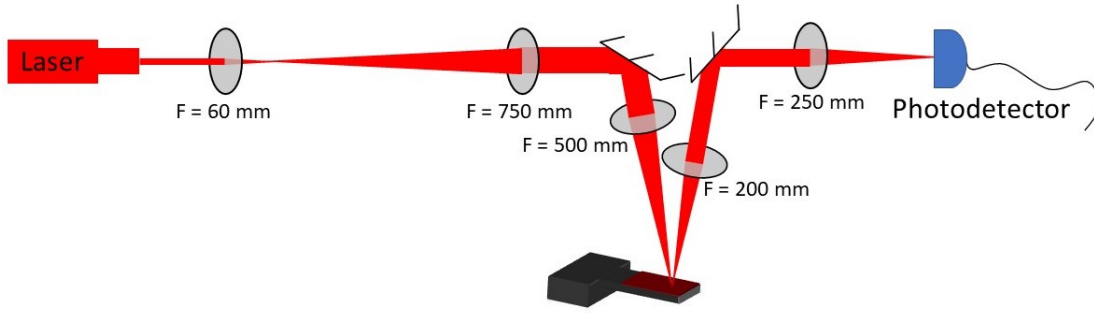


Figure 3.19: Layout of cantilever measurement system. A HeNe laser is reflected from the tip of the cantilever into a quadrant photodetector to measure the tip displacement.

the component of the signal that matches the frequency and phase of the AC signal used to drive the cantilever. The signal from the lock-in amplifier is shown in figure 3.20. A Lorentzian fit to the X quadrature of the lock-in amplifier yields a center (resonance) frequency of 1057.7 kHz and a Lorentzian width (mechanical linewidth) of  $0.67 \pm 0.02$  kHz. The mechanical quality factor is given by

$$Q = \frac{f_r}{\Delta f}, \quad (3.24)$$

where  $f_r$  is the resonance frequency, and  $\Delta f$  is the mechanical linewidth. For the cantilever used in our experiment, the measured quality factor is  $1.6 \times 10^3$ . Using the measured quality factor,  $v_{dc} = 40$  v,  $v_{ac} = 10$  v, and  $d = 9 \mu\text{m}$  on equation 3.23, the calculated tip displacement is  $\delta z = 40$  nm.

### Cantilever Tip Displacement Measurement

The tip displacement was measured by positioning the quadrant photodetector on a 2-dimensional micrometer stage and measuring the displacement on the photodetector

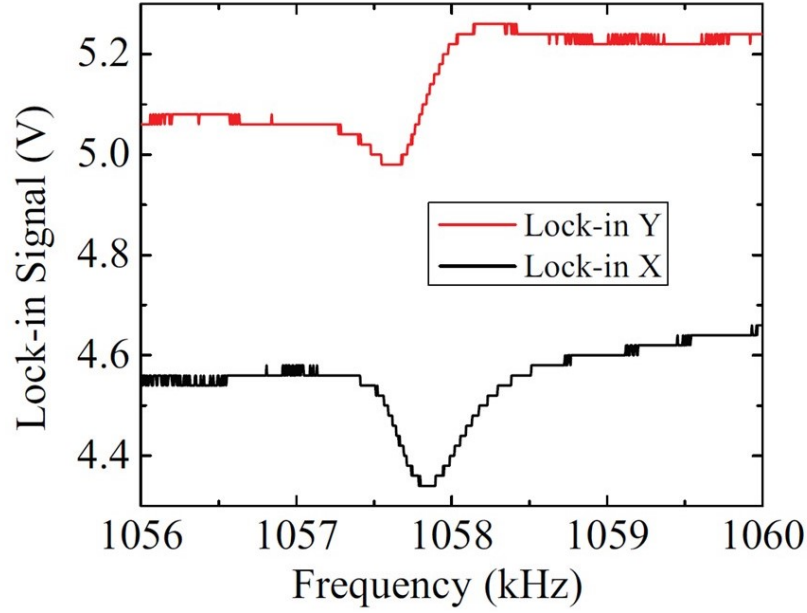


Figure 3.20: (Figure reproduced from [1].) Cantilever resonance. The black and red curve represent the X and Y quadratures of a lock-in amplifier signal.

needed to vary the signal on the photodetector by the same amount that it varies when the cantilever is resonantly driven. As can be seen on figure 3.21, the laser is focused onto the tip of the cantilever, and resized with a telescope before striking the photodetector. Using the matrix optics method, based on our measurements, we calculated a tip displacement of  $\delta z = 34 \text{ nm} \pm 13 \text{ nm}$ , which agrees with our theoretical estimation of 40 nm. The uncertainty in this measurement could be reduced if the laser were to be focused to a tighter waist size at the cantilever tip.

### Thermoelastic Dissipation

It has been demonstrated that thermoelastic internal friction is a fundamental damping mechanism in silicon cantilevers with thicknesses in the order of  $10 \text{ } \mu\text{m}$  [92]. Thermoelastic internal friction is a damping mechanism that occurs when a mate-

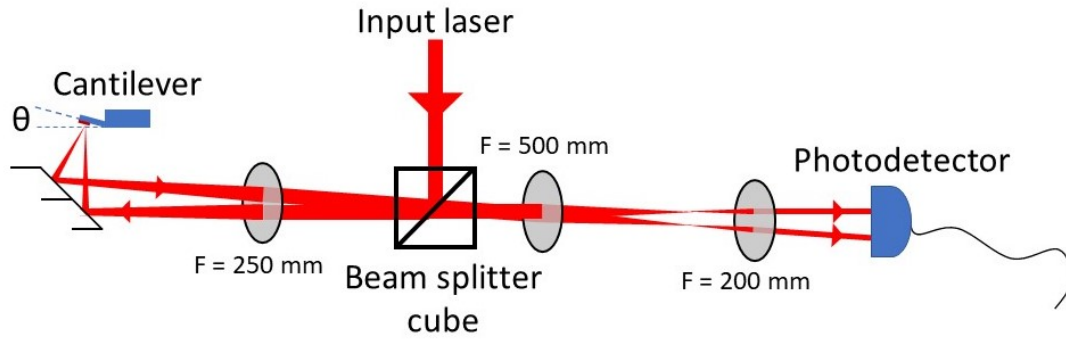


Figure 3.21: Cantilever tip displacement measurement layout. When the cantilever is at rest, the beam retro-reflects and strikes the photodetector at a different spot than when the cantilever is at its maximum displacement position. By measuring the displacement on the photodetector, the cantilever's tip displacement can be determined.

material is subjected to tensile and compressive stress. As a material is mechanically deformed, the work is transformed into elastic potential energy and thermal energy. The temperature of the regions undergoing tensile stress decreases; while on the regions undergoing compressive stress, the temperature increases. When the temperature equilibrates among these regions, the thermal gradient is lost and can't be elastically recovered [92].

Following the work done by Yasumura, et al [93], the thermoelastic-limited mechanical quality factor,  $Q_{TE}$  can be expressed in terms of its material dependencies  $\Gamma(T)$ , and of the cantilever's characteristics  $\Omega(f)$

$$\Gamma(T) = \frac{\alpha^2 T E}{4 \rho C_p}, \quad (3.25)$$

where  $\alpha$  is the coefficient of thermal expansion,  $T$  is the cantilever temperature,  $E$  is the modulus of elasticity,  $\rho$  is the mass density, and  $C_p$  is the specific heat.

The other determining factor is the cantilever's characteristics

$$\Omega(f) = \frac{2f/F_0}{1 + (f/F_0)^2}, \quad (3.26)$$

where  $f$  is the cantilever frequency, and  $F_0$  is the characteristic damping frequency given by

$$F_0 = \frac{\pi\kappa}{2\rho C_p t^2}, \quad (3.27)$$

where  $\kappa$  is the thermal conductivity of the material, and  $t$  is the thickness of the cantilever beam. The thermo-elastic quality factor is then given by

$$Q_{TE} = \frac{1}{2\Gamma(T)\Omega(f)}. \quad (3.28)$$

In our setup, from equation 3.27, and table 3.4, the characteristic damping frequency at room temperature is  $F_0 = 231$  kHz, meaning that the effects of thermo-elastic dissipation are expected in cantilevers with resonance frequencies in the hundreds of kilohertz. From equation 3.28, the thermo-elastic-limited quality factor for a cantilever like ours is  $2 \times 10^4$ . Similar mechanical quality factors were measured for our cantilever before adding the magnet and coating the cantilever with gold. These two processes reduced the quality factor below  $10^4$ . Also, as the cantilever ages, a decrease in the quality factor has been observed, the reasons for this have not been studied by our research group.

### 3.5.2 U-trap Layer

Underneath the copper mirror, the first of our atom chip layers is located. This layer contains wires with a 'U' and a 'Z' shape. In this experiment, only the 'U' shaped

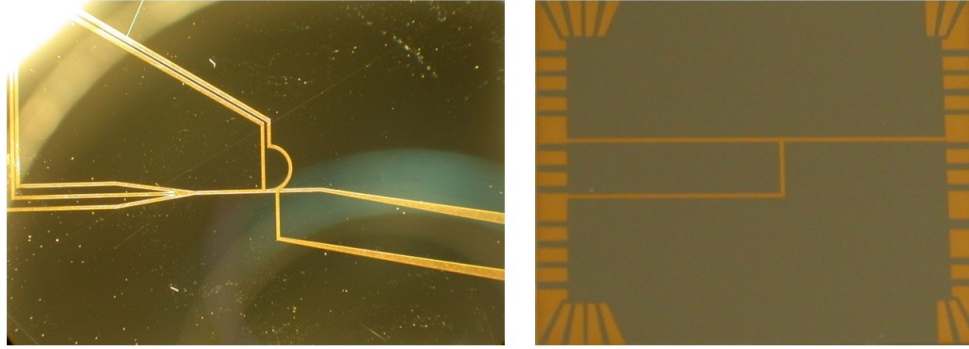


Figure 3.22: Atom chip. (Left) Guiding / P-trap layer. (Right) U-trap layer.

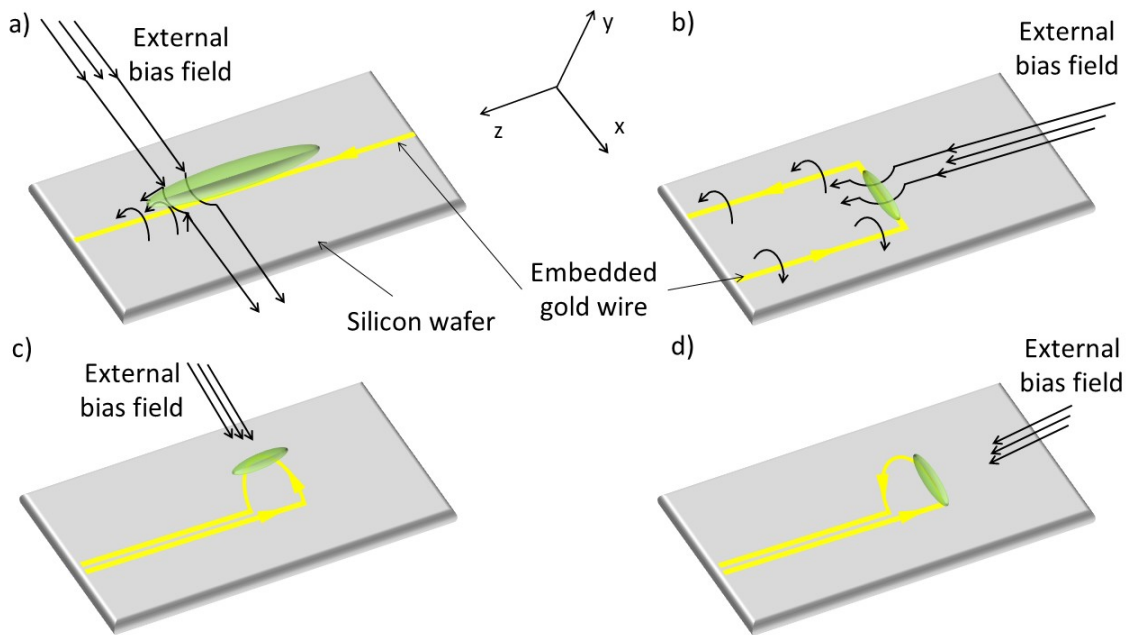


Figure 3.23: Atom chip architectures used in our experiment. a) Guiding trap. An external magnetic field perpendicular to the wire, creates a trap parallel to the wire. Note the trap has no bounds on the ends of the wire. b) U-trap. Similar to the guiding trap, the trap is created parallel to the wire. The field from the two sides of the 'U' put bounds on the long side of the trap. c) and d) P-Trap. Depending on where the external bias field points, the cloud of atoms can be trapped in some region of the curved part of the 'P' shaped wire.

Parameter	Silicon	Units
$\alpha$	$2.6 \times 10^{-6}$	$K^{-1}$
E	$190 \times 10^9$	$Nm^{-2}$
$\rho$	$2.33 \times 10^3$	$kgm^{-3}$
$C_p$	$0.7 \times 10^3$	$Jkg^{-1}K^{-1}$
$\kappa$	$1.5 \times 10^2$	$Wm^{-1}K^{-1}$

Table 3.4: (Adapted from ref. [93].) Thermoelastic constants for single-crystal silicon.

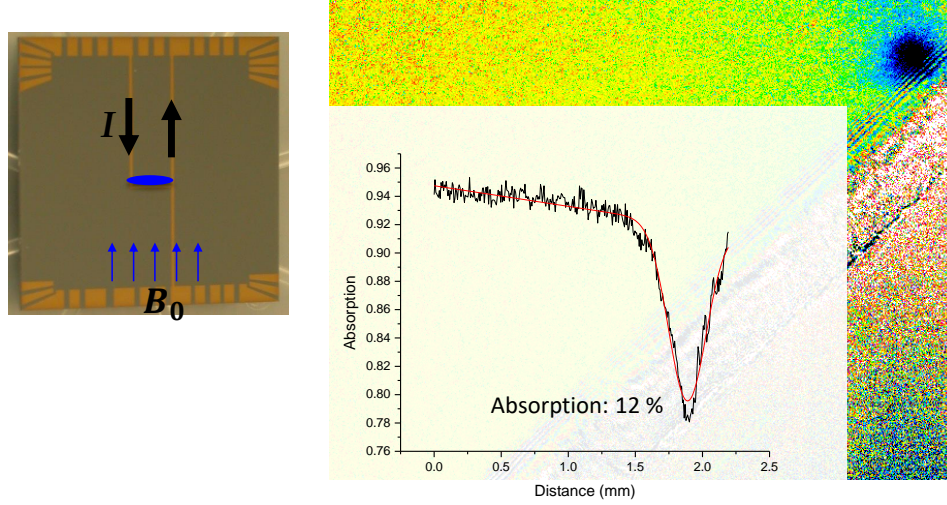


Figure 3.24: U-trap. (Left) Representation of U-trap location on the chip. (Right) Side view absorption image of U-trap, where the dark blue region shows the most optically dense area of the atom cloud.

wire is used. The wires in this layer are  $25 \mu m$  deep and  $300 \mu m$  wide.

The diagonal coils can produce an external bias magnetic field, which in combination with the magnetic field produced by running 8 A of current through the silicon embedded U-shaped gold wire, produces a trapping site at the base of the U-wire (see figure 3.23b). This magnetic trap is tapered on the ends by the field produced by the two side-wires that form the 'U', and by the bias field. This results in a cigar-shaped cloud of atoms, trapped very close to the copper mirror surface. The distance from the cloud to the chip is set by the external bias field.



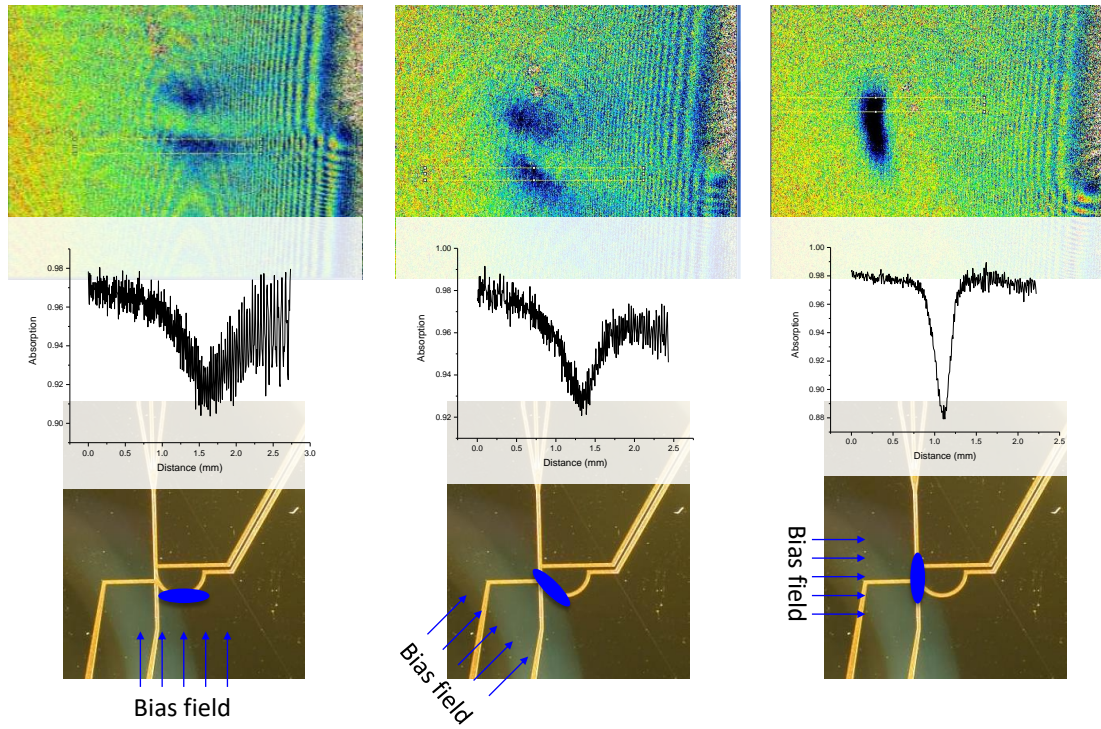


Figure 3.25: P-trap rotation. As the external bias field's direction is changed, the cloud rotates along the curved part of the 'P'. (Top) Front view absorption images of P-cloud. (Middle) Absorption lineouts of atom cloud. (Bottom) Representation of P-trap location on the chip.

### 3.5.3 Guiding / P-trap Layer

The second layer on the atom chip is designed to be used in 3 different configurations which can be seen on figure 3.22: a 'Z' shaped configuration which is not used in this experiment, a 'P' shaped wire is used to rotate the atom cloud by  $90^\circ$ , and a straight wire is used to guide the cloud parallel to the wire. All of the wires on this layer are  $15\ \mu\text{m}$  deep and  $150\ \mu\text{m}$  wide.



### P-trap

The P-wire sits directly below the U-wire. To transfer the atoms from the U-wire to the P-wire, the magnetic fields of both traps must be matched. After the atoms are transferred to the P-trap, the external magnetic field is slowly rotated, the cloud of atoms follow this rotation along the curved part of the 'P' (see figure 3.23c, 3.23d, and 3.25). If the rotation is done quickly, the atoms will gain momentum and escape the trap. If it's done slowly, the cloud's population will decrease due to background gas collisions. To maximize the preservation of atoms in the trap, the rotation speed must match the atoms rms velocity. The purpose of this rotation is to align the cigar-shaped cloud of atoms with the guiding wire (see figure 3.22).

### Guiding-trap

The guiding trap is used to transport the atoms from the center of the chip to the edge of the chip, about 0.8 cm away, where the cantilever is located. The guiding wire, in combination with an external bias magnetic field perpendicular to the wire creates a trap directly above the wire with no axial bounds. An external gradient field is used to confine the atoms on the long side of the wire. Without this gradient field, the atoms would spread along the whole wire and therefore, the optical density would get reduced, making it harder to image the cloud of atoms, and eventually losing atoms on the edges of the wire (figure 3.26). The gradient field is produced by running 20 A of current on the anti-Helmholtz diagonal coils.

At first, the gradient field is used to confine the atoms along the wire at the same location where the rotated P-trap is. To do this, the magnetic field minimum must be located where the atoms are. By changing the bias field, the field minimum is

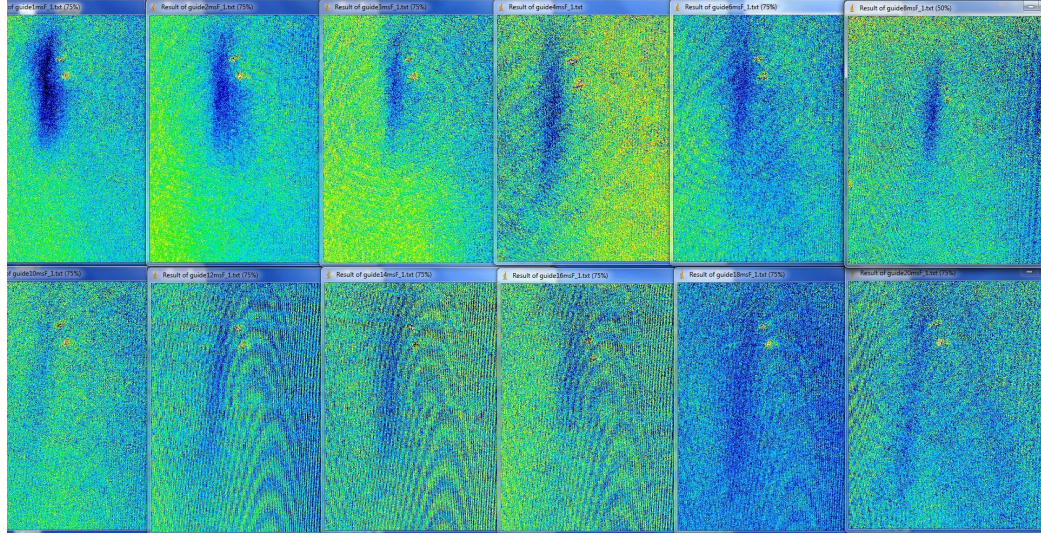


Figure 3.26: Time progression of the guiding trap when no trapping bounds are added to the long side of the trap. The density of the cloud decreases as the atoms spread along the wire. The top left picture was taken after 1 ms of turning the guiding trap on, while the bottom right picture 20 ms after turning the guiding trap on.

shifted. This allows the atoms to move along the wire as the field minimum location is moved. The whole magnetic transport of the atoms occurs in about 200 ms.

### 3.6 Diagnostics

To study the effectiveness of the various traps throughout the experiment, a few diagnostics methods are utilized. Calculating the MOT temperature is important when determining the trap depth of further traps. Monitoring the population of trapped atoms is needed to optimize each stage of the experiment as a large number of trapped atoms is desirable. Finally, knowing the decay rate of our magnetic trap allows determining if the atom number is decaying due to an external effect.

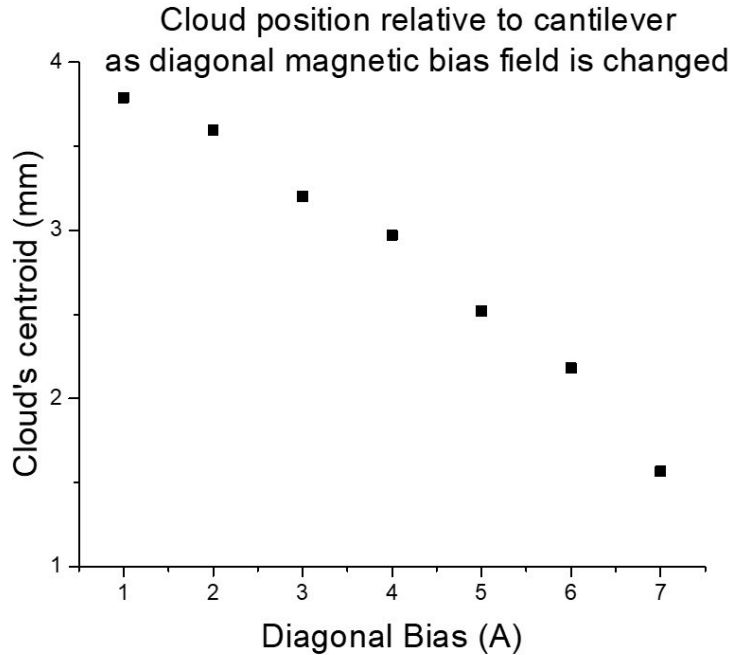


Figure 3.27: Cloud transport along guiding wire by changing bias field.

### 3.6.1 MOT Temperature

To calculate the temperature of the atoms trapped by the MOT we use a cloud expansion method. After molasses cooling the atoms, the cooling laser, as well as the trapping magnetic fields are switched off for a variable period of time, then the cloud is imaged. The process is repeated for several different wait periods. When the cooling is turned off, the cloud of atoms will expand as they are no longer confined. The expansion rate will occur at the average velocity of the molasses-cooled atoms.

From the equipartition theorem, we know that the average kinetic energy per degree of freedom of a sample of atoms in thermal equilibrium is

$$\langle E_k \rangle = \frac{1}{2} k_B T, \quad (3.29)$$

where  $k_B$  is Boltzmann's constant and  $T$  is the atom's temperature.

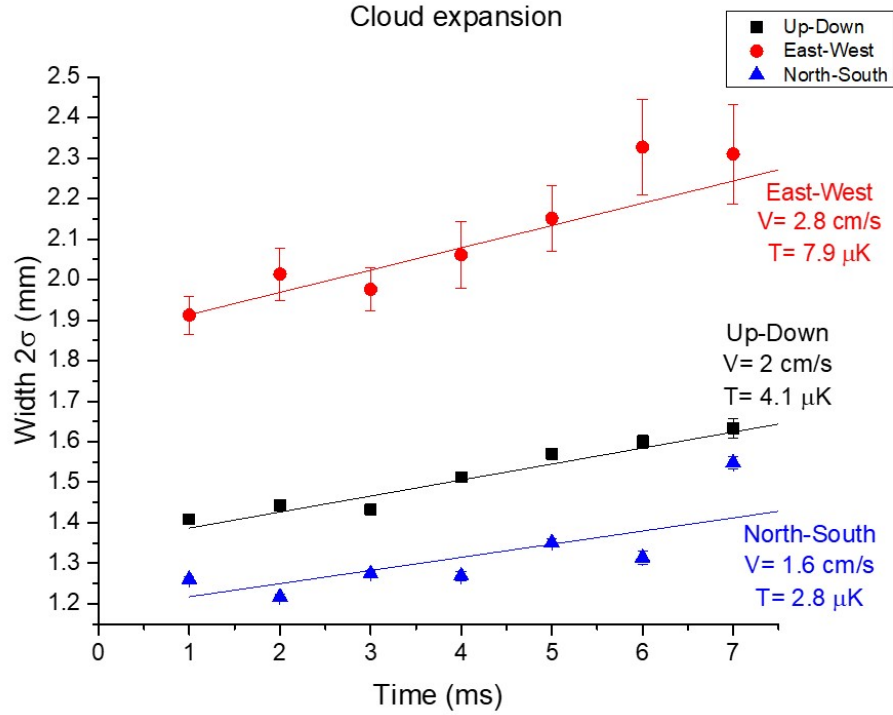


Figure 3.28: After a variable time with the cooling off, the cloud's width is measured, the expansion rate of the cloud is computed to calculate the temperature. Differences in velocities along different axis are due to the fact that the atoms have not fully thermalized when their temperature is measured.

The kinetic energy can also be computed by knowing the velocity, or expansion rate of the atoms by

$$E_k = \frac{1}{2}mv^2, \quad (3.30)$$

where  $m$  is the atomic mass of Rubidium ( $1.44 \times 10^{-25} \text{ kg}$  [66]).

From equations 3.30 and 3.29, we can solve for  $T$ , as follows:

$$T = \frac{mv^2}{k_B}, \quad (3.31)$$

where  $v$  represents the atom's rms velocity.

As seen on figure 3.28, in our experiment, we have measured velocities below 5 cm/s, corresponding to temperatures below  $10 \text{ } \mu\text{K}$ , which is expected for molasses

cooled Rb atoms. Differences in velocities along different axis are due to the fact that the atoms have not fully thermalized when their temperature is measured because of the low collision rates.

### 3.6.2 MOT Population

The population of atoms trapped can be calculated by measuring the cloud width and its optical depth. The optical depth measures how much light gets absorbed as it travels through a material, and it is given by

$$OD = n\sigma l, \quad (3.32)$$

where  $n$  is the cloud's atom density,  $l$  is the cloud's width along the optical axis, and  $\sigma$  is the scattering cross section given by [66]

$$\sigma = \frac{\sigma_0}{1 + 4(\Delta/\Gamma)^2 + I/I_{sat}}. \quad (3.33)$$

Here  $\Delta = \omega - \omega_0$  is the laser detuning,  $\Gamma$  is the decay rate (for the D2 transition of  $^{87}\text{Rb}$ ,  $\Gamma = 38.117 \times 10^6 \text{ s}^{-1}$  [66]),  $I$  is the imaging laser intensity,  $I_{sat}$  is the saturation intensity (for  $^{87}\text{Rb}$   $|F = 2, m_F = \pm 2\rangle \rightarrow |F' = 3, m'_F = \pm 3\rangle$ ,  $I_{sat} = 1.669 \text{ mW/cm}^2$  [66]), and  $\sigma_0$  is the on-resonance cross section, which for a 2-level atom approximation, is defined as

$$\sigma_0 = \frac{\hbar\omega\Gamma}{2I_{sat}}, \quad (3.34)$$

where  $\omega$  is the laser frequency.

The optical depth can be obtained experimentally by studying the light transmitted through a sample and using the following equation, where  $T$  is the transmitted light:

$$T = \frac{I}{I_0} = e^{-OD}. \quad (3.35)$$

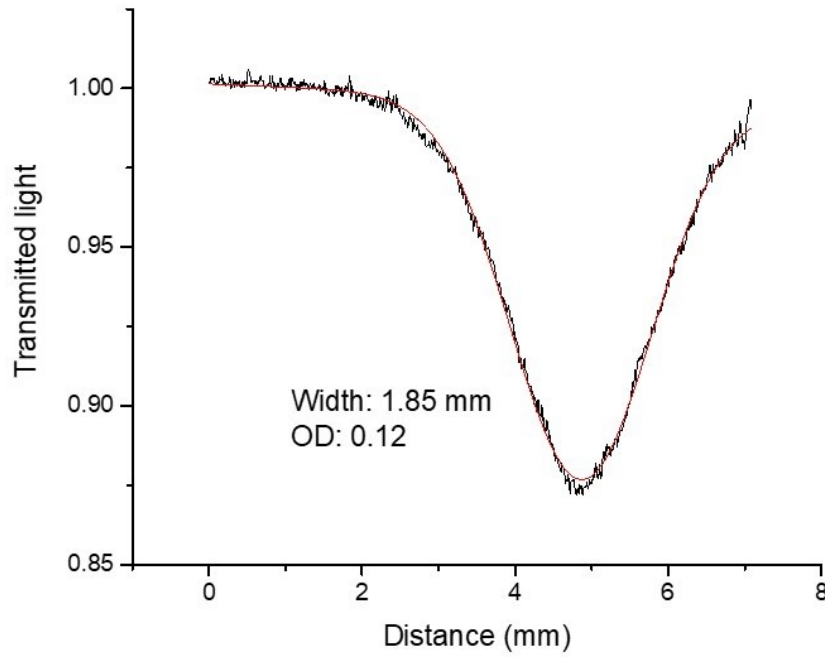


Figure 3.29: Atom cloud lineout on North-South axis. In this example, the cloud's optical depth is 0.128. The cloud's width ( $1/e^2$  radius) is 1.85 mm.

Parameter	Symbol	Experimental measurement	Units
Cloud width	$l$	1.85	mm
Optical density	OD	0.128	-
Laser intensity	$I$	0.025	$mW/cm^2$
Imaging laser detuning	$\Delta$	0	-

Table 3.5: Experimental measurements of cloud after molasses cooling.

From the data on table 3.5, the MOT in our experiment has an atom density of  $2 \times 10^8$  atoms/ $cm^3$ . The total number of trapped atoms is given by

$$N = nV, \quad (3.36)$$

where  $V$  is the volume of the atom cloud, which in our case is about  $27 \text{ mm}^3$ . Therefore, there are about  $6 \times 10^6$  atoms in the cloud after molasses cooling.

### Additional Approximation to MOT Population

A better estimate of the number of atoms can be done by studying in detail the transmission on a single image. For the purposes of this dissertation, a precise estimation of the number of atoms is not needed, but a more precise approximation will nevertheless be explained. Consider a small region of an image of a cloud of atoms, for example a single pixel at location  $x, y$  in the picture. The transmission is not uniform within the picture. In a given pixel, the measured transmission is a result of the absorption of light due to a number of atoms given by

$$N_{x,y} = \frac{OD_{x-y} A_{x,y}}{\sigma}, \quad (3.37)$$

where  $\sigma$  is the scattering cross-section,  $A_{x,y}$  is the area of the pixel, and  $OD_{x,y}$  is the optical depth at pixel  $x, y$ . The total number of atoms is the sum of the number of atoms in each pixel,

$$N = \frac{1}{\sigma} \sum_x \sum_y OD_{x-y} A_{x,y}, \quad (3.38)$$

where the sum is performed over all the pixels in the image.

### 3.6.3 Magnetic Trap Lifetime

The lifetime of the P-trap was studied by measuring the optical density in absorption images of the P-trap as a function of time. In figure 3.30, it can be seen how the P-trap absorption decays with time, this is expected as atoms fall off the trap primarily because of background gas collisions. An exponential fit to the data yields a decay time of  $157 \text{ ms} \pm 31 \text{ ms}$ . Similar decay rates are expected for the other magnetic traps in our experiment.

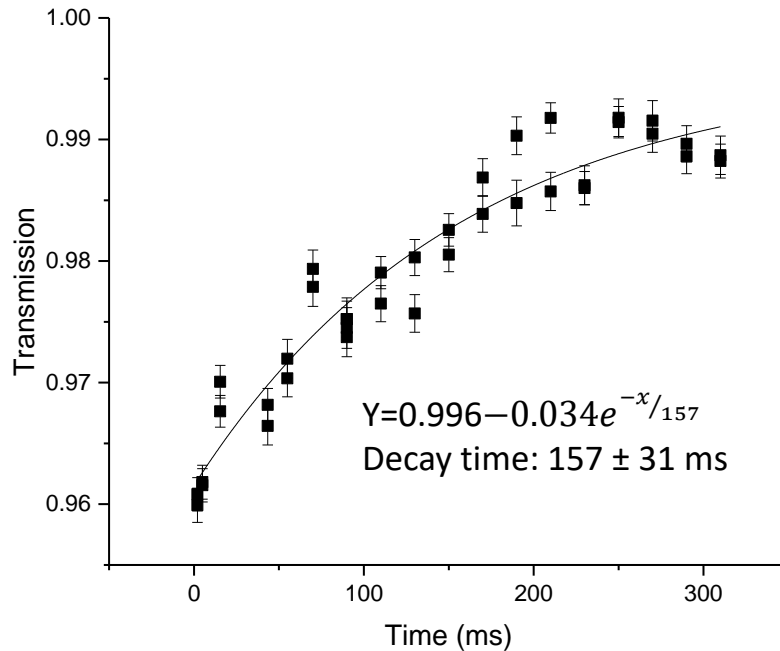


Figure 3.30: P-trap lifetime. Using absorption imaging to monitor the optical density of the P-trap as a function of time, we determined a magnetic lifetime of  $157 \text{ ms} \pm 31 \text{ ms}$ .

### 3.7 Landau-Zener Theory

A system whose eigenstates cross depending on a variable in its Hamiltonian, can have the degeneracy of these two states broken by a perturbation that couples the two levels [94]. A transition between the levels is then possible and can be analyzed using the Landau-Zener theory [95]. The probability of transitioning between the two states, for a time-dependent perturbation is given by [94]

$$P = 1 - e^{-\gamma} \quad (3.39)$$

$$\gamma = \frac{2\pi}{\hbar} \frac{V_{12}^2}{dE/dt}, \quad (3.40)$$



where  $E$  is the difference between the eigenenergies and  $V_{12}$  is the matrix element of the perturbation that couples the two states.

Using equations 3.39 and 3.40, we can calculate the probability of an atom, in the presence of a magnetic field  $B$ , to transition from the Zeeman state  $m_F = 2$  to  $m_F = 1$  when a perturbation couples the two states such that  $V_{12} = \hbar\Omega$ . Each state has an energy given by equation 2.12, the energy difference between the states is

$$E = E_2 - E_1 = 2g_F\mu_B B(x) - g_F\mu_B B(x). \quad (3.41)$$

The landé factor is  $g_F = 2$ , so

$$E = 2\mu_B B(x), \quad (3.42)$$

$$\frac{dE}{dt} = 2\mu_B \frac{dB}{dx} \frac{dx}{dt} = 2\mu_B v \frac{dB}{dx} \quad (3.43)$$

where  $v$  is the rate at which the energy changes, which in our example is the velocity of the atom.

Using equations 3.39, 3.40, and 3.43, we obtain

$$P = 1 - e^{-(\pi\hbar\Omega^2)/(\mu_B v B')}, \quad (3.44)$$

where  $B'$  is the gradient of the magnetic field.

### 3.8 Magnetic Coupling of Atoms to Cantilever

The goal of this experiment is to induce Zeeman-state transitions in magnetically trapped atoms by oscillating a cantilever with a magnet on its tip located nearby the atoms.

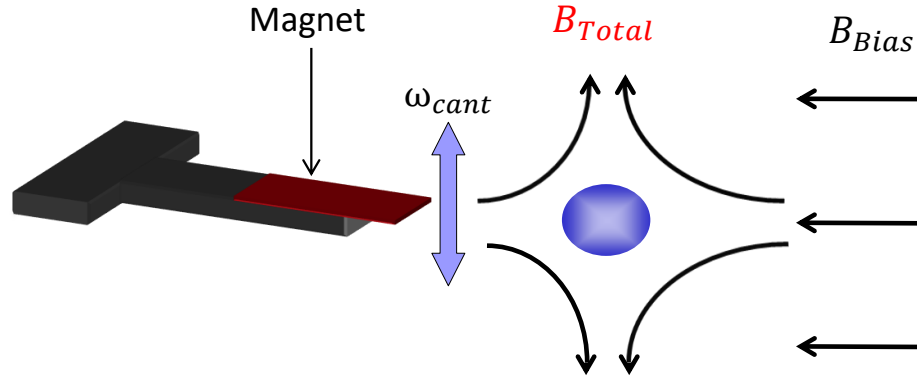


Figure 3.31: A cantilever with a magnet on its tip oscillates near a sample of magnetically trapped  $^{87}\text{Rb}$  atoms. The RF magnetic field produced by the cantilever induces Zeeman-state transitions in the atoms.

### 3.8.1 Zeeman-State Transitions

The atoms are subjected to an external magnetic field and to the magnetic field produced by the tip of the cantilever. Atoms with a Larmor frequency that matches the cantilever's oscillating frequency will have their spin undergo a precession about the net magnetic field direction, resulting in a Zeeman-state transition. The Larmor frequency is given by

$$\omega_L = -\gamma B_T \quad (3.45)$$

where  $\gamma$  is the gyromagnetic ratio, which for  $^{87}\text{Rb}$  is 0.7 MHz/G; and  $B_T$  is the total magnetic field. Notice that the Larmor frequency depends on the total magnetic field which varies with position.

The spin transitions will occur at the Rabi frequency

$$\Omega_R = \gamma B_{\perp}. \quad (3.46)$$

Here  $B_{\perp}$  is the component of the oscillating magnetic field perpendicular to the static

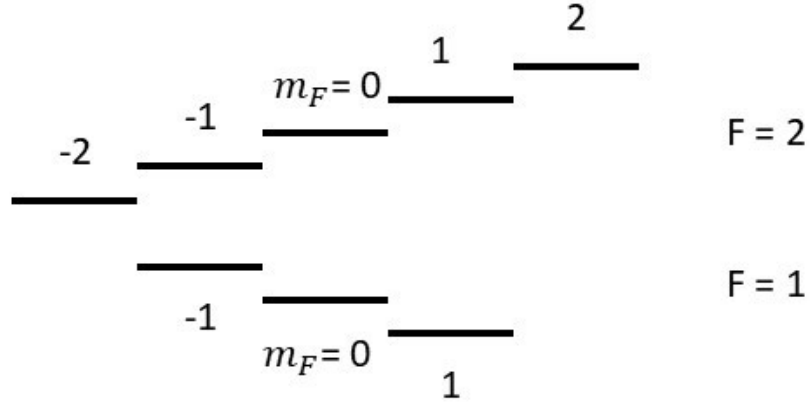


Figure 3.32: Energy diagram of  $m_F$  magnetic sublevels in  $^{87}\text{Rb}$  ground state. The atoms are trapped in the  $F = 2$ ,  $m_F = 2$  sublevel.

field. Using equation 3.19 for the cantilever's field in the dipole limit, we have

$$\Omega_R = \frac{3\gamma m \mu_0 \delta z}{4\pi r^4}. \quad (3.47)$$

The Rabi frequency must be comparable to the trap frequency for maximum efficiency.

Equation 3.44, can then be updated with the Rabi frequency:

$$P = 1 - e^{-(\pi \hbar \Omega_R^2)/(\mu_B \nu B')}. \quad (3.48)$$

Notice the strong dependence on  $r$ , the distance from the tip of the cantilever; as well as from  $\delta z$ , the cantilever tip displacement.

### 3.8.2 Zeeman-State Transition Detection

The atoms are magnetically trapped in the  $F = 2$  ground state of  $^{87}\text{Rb}$  (see figure 3.1). In this hyperfine level, there are 5 sublevels:  $m_F = 2, 1, 0, -1, -2$  (see figure 3.32). As discussed in section 2.2, the atoms on the sublevels  $m_F = 2$  and  $m_F = 1$ ,

are low field seeking atoms. The force on atoms on this sublevel attracts them to the local magnetic field minima, i.e. the center of our magnetic trap; these magnetic states are therefore called trapped states. The atoms in the sublevels  $m_F = -2$  and  $m_F = -1$  are high field seeking atoms. These atoms are repelled from the trap center; these magnetic states are called anti-trapped states. The  $m_F = 0$  state is called an untrapped state since atoms here are neither pulled to the trap center nor are they pushed away from it.

We trap our atoms in the  $m_F = 2$  level. Driving transitions towards the lower  $m_F$  levels will cause the atoms to escape the magnetic trap when they reach the  $m_F = -1$  and  $m_F = -2$  anti-trapped levels. Detecting successful Zeeman-state transitions of the atoms can be done by monitoring the population of the cloud of atoms. A decrease in population is expected when the atoms transition to the untrapped and anti-trapped states.

### 3.9 Results

Rubidium is released into the vacuum chamber by evaporating atoms in a dispenser. The atoms are heated with DC current, so the rate of evaporation can be controlled at will. The atoms are collected in a mirror-MOT at approximately 2.5 mm above the chip surface (see figure 3.12). The MOT is then transferred closer to the chip by creating a U-MOT, where the gradient is created by the U-shaped wire in the atom chip instead of the Anti-Helmholtz coils. Following this stage, the atom cloud is compressed by reducing the repump laser intensity. Further cooling to 7  $\mu\text{K}$  is achieved by polarization gradient cooling. Next, the cloud of atoms is optically pumped to the  $|F = 2, m_F = 2\rangle$  state (see figure 3.32).

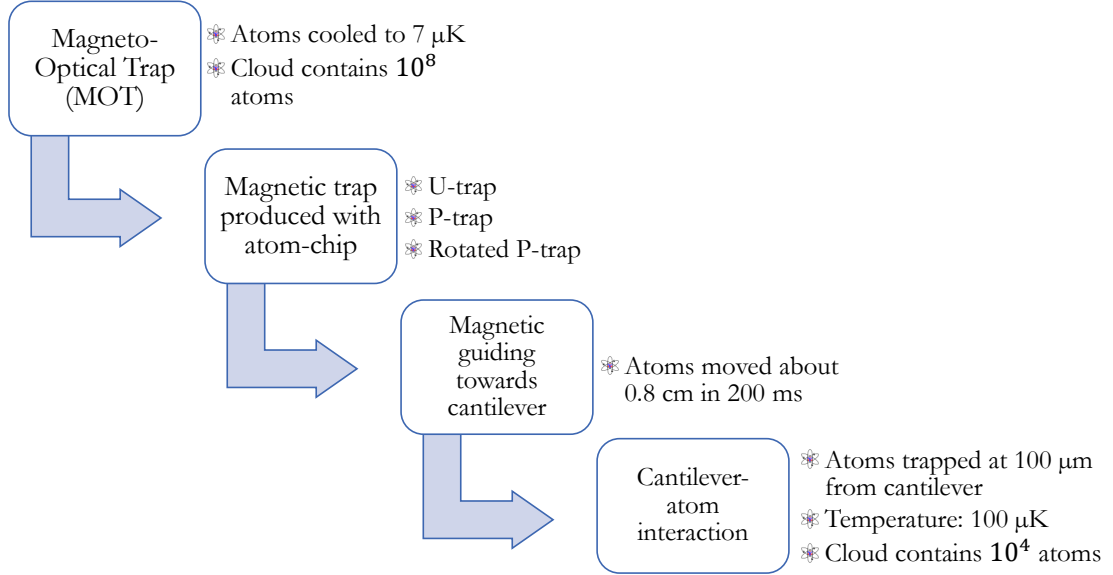


Figure 3.33: Atom preparation flow chart.

After the atoms are pumped to the  $m_F = 2$  state, they are transferred to a magnetic quadrupole trap created by the U-shaped wire on the atom chip and external magnetic fields as discussed in section 3.5.2. The atoms are further transferred to the trap created by the P-shaped wire which allows rotation of the trap axis, such that it is aligned with the guiding wire (see section 3.5.3). The guiding wire, in combination with an external magnetic gradient field produced by the diagonal anti-Helmholtz coils, produces a trap along the guiding wire with a trap center set by an external bias field. Varying this bias field enables the transport of the atoms along the guiding wire and towards the cantilever, located about  $0.8\ \text{cm}$  from the cloud's initial position. Finally, the atoms are transferred to a magnetic trap created by external fields and the field produced by the magnet located on the tip of the cantilever. At this point, the atom temperature has increased to about  $100\ \mu\text{K}$  and the atom number has decreased to about  $10^4$ .

As discussed in section 3.8.2, we expect a decrease in the trap population when

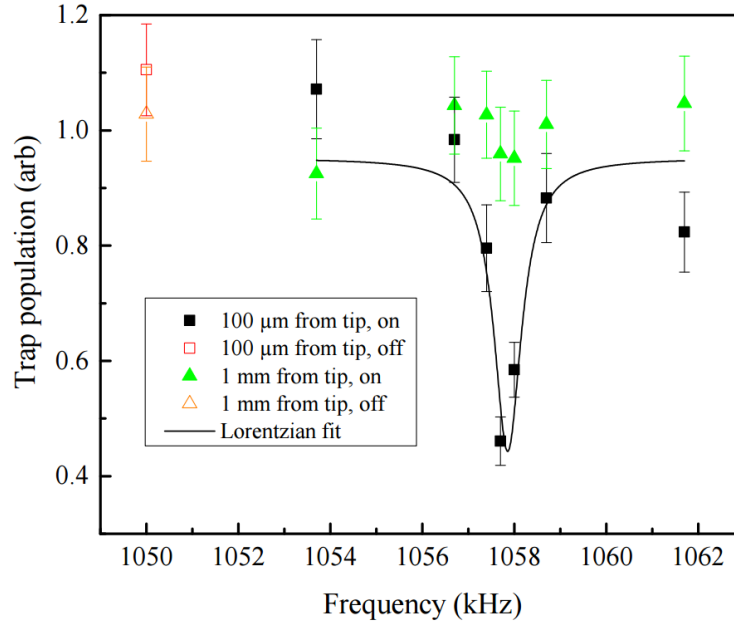


Figure 3.34: (Figure reproduced from ref. [1].) Trap population after interacting with cantilever for 11 ms. A decrease in the trap population is observed when the atoms are 100  $\mu\text{m}$  from the tip of the cantilever and the cantilever is driven on resonance. When the atoms are at 1 mm from the cantilever tip, no significant effect on the trap population is observed.

Zeeman-state transitions are induced in the atoms. Also, from equation 3.44, we expect a large dependence on the distance from the tip of the cantilever to the atoms. As a baseline, we first determined the trap population when the atoms are at 100  $\mu\text{m}$  and at 1 mm from the tip of the cantilever, with the cantilever off. In both cases, the population was measured after the atoms had been at the desired distance from the cantilever for 11 ms. As can be seen on figure 3.34, these two measurements are within error from each other, as expected. Next, the effect of the cantilever was studied when the atoms are at 1 mm from the tip of the cantilever. Because the cantilever effect has a  $1/r^4$  dependence, at 1 mm we expect the effect to be negligible. The atom population was studied as the cantilever was driven at various frequencies, no significant effect was observed at driving frequencies between 1054 and 1062 kHz,

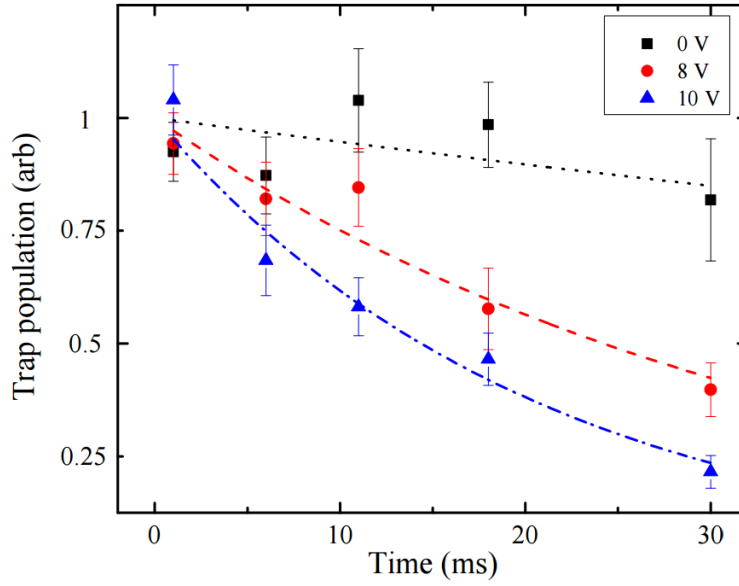


Figure 3.35: (Figure reproduced from ref. [1].) Trap population after varying time of interaction with the cantilever, for different cantilever tip displacement. The dotted lines represent the expected theoretical 1-D Landau-Zener model.

as the population remained comparable to the previously measured population with the cantilever off. The final test was performed by studying the trap population at  $100\text{ }\mu\text{m}$  from the tip of the cantilever. As expected, the trap population dropped to about half when the cantilever was driven on-resonance. A Lorentzian fit to this data yields a peak centered at  $1057.85\text{ kHz}$ , and a width of  $0.73\text{ kHz}$ .

In figure 3.34, the atoms interacted with the cantilever for  $11\text{ ms}$  at various cantilever driving frequencies. In figure 3.35, the interaction time is varied while the driving frequency was kept on-resonance. As can be seen from equation 3.44, the probability of inducing a hyperfine transition in the atoms depends on the amplitude of oscillation of the cantilever tip  $\delta z$ . From equation 3.23, it can be deduced that varying the voltage used to drive the cantilever will result in a change in the tip displacement. The DC voltage was kept constant at  $V_{DC} = 40\text{ V}$ , while the trap popu-

lation was studied at  $V_{AC} = 0, 8, \text{ and } 10 \text{ V}$ . At  $V_{AC} = 0 \text{ V}$ , the cantilever tip will not be displaced. The population decay rate in this case, is caused primarily by background gas collisions. An exponential decay fit to this data yields a time constant of  $184 \text{ ms} \pm 66 \text{ ms}$ , in agreement with the magnetic trap lifetime. When the cantilever is driven at  $V_{AC} = 8 \text{ V}$  and  $10 \text{ V}$ , the population decays much faster and agrees, within a factor of 2, with the theoretical calculations from the 1-D Landau-Zener theory, represented in figure 3.35 by dotted lines. As the actual atomic motion in the trap occurs in three dimensions and can be quite complex, we do not expect exact quantitative agreement for the 1-D calculation. In this calculation, the magnetic gradient was calculated by numerically integrating over the magnet as a single domain. At  $V_{AC} = 8 \text{ V}$ , the fitted decay rate is  $34 \text{ ms} \pm 3.6 \text{ ms}$ , while at  $V_{AC} = 10 \text{ V}$ , the fitted decay rate is  $21 \text{ ms} \pm 3.1 \text{ ms}$ .

### 3.10 Conclusions and Future Directions

In this experiment, Zeeman-state transitions on magnetically trapped  $^{87}\text{Rb}$  atoms were induced by use of a micro-cantilever with a magnet on its tip. These results agree, within error, with the Landau-Zener theory. A similar complimentary experiment could be performed where the cantilever is used to detect Zeeman-state transitions rather than inducing them. To achieve this, the force induced by the atoms must be larger than the thermal-noise limited sensitivity of the cantilever. Thermal noise sets a limit on the minimum detectable force (see appendix B), which is given by [85],

$$F_{min} = \sqrt{\frac{4kk_B T b}{\omega_c Q}}, \quad (3.49)$$

where  $k$  is the spring constant,  $T$  is the effective temperature of the mode in consideration,  $b$  is the bandwidth of the measurement,  $\omega_c$  is the cantilever's natural



frequency, and  $Q$  is the mechanical quality factor. Table 3.6 shows example values for a cantilever with a minimum detectable force of  $28 \text{ aN}/\sqrt{\text{Hz}}$ . Further improvement can be achieved by cryogenically cooling the cantilever to 2 K, as a result, we expect the quality factor to increase by about a factor of 3. For these conditions, the force sensitivity becomes  $1.3 \text{ aN}/\sqrt{\text{Hz}}$ , allowing single-electron spin detection at  $1.1 \text{ }\mu\text{m}$  separation from the tip of the cantilever, as seen on figure 3.36. These experiments should take place in an optical trap, to prevent loss of atoms experiencing state changes. Work is in progress to develop an optical trap near the cantilever.

Parameter	Symbol	Value	Units
Spring constant	$k$	$3 \times 10^{-3}$	N/m
Temperature	$T$	300	K
Bandwidth	$b$	0.1	Hz
Resonance frequency	$\omega_c$	$2\pi \times 70$	kHz
Mechanical quality factor	$Q$	$10^5$	-
Force sensitivity	$F_{min}$	28	$\text{aN}/\sqrt{\text{Hz}}$

Table 3.6: Example values for highly sensitive cantilever

Cooling mechanical oscillators to their quantum ground state [12, 13, 14] could enable nonclassical states of the atomic degrees of freedom to be transferred to the motional states of the resonators and vice versa, with applications in quantum information science [40, 85, 96]. In these setups, mechanical oscillators can provide coupling between photons, spins, and charges via phonons [50, 97, 98, 99, 100]. Such transducers could be useful for quantum networks by allowing coupling between different types of quantum systems, each with different advantages.

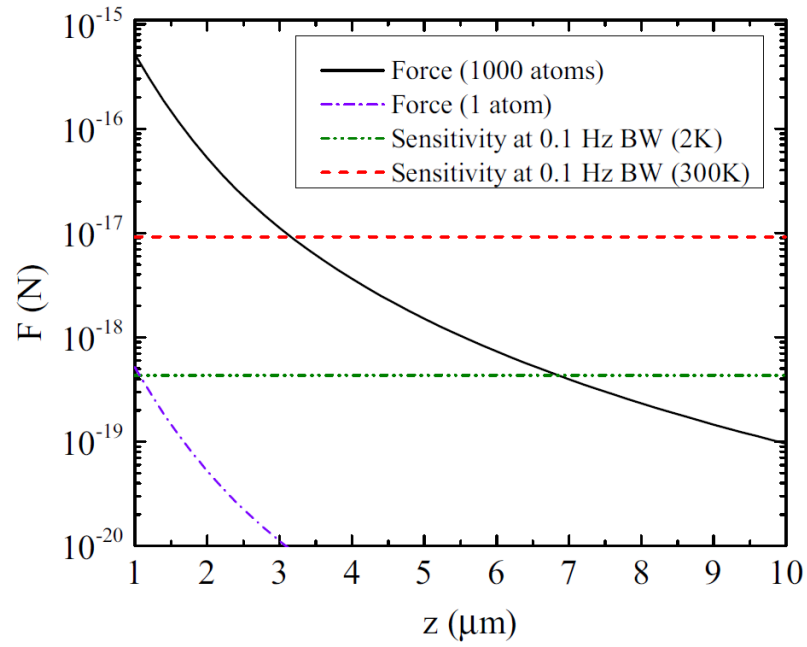


Figure 3.36: (Figure reproduced from ref. [1].) Thermal-noise limited force sensitivity of proposed cantilever as a function of distance from the tip of the cantilever. The solid line represents the force due to 1000 atoms, while the dashed line represents the force due to 1 atom spin. The dashed horizontal lines represent the minimum force sensitivity at 2 K and 300 K.

## CHAPTER 4

### OPTICAL TRAPS

In the second experiment discussed in this dissertation, atoms are optically trapped. Also, a silica sphere is optically levitated. These optical traps work because of the force exerted by light, or radiation pressure force. First deduced by Maxwell in 1873 [101], and observed by Nichols and Hull in 1903 [102], radiation pressure can be understood from the conservation of momentum: if an object absorbs radiation, its momentum changes. The force imparted by the absorption of radiation on a surface of area  $A$  is given by

$$F_{rad} = \frac{IA}{c}, \quad (4.1)$$

where  $I$  is the intensity of the light, and  $c$  the speed of light.

#### 4.1 Gaussian Optics

In our setup, the optical traps are created by focusing the fundamental, or  $TEM_{00}$ , mode of a laser beam. In this mode, the magnetic and electrical field amplitude profiles are described by a Gaussian function. The intensity profile is also described by the Gaussian function [103], and is given by

$$I(\vec{r}, z) = I_0 \left( \frac{w_0}{w(z)} \right)^2 e^{\frac{-2r^2}{w^2(z)}}, \quad (4.2)$$

where  $I_0$  is the intensity at the center of the beam,  $z$  is the distance from the focus,  $w$  is the spot size, and  $w_0$  is the minimum spot size, or waist, of the beam.

The Rayleigh range, is defined as the distance, along the beam propagation direction, from the waist to the place where the area of the cross section is doubled

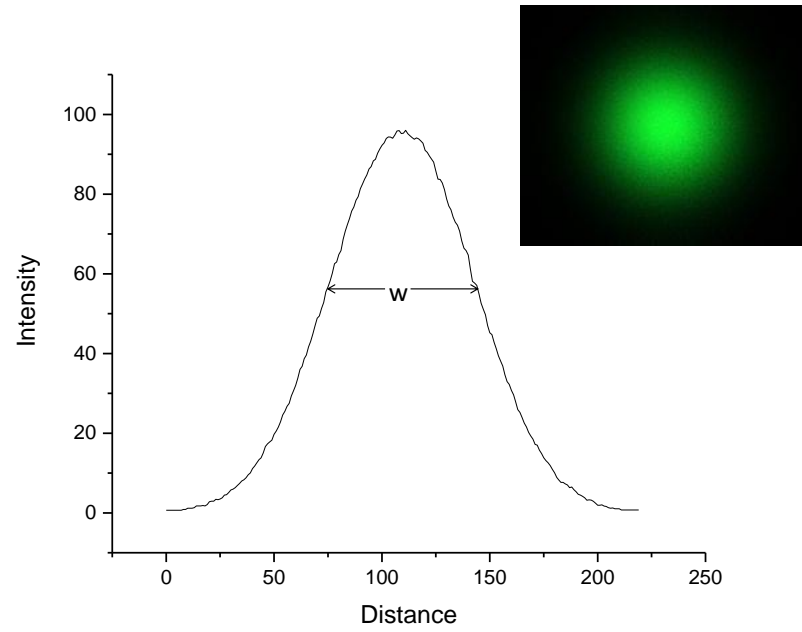


Figure 4.1: Example intensity profile of a Gaussian beam.

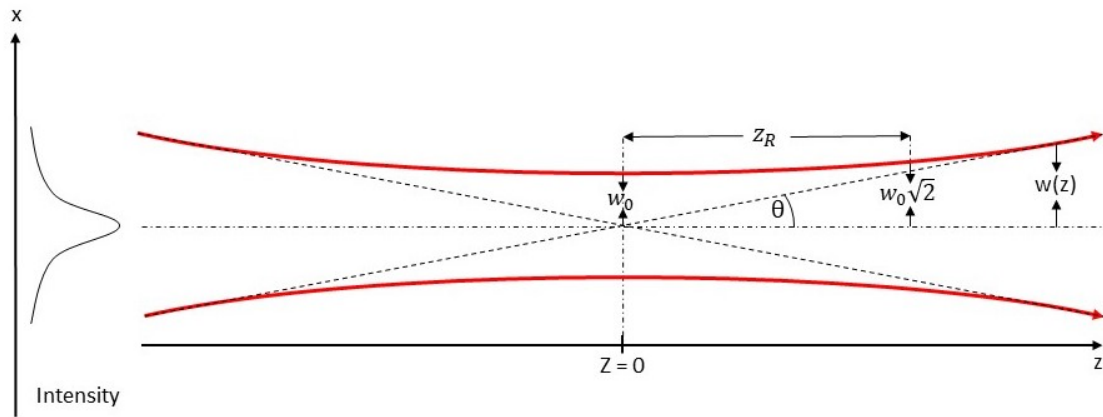


Figure 4.2: (figure adapted from ref. [103].) Spot size of a Gaussian beam.

[104].

$$z_R = \frac{\pi w_0^2}{\lambda}, \quad (4.3)$$

where  $\lambda$  is the wavelength of the laser. The Rayleigh range is a parameter that characterizes the rate at which the spot size grows. Alternatively, the confocal parameter is also used, which is exactly twice the Rayleigh range. At a distance  $z$  from the waist, the spot size is given by

$$w(z) = w_0 \sqrt{1 + z^2/z_R^2}. \quad (4.4)$$

The divergence angle of a Gaussian beam when  $z \gg z_R$  is

$$\theta \approx \frac{w(z)}{z} \approx \frac{w_0}{z_R} = \frac{\lambda}{\pi w_0}. \quad (4.5)$$

Consider a beam with a width  $w = d$ , focused by a lens of focal length  $f$ , the divergence angle is approximately

$$\theta \approx \frac{d}{f}. \quad (4.6)$$

Using equations 4.5 and 4.6, we conclude that the diffraction limited waist produced by a lens depends on its focal length and on the size of the input beam

$$w_0 = \frac{\lambda f}{\pi d}. \quad (4.7)$$

## 4.2 Dipole Force

In 1986, Ashkin, et al [105], reported results that demonstrated the existence of negative radiation pressure due to an axial intensity gradient in a laser beam. This results were further explored to create optical tweezers to trap atoms [17], and in biological applications to trap and manipulate cells, internal parts of cells and molecules [106],

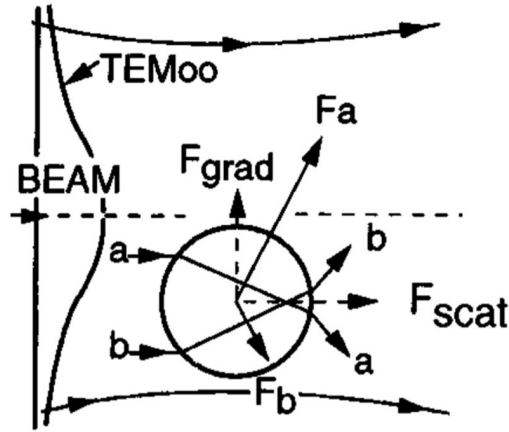


Figure 4.3: (Figure reproduced from ref. [109].) Ray optics diagram of scattering and gradient forces.

viruses and bacteria [107], and even to study the swimming forces of sperm cells [108]. Optical tweezers are created when a trap is formed by a tightly focused laser beam. Depending on its index of refraction, dielectric objects can be trapped using optical tweezers.

#### 4.2.1 Ray Optics Visualization

Ray optics can be used to describe the scattering force and momentum transfer on an object by a single-beam. This approach is valid on the Mie size regime, where the size of the scattering particle is comparable to the wavelength of the light. As seen on figure 4.3, a sphere displaced from the axis of a TEM<sub>00</sub> mode of a focused laser beam, refracts two typical rays (a and b on the figure) symmetrically about the sphere's axis. The ray closer to the beam axis has a higher intensity than the beam further from the axis, therefore the force due to refraction on the first ray ( $F_a$ ) is stronger than the force due to the second ray ( $F_b$ ). The net force can be studied in two components, an axial component pointed in the direction of the incident light

called the scattering force, and a radial component called the gradient force [109]. If the index of refraction of the object is higher than the index of refraction of the medium, the gradient force is directed towards the region of highest intensity of the beam. If the index of refraction of the object is lower than the index of refraction of the medium, the gradient force is directed away from the region of highest intensity of the beam, pushing the object away from the beam. This case does not work for trapping.

#### 4.2.2 Dipole Force Theory

In the presence of an electric field  $\vec{E}$ , like that of a laser beam, a dipole moment  $\vec{p}$  is induced on an object. The interaction energy is given by

$$U_{dip} = -\frac{1}{2} \langle \vec{p} \cdot \vec{E} \rangle, \quad (4.8)$$

where the dipole moment, depends on the electric polarizability  $\alpha$  of the object,

$$\vec{p} = \alpha \vec{E}. \quad (4.9)$$

Equation 4.8 then becomes

$$U_{dip} = -\frac{1}{2} \alpha E^2. \quad (4.10)$$

From equation 2.10, we can derive the dipole, or gradient force:

$$F_{dip} = \frac{1}{2} \alpha \nabla (E^2). \quad (4.11)$$

Since  $E^2$  is proportional to  $I$ , the intensity of the light field, this equation shows the dipole force depends on the gradient of the intensity. The gradient force is a conservative force.

### 4.2.3 Dipole Force for Dielectric Spheres

For a dielectric sphere of radius  $a$ , index of refraction  $n_s$ , in a medium with index of refraction  $n_m$ , illuminated by a linearly polarized Gaussian laser beam of intensity  $I$  and wavelength  $\lambda$ , the scattering force is given by [110]

$$\vec{F}_{scatt}(\vec{r}, \vec{z}) = \hat{z} \frac{128}{3} \frac{\pi^5 a^6 n_m}{c \lambda^4} \left( \frac{m^2 - 1}{m^2 + 2} \right)^2 I(\vec{r}, \vec{z}), \quad (4.12)$$

where  $m = n_s/n_m$ . The gradient force is

$$\vec{F}_{grad}(\vec{r}, \vec{z}) = \frac{2\pi n_m a^3}{c} \left( \frac{m^2 - 1}{m^2 + 2} \right) \nabla I(\vec{r}, \vec{z}). \quad (4.13)$$

As can be seen, the scattering force linearly depends on the intensity of the laser, while the dipole force depends on the gradient of the intensity.

To optically trap a microsphere, the total force on it must be negative, hence

$$\vec{F}_{scatt}(\vec{r}) + \vec{F}_{grad}(\vec{r}) < 0. \quad (4.14)$$

On figure 4.4, the scattering force, gradient force, and total net force are plotted for different laser intensities. As can be seen, the waist size greatly impacts the trap escape potential. Generally, the trap depth should be at least 10 times the temperature of the particle or of the cloud of atoms. This allows the kinetic energy to have a large standard deviation while preserving the trap conditions.

Using equation 2.10, we can deduce the trapping potential from equation 4.13 to be

$$U_{grad}(\vec{r}, \vec{z}) = -\frac{2\pi n_m a^3}{c} \left( \frac{m^2 - 1}{m^2 + 2} \right) I(\vec{r}, \vec{z}). \quad (4.15)$$

In terms of the volume of the sphere  $V$ , equation 4.15 turns into

$$U_{grad}(\vec{r}, \vec{z}) = -\frac{3n_m V}{2c} \left( \frac{m^2 - 1}{m^2 + 2} \right) I(\vec{r}, \vec{z}). \quad (4.16)$$



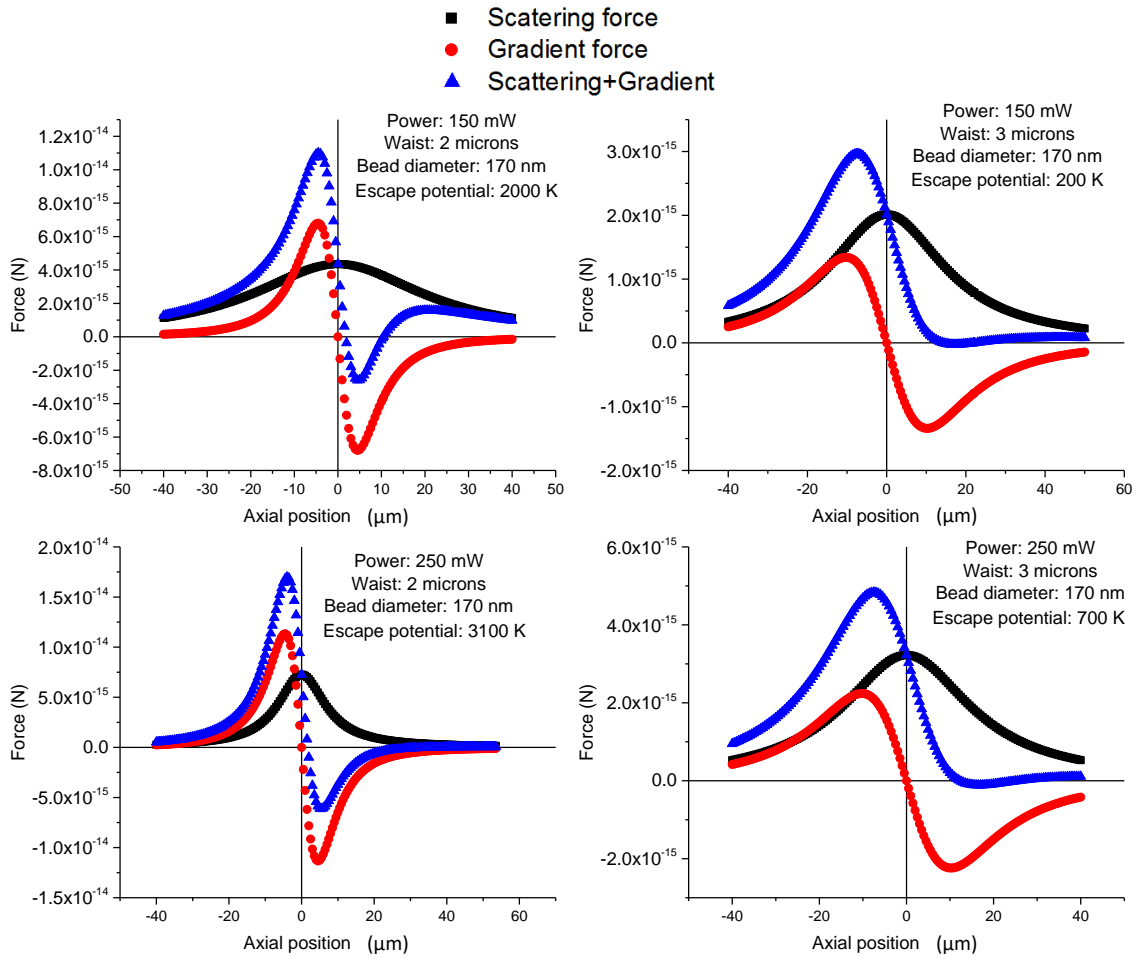


Figure 4.4: Scattering and gradient forces on axial direction for different intensities of a 1596 nm laser beam.

Figure 4.5 shows the bead trap potential for different beam waist, laser power, and bead diameter. As can be seen, the trap potential increases for larger beads, but from equations 4.12 and 4.13, it can be deduced that the scattering force increases due to the sphere radius more rapidly than the gradient force, limiting the trap depth.

The trap frequency can be described in terms of the component along the direction of propagation of the laser beam, or axial direction; and the component perpendicular to the direction of propagation or radial direction. To derive the expressions for the

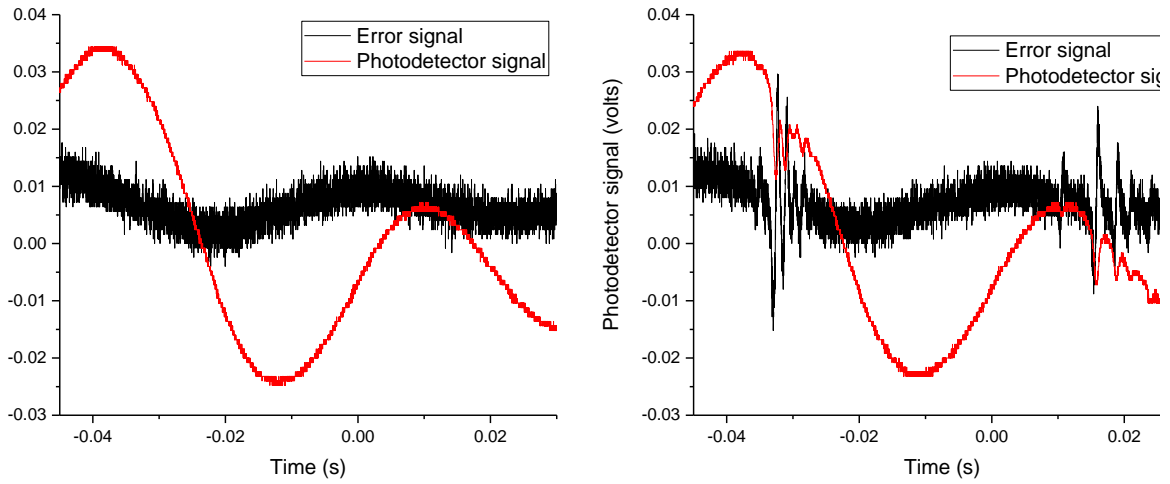


Figure 4.5: Bead trap potential for different beam waist, laser power, and bead diameter. The traps on all plots are formed by a focused 1596 nm laser beam.

trap frequency, we first need to find the components of the gradient force in each of these directions. Using equation 2.10 on equation 4.16 we find the radial component of the gradient force:

$$F_r = -\frac{\partial U_{grad}(\vec{r}, 0)}{\partial r} = \frac{-6n_m V r I_0}{c w_0^2} \left( \frac{m^2 - 1}{m^2 + 2} \right) e^{-\frac{2r^2}{w_0^2}} \quad (4.17)$$

and the axial component of the gradient force:

$$F_z = -\frac{\partial U_{grad}(\vec{0}, \vec{z})}{\partial z} = \frac{-3n_m V I_0}{c} \frac{z \lambda^2}{w_0^4 \pi^2} \left( \frac{m^2 - 1}{m^2 + 2} \right) \frac{1}{\left( 1 + \frac{z^2 \lambda^2}{\pi^2 w_0^4} \right)^2}. \quad (4.18)$$

Taylor expanding the expressions for  $F_r$  and  $F_z$  to first order, gives

$$F_r = \frac{-6n_m V I_0}{c w_0^2} \left( \frac{m^2 - 1}{m^2 + 2} \right) r + O(r^2) \quad (4.19)$$

and the axial component of the gradient force:

$$F_z = \frac{-3n_m V I_0 \lambda^2}{c \pi^2 w_0^4} \left( \frac{m^2 - 1}{m^2 + 2} \right) z + O(z^2). \quad (4.20)$$

Comparing equations 4.19 and 4.20 with Hooke's law:  $F = -kx$ , we can deduce the spring constants of the trap:

$$k_r = \frac{6n_m V I_0}{c w_0^2} \left( \frac{m^2 - 1}{m^2 + 2} \right), \quad (4.21)$$

$$k_z = \frac{3n_m V I_0 \lambda^2}{c \pi^2 w_0^4} \left( \frac{m^2 - 1}{m^2 + 2} \right). \quad (4.22)$$

Finally, we can write the expressions for the trap frequency by using  $\omega = \sqrt{k/m}$ , where  $m = \rho V$  is the mass of the sphere, and  $\rho$  is the density of the sphere

$$\omega_r = \sqrt{\frac{6n_m I_0}{c \rho w_0^2} \left( \frac{m^2 - 1}{m^2 + 2} \right)} = \sqrt{\frac{4U_{depth}}{V \rho w_0^2}}, \quad (4.23)$$

$$\omega_z = \sqrt{\frac{3n_m I_0 \lambda^2}{c \pi^2 \rho w_0^4} \left( \frac{m^2 - 1}{m^2 + 2} \right)} = \sqrt{\frac{2U_{depth} \lambda^2}{V \pi^2 \rho w_0^4}}; \quad (4.24)$$

where  $U_{depth}$  is the trap potential depth defined as  $U_{grad}(0, 0)$  from equation 4.16.

The values of the parameters we typically use in our setup are listed in table 4.1. The calculated radial frequency is 32 kHz, while the axial frequency is 7 kHz, with a trap potential depth of 4200 K, enough to trap spheres at room temperature.

Parameter	Symbol	Value	Units
Laser power	P	250	mW
Laser wavelength	$\lambda$	1596	nm
Waist	$w_0$	1.7	$\mu\text{m}$
Sphere's index of refraction	$n_s$	1.44963	-
Sphere's radius	a	85	nm
Sphere's density	$\rho$	2300	$\text{kg}/\text{m}^3$
Radial frequency	$\omega_r$	32.4	kHz
Axial frequency	$\omega_z$	6.8	kHz
Trap depth	$U_{depth}$	4200	K

Table 4.1: Typical parameters in our experiment.

#### 4.2.4 Dipole Force for Atoms

In the case of atoms illuminated by a focused Gaussian beam with intensity  $I$ , the forces acting on the atoms depend on the atom decay rate  $\Gamma$ , the laser's frequency detuning from resonance  $\delta = \omega - \omega_0$ , and the saturation intensity  $I_{sat}$  [64]

$$F_{scatt} = \hbar k \frac{\Gamma}{2} \frac{I/I_{sat}}{1 + I/I_{sat} + 4\delta^2/\Gamma^2}, \quad (4.25)$$

$$F_{grad} = -\frac{\hbar \delta}{2} \frac{1}{1 + I/I_{sat} + 4\delta^2/\Gamma^2} \frac{\partial I}{\partial z}. \quad (4.26)$$

For atoms, just like for dielectric spheres, the scattering force scales with the intensity, while the dipole force scales with the gradient of the laser intensity. When the laser is on resonance, the gradient force on equation 4.26 is zero. Therefore to optically trap atoms, the laser must be detuned from resonance. Also, for the gradient force to be negative, a requirement for trapping,  $\delta > 0$ , i.e. the laser must be red-detuned. For large detunings,  $|\delta| \gg \Gamma$ , the scattering rate becomes [64]

$$R_{scatt} \simeq \frac{\Gamma}{8} \frac{\Gamma^2}{\delta^2} \frac{I}{I_{sat}}. \quad (4.27)$$

Generally, the scattering rate in a trap must be kept low to reduce heating. Following a similar procedure as in section 4.2.3, the trap potential for atoms can be determined

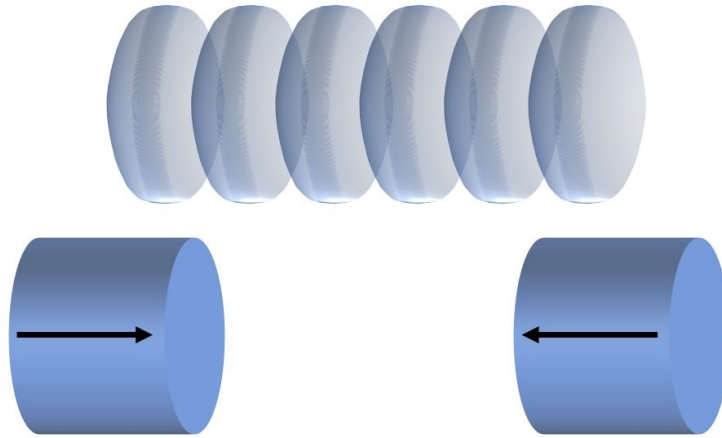


Figure 4.6: Representation of a 1-dimensional optical lattice. Two counter-propagating beams interfere and produce a standing wave.

as

$$U_{grad} = \frac{\hbar \Gamma}{8} \frac{\Gamma}{\delta} \frac{I}{I_{sat}}. \quad (4.28)$$

The trap frequency of the atoms is given in the radial direction by [111]

$$\omega_r = \sqrt{\frac{4U_{grad}}{mw_0^2}} \quad (4.29)$$

just like in the case of the sphere. In the axial direction, the trap frequency is given by

$$\omega_z = \sqrt{\frac{2U_{grad}k^2}{m}}, \quad (4.30)$$

where  $k$  is the laser wave number, and  $m$  is the mass of the atoms.

### 4.3 Optical Lattice

As can be seen in equations 4.13 and 4.26, the dipole force is stronger when there is a strong intensity gradient. If a standing wave is created by the interference of two overlapping counter-propagating beams, regions of high intensity and low intensity

are separated by a distance of  $\lambda/2$ . This gives rise to very high intensity gradients which makes the trap potential in an optical lattice deeper than in a single dipole trap, given the same intensity and waist. In our experiment, only the atoms will be trapped in an optical lattice, while the microsphere will be trapped in a single dipole trap. The lattice potential depth for atoms is given by [112]

$$U_{lat} = \frac{3\pi c^2}{2w_0^3} \frac{\Gamma}{\delta} I_0. \quad (4.31)$$

From equations 4.23 and 4.24, it can be seen that increasing the potential depth of a trap will result in an increase in the trap frequency. When comparing an optical lattice with a single beam dipole trap, the trap depth along the axis of beam propagation (axial), is deeper in the optical lattice, which results in a higher axial trap frequency for the optical lattice.

## CHAPTER 5

### SYMPATHETIC COOLING OF NANOSPHERES WITH ATOMS

Research on cooling the modes of vibration of mesoscopic objects to their ground state has flourished in recent years [12, 31, 37, 42, 113, 114, 115, 116]. Such research is important for testing the limits of quantum mechanics in macroscopic objects as it enables the study of decoherence in superpositions of macroscopic observables [117, 118]. These mechanical oscillators could be used as transducers in quantum networks [119, 120, 121], by providing coupling between photons, spins, and charges via phonons [50, 97, 98, 99, 100].

Recently, Jökel, et al [40] demonstrated sympathetic cooling of the vibrations of a nanomembrane by using cold atoms, coupled by laser light. They reported cooling the membrane from room temperature to  $650 \pm 230$  mK, and anticipate reaching the vibrational ground state by cryogenically pre-cooling the membrane to 4 K. Pre-cooling the membrane would reduce the thermalization rate, which represents the balance between coherent and dissipative dynamics, given by [122]

$$\Gamma_{th} = \frac{k_B T}{\hbar Q}, \quad (5.1)$$

where  $Q$  is the mechanical factor of the oscillator,  $k_B$  is the Boltzmann constant, and  $T$  is the initial temperature of the oscillator. It can be seen from equation 5.1, that increasing the mechanical quality factor of the oscillator would also be beneficial, this can be achieved by reducing the coupling of the oscillator to the environment. Because levitated mechanical systems do not have a clamping mechanism, they are highly decoupled from the environment [123] and their quality factors are predicted to reach  $> 10^{12}$  [124], limited by background gas collisions. Experimentally, these high mechanical quality factors have not been seen yet, but quality factors of  $10^7$

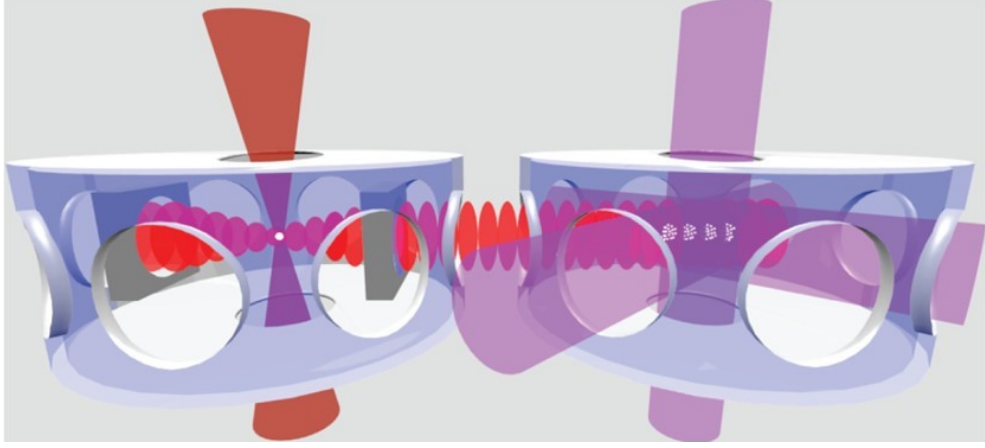


Figure 5.1: (Figure reproduced from ref. [2].) Experimental setup. The vacuum chamber on the left contains an optical cavity where a nanosphere is trapped using an optical tweezer. On the vacuum chamber on the right, atoms are trapped in an optical lattice which runs across both vacuum chambers providing the coupling between the two systems. The atoms are cooled through molasses cooling which sympathetically cools the center of mass motion of the levitated sphere.

at a pressure of  $10^{-5}$  mbar have been reported for levitated 70 nm radius particles [125], and recently a quality factor of  $10^{11}$  was reported at room temperature at a few millibars of pressure for a levitated nanorod [126]. This in comparison with the membrane in [40], which had a mechanical quality factor of  $10^4$ .

### 5.1 Proposed/Ongoing Experiment

A sample of  $^{87}\text{Rb}$  atoms are trapped in a one-dimensional optical lattice formed by a laser with a wavelength of about 780.74 nm, which is retro-reflected on the back mirror of a medium-finesse concentric optical cavity located in a separate vacuum chamber. A second laser of wavelength 1596 nm propagating perpendicular to the cavity axis is tightly focused, creating an optical tweezer inside the cavity. The optical tweezer is used to trap a silica sphere with a diameter of 170 nm, positioned at a node of the optical lattice (figure 5.2).



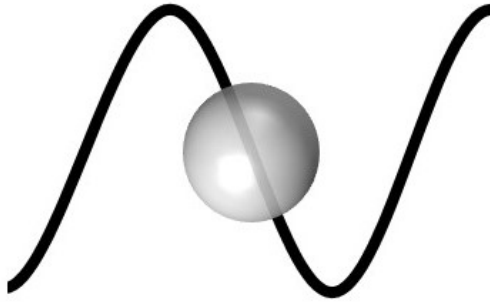


Figure 5.2: Representation of a nanosphere positioned in a node of an optical lattice. The black curve represents the intensity profile of the optical lattice.

### 5.1.1 Atoms-Bead Coupling

The two systems are coupled through the optical lattice, and the coupling is enhanced by the optical cavity. While the atoms are optically trapped by the one-dimensional lattice; the sphere is levitated by a 1596 nm wavelength optical tweezer, and the lattice only exerts a force on it along the cavity axis.

#### Force Imparted by the Atoms on the Sphere

The atoms absorb and re-emit photons incident from both directions of the optical lattice. As the atoms move away from their trap minima, they will absorb more photons traveling in the direction that restores them to their equilibrium position. This causes the intensity of the light striking the sphere to change accordingly, which means the force imparted on the sphere from the lattice is modulated as the atoms move about their equilibrium position [127].

## Force Imparted by the Sphere on the Atoms

The sphere is positioned at the location of maximal slope of the intensity of the standing wave. The sphere is small in comparison to the wavelength of the optical lattice: while the sphere's diameter is 170 nm, the lattice wavelength is about 780 nm. As a result, the phase of the light reflecting from the cavity, depends on the position of the sphere within the standing wave; for example, if the sphere was at a "dark region" of the lattice, where the two beams are destructively interfering, the phase of the outgoing light would not be shifted. This sphere-position dependent phase shift means when the sphere moves, the lattice gets shifted, changing the atom's trap minima position.

## 5.2 Coupling to the Lattice

The atoms and the sphere are coupled via a standing wave of frequency  $\omega_L$ . The coupling of each system to the lattice must first be studied to determine the coupling between the two systems. The momentum transfer of photons between the optical lattice and the atoms, and between the optical lattice and the sphere provides the coupling mechanism [39].

### 5.2.1 Atom-Light Coupling

The Hamiltonian that describes the laser field interaction with the dipole moment of the atoms is derived in detail by Vogell, et al in ref. [122]. In this paper, the atoms are modeled as a two-level system, and the atom-laser interaction is modeled

as an AC Stark shift for the atoms in the ground state. The atoms are trapped by an optical lattice of frequency  $\omega_L$ , far detuned from the transition frequency. The Hamiltonian describing the atom-light interaction, in a frame rotating at the laser frequency is given by [122]

$$H_{a-l} = \hbar G_{at} \int \frac{d\omega}{\sqrt{2\pi}} (b_w + b_w^\dagger)(a_{at} + a_{at}^\dagger) \sin[\Delta_w \bar{z}/c + \Delta\varphi_w], \quad (5.2)$$

where  $b_w$  and  $b_w^\dagger$  are the field mode operators,  $a_{at}$  and  $a_{at}^\dagger$  are the atom center-of-mass mode operators,  $\Delta\varphi$  is the phase by which the standing wave is shifted,  $\varphi_w$  is the center-of-mass position, and  $\Delta_w = \omega - \omega_L$ ,  $G_{at}$  is the atom-light coupling strength, given by

$$G_{at} = \frac{\omega_{at}}{2\alpha k_L \ell_{at}} \sqrt{\pi N_{at}}, \quad (5.3)$$

where  $\omega_{at}$  is the atom trapping frequency given by equations 4.29 and 4.30,  $N_{at}$  is the number of atoms,  $k_L = \omega_L/c$  is the wavenumber of the lattice laser, and  $\ell_{at}$  is the harmonic oscillator length for the atoms given by

$$\ell_{at} = \sqrt{\frac{\hbar}{2\omega_{at} m_{at}}}, \quad (5.4)$$

where  $m_{at}$  is the mass of the atoms. On equation 5.3,  $\alpha$  is a parameter related to the optical lattice power  $P$  by

$$P = \hbar \omega_L \frac{\alpha^2}{2\pi}. \quad (5.5)$$

From equation 5.3 it can be seen that the more atoms are trapped in the optical lattice, the better the coupling of the atoms to the lattice.

### 5.2.2 Sphere-Light Coupling

The sphere is levitated inside an optical cavity which enhances the coupling. Therefore, the coupling of the sphere to the optical lattice depends on the characteristics

of the cavity: the cavity mode volume  $V_c$ , and  $\kappa$  defined as half the cavity linewidth [128]

$$\kappa = \frac{\pi c}{L\mathcal{F}}, \quad (5.6)$$

where  $L$  is the length of the cavity, and  $\mathcal{F}$  is the cavity finesse, defined as

$$\mathcal{F} = \frac{c}{2L} = \frac{\Delta\omega}{\delta\omega}, \quad (5.7)$$

where  $\Delta\omega$  is the free spectral range of the cavity, and  $\delta\omega$  is the mechanical linewidth.

The cavity volume is defined as

$$V_c = \frac{\pi}{4}Lw^2, \quad (5.8)$$

where  $w$  is the cavity mode waist.

The coupling between the optical lattice and the sphere is given by [122]

$$G_s = \frac{3V}{2V_c} \frac{\epsilon - 1}{\epsilon + 2} \omega_L k_L \ell_s \frac{\alpha}{\kappa\sqrt{\pi}}, \quad (5.9)$$

where  $V$  is the volume of the sphere,  $\epsilon$  is the dielectric constant of the sphere,  $\ell_s = \sqrt{\hbar/(2\omega_s m_s)}$  is the harmonic oscillator length of the sphere which depends on the sphere trap frequency,  $\omega_s$ , given by equations 4.23 and 4.24, and the mass of the sphere  $m_s$ . The effective optomechanical coupling rate between the sphere and the atoms is given by

$$g = 2G_{at}G_s = \frac{3V}{2V_c} \left( \frac{\epsilon - 1}{\epsilon + 2} \right) \frac{\omega_L \omega_{at}}{\kappa} \sqrt{\frac{N_{at} m_{at} \omega_{at}}{m_s \omega_s}}. \quad (5.10)$$

### 5.3 Cooling Terms

In the adiabatic limit, where the atom-cooling rate exceeds the atom-sphere coupling rate, the sympathetic cooling rate is given by [40]

$$\Gamma_{cool} = \gamma_{at}^{cool} \frac{g^2}{\Delta^2 + (\gamma_{at}^{cool}/2)^2}, \quad (5.11)$$

where  $\gamma_{at}^{cool}$  is the atomic-cooling rate which in our case is set by the molasses beams.  $\Delta = \omega_s - \omega_{at}$  is the difference between the bead trap frequency and the atom trap frequency. For optimal sympathetic cooling, the mechanical trap frequency of the two systems must therefore match.

## 5.4 Heating Terms

The scattering of trap photons by the atoms and by the sphere leads to heating. This causes fluctuations in the radiation force due the randomness of the scattering [129].

### 5.4.1 Momentum Diffusion of the Atoms

The scattering of the lattice beams by the atoms lead to the following heating term

$$\gamma_{at}^{diff} = (k_L \ell_{at})^2 \gamma_{se} \frac{U}{\hbar \delta}, \quad (5.12)$$

where  $\gamma_{se}$  is the spontaneous emission decay rate of the atom, U is the lattice potential depth given by equation 4.31, and  $\delta$  is the lattice laser detuning from the Rb F=2 hyperfine component of the ground state [129].

### 5.4.2 Momentum Diffusion of the Sphere

The sphere will scatter light from both the lattice beam, and the trap beam. The Rayleigh scattering rate is given by

$$R_{sc} = \frac{24\pi^3 I U^2}{\lambda^4} \frac{1}{\hbar \omega} \left( \frac{\epsilon - 1}{\epsilon + 2} \right)^2, \quad (5.13)$$

where  $I$  is the intensity,  $\lambda$  the wavelength, and  $\omega$  the frequency of the laser beam; and  $U$  is the trap potential depth.

The heating rate due to Rayleigh scattering is given by

$$\gamma_s^{sc} = \frac{2}{5} \left( \frac{\omega_{rec}^{trap}}{\omega_s} \right) R_{sc}^{trap} + \frac{2}{5} \left( \frac{\omega_{rec}^{lat}}{\omega_s} \right) R_{sc}^{lat}, \quad (5.14)$$

where  $\omega_{rec}$  is the recoil frequency for the sphere

$$\omega_{rec} = \frac{\hbar k^2}{2m_s}, \quad (5.15)$$

where  $k$  is the wavenumber of the laser, and  $m_s$  the mass of the sphere.  $\omega_{rec}^{trap}$  is the tweezer recoil frequency, while  $\omega_{rec}^{lat}$  is the lattice recoil frequency.

An other source of heating of the sphere comes from radiation pressure

$$\gamma_s^{diff} = 2G_s^2, \quad (5.16)$$

where  $G_s$  is the lattice-sphere coupling, defined by equation 5.9.

The sphere is coupled to its environment through collisions with background gas, which occurs at a rate given by

$$\gamma_g = \frac{16P}{\pi \bar{v} \rho a}, \quad (5.17)$$

where  $P$  is the gas pressure,  $\bar{v}$  is the gas mean speed,  $\rho$  is the sphere's density, and  $a$  the sphere's radius. The role of the gas pressure surrounding the sphere is seen on this equation, as lower pressures will yield a weaker coupling to the environment.

The initial temperature bath  $T$  determines the mean thermal occupation number of the sphere  $\bar{n}_s$ , which represents the time-averaged thermal phonons of a given mechanical mode [25]

$$\bar{n}_s = \frac{k_B T}{\hbar \omega_s}. \quad (5.18)$$

From equations 5.17 and 5.18 we can define the thermal dissipation rate as

$$\Gamma_{th} = \gamma_g \bar{n}_s. \quad (5.19)$$

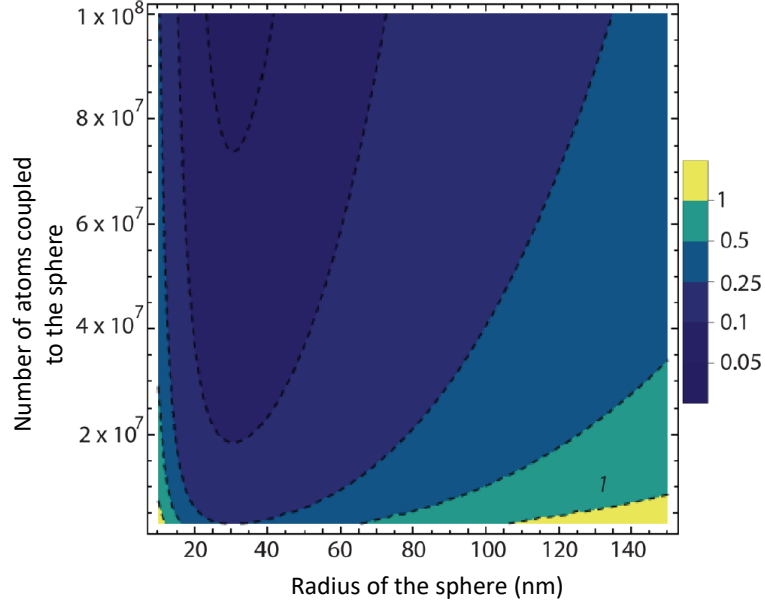


Figure 5.3: (Figure reproduced from ref.[2].) Steady-state phonon number of the sphere assuming a cavity finesse of 400. Higher number of atoms coupled to the sphere reduce the phonon number as it improves the coupling.

## 5.5 Steady State

Following [39], the steady-state phonon number of the sphere is given by the ratio of the heating rates to the effective cooling rates for both the atoms and the sphere

$$n_{ss} = \frac{\Gamma_{th} + \gamma_s^{diff}/2 + \gamma_s^{sc}}{\gamma_g + \Gamma_{cool}} + \left( \frac{\gamma_{at}^{cool}}{4\omega_{at}} \right)^2 + \frac{\gamma_{at}^{diff}}{2\gamma_{at}^{cool}}. \quad (5.20)$$

Figure 5.3 shows the steady state phonon number of the sphere for the values listed on table 5.1. It can be seen that for spheres with a radius smaller than 100 nm, single phonon level can be achieved if a minimum of  $10^7$  atoms are coupled to the sphere with a thermal bath at room temperature.

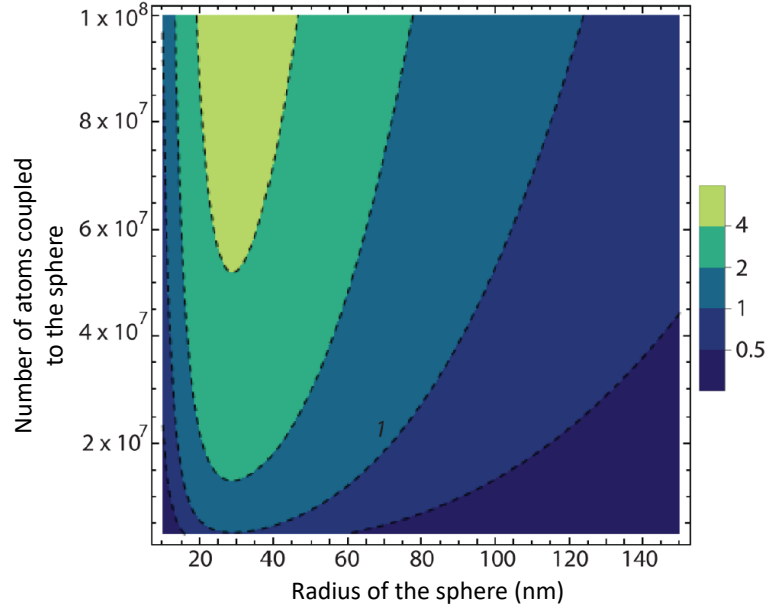


Figure 5.4: (Figure reproduced from ref. [2].) Ratio of coupling strength to the sum of the dissipation terms. Strong coupling dynamics are observed when the ratio is above 1.

### Strong Coupling Regime

When the effective coupling of the sphere and the atoms (equation 5.10) is larger than the dissipative effects, i.e. the coherent effects dominate the decoherent effects, normal mode splitting can be observed [130], evidence of reaching the strong coupling regime [131]. This regime is a state of reversible exchange of energy between the systems [132], a requirement for controlled quantum experiments of massive mechanical oscillators, as well as for using mechanical oscillators as quantum transducers for quantum information processing [131]. In our system, the strong coupling regime can be achieved by turning off the atom cooling and observing the evolution of the sphere by probing it with a weakly coupled laser to read its position in the cavity.



As previously mentioned, the strong coupling dynamics are observed when

$$\frac{g}{\gamma_{at}^{diff} + \gamma_s^{diff} + \Gamma_{th} + \Gamma_{sc}} > 1 \quad (5.21)$$

As can be seen from equation 5.10, the effective optomechanical coupling rate depends on the characteristics of the trapped sphere which sets the conditions for observing the strong coupling dynamics. Figure 5.4 illustrates the dependence of the number of trapped atoms and the sphere size in reaching the strong coupling regime for a given cavity mode volume.

Parameter	Symbol	Value	Units
Lattice wavelength	$\lambda_L$	780.74	nm
Lattice power	$P_L$	62	$\mu W$
Lattice waist	$w_L$	30	$\mu m$
Tweezer beam wavelength	$\lambda_t$	1550	nm
Tweezer beam power	$P_t$	460	mW
Tweezer beam waist	$w_0$	2	$\mu m$
Cavity length	L	5	cm
Cavity finesse	$\mathcal{F}$	400	-
Cavity mode waist	w	2	$\mu m$
Sphere's dielectric constant	$\epsilon$	2	-
Density of the sphere	$\rho$	2300	$kg/m^3$
Mass of Rb atom	$m_{at}$	$1.44 \times 10^{-25}$	kg
Spontaneous decay rate of Rb	$\Gamma_{at}$	$38.11 \times 10^6$	$s^{-1}$
Saturation intensity	$I_{sat}$	1.7	$mW/cm^2$
Pressure	P	$10^{-10}$	torr

Table 5.1: Parameters for sympathetic cooling of sphere.

## 5.6 Advantages of Sympathetic Cooling

Ground state cooling of levitated spheres might also be done via cavity cooling in the resolved sideband regime [113] (where the mechanical oscillator frequency is much larger than the cavity decay rate [39]). Cavity cooling requires a very high-finesse

cavity and a high mechanical oscillator frequency, both of which are difficult to obtain for levitated spheres [2]: heating from optical absorption limits the mechanical frequency of the spheres at high vacuum [133], and deposition of nanospheres onto the cavity mirrors degrades the cavity finesse [2]. Optical feedback cooling can also be used to reach the ground state, even in the bad cavity limit, if the position measurement of the sphere is done very precisely. This is not a requirement for sympathetic cooling, giving this method an advantage when position readout is not practical [2]. A combined approach (when possible) of feedback cooling and sympathetic cooling has been calculated to outperform each individual method [134].

## 5.7 Projected Results

Parameter	Symbol	a=150 nm sphere	a=50 nm sphere
Optomechanical coupling rate	$g$	$2\pi(5.9 \times 10^3 Hz)$	$2\pi(1.1 \times 10^3 Hz)$
Atom cooling rate	$\gamma_{at}^{cool}$	$2\pi(6.5 \times 10^3 Hz)$	$2\pi(1.2 \times 10^3 Hz)$
Momentum diffusion rate of the sphere	$\gamma_s^{diff}$	$2\pi(4.5 \times 10^3 Hz)$	$2\pi(1.7 \times 10^2 Hz)$
Scattering diffusion rate of the sphere	$\gamma_s^{sc}$	$2\pi(6.6 \times 10^3 Hz)$	$2\pi(2.4 \times 10^2 Hz)$
Momentum diffusion rate of the atoms	$\gamma_{at}^{diff}$	$2\pi(0.27 Hz)$	$2\pi(0.27 Hz)$
Trap frequency	$\omega_{at}, \omega_s$	$2\pi(4.5 \times 10^4 Hz)$	$2\pi(4.5 \times 10^4 Hz)$
Sympathetic cooling rate	$\Gamma_{cool}$	$2\pi(2.1 \times 10^4 Hz)$	$2\pi(4.1 \times 10^3 Hz)$
Thermal dissipation rate	$\Gamma_{th}$	$2\pi(9 Hz)$	$2\pi(28 Hz)$
Background gas collision rate	$\gamma_g$	$2\pi(6.6 \times 10^{-8} Hz)$	$2\pi(1.9 \times 10^{-7} Hz)$
Steady state phonon number	$n_{ss}$	0.41	0.09

Table 5.2: Derived parameters for sympathetic cooling of sphere.

Using the experimentally viable parameters listed on table 5.1, we have calculated the parameters on table 5.2 for a sphere of radius 50 nm and 150 nm. The results suggest it is possible to cool the center of mass motion of the sphere to the ground

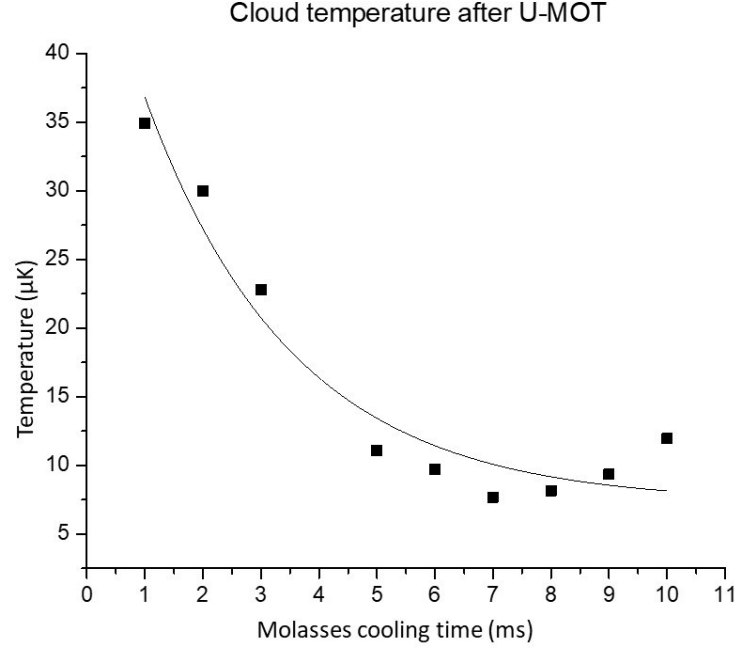


Figure 5.5: U-MOT temperature measured after various molasses cooling times.

state starting with a thermal bath at room temperature using a medium finesse cavity at a pressure of  $10^{-10}$  Torr.

The molasses cooling rate was calculated by studying the temperature of the U-MOT cloud after turning the molasses beams on for a variable time, as illustrated in figure 5.5, the cloud's temperature decreases exponentially with time. An exponential fit to this data yields the following function

$$T = 7.27 + 43.7e^{-0.39t} \quad (5.22)$$

where  $T$  is the cloud temperature in  $\mu\text{K}$ , and  $t$  is the time the molasses cooling was on for, in units of ms. By taking the inverse of the exponential term, we conclude that the cooling rate is 2.5 kHz. If we update table 5.1 with the experimentally measured parameters from our setup, listed on table 5.3 we can expect, as listed on table 5.4, a phonon number of 146, this corresponds to a temperature of 7.2 mK, as

calculated using equation 5.18. Although our current setup will not cool the sphere to the ground state, a significant reduction in the sphere's center of mass motion can be achieved, enough to proof the viability of such a setup.

Parameter	Symbol	Value	Units
Lattice wavelength	$\lambda_L$	781.3	nm
Lattice power	$P_L$	200	$mW$
Lattice waist	$w_L$	50	$\mu m$
Tweezer beam wavelength	$\lambda_t$	1596	nm
Tweezer beam power	$P_t$	250	mW
Tweezer beam waist	$w_0$	1.7	$\mu m$
Bead radius	a	85	nm
Number of atoms in lattice	$N_{at}$	$10^4$	
Atom cooling rate	$\gamma_{at}^{cool}$	2.5	kHz

Table 5.3: Experimentally measured parameters for current sympathetic cooling setup.

Parameter	Symbol	Value
Optomechanical coupling	g	$2\pi(201Hz)$
Momentum diffusion rate of the sphere	$\gamma_s^{diff}$	$2\pi(7.0 \times 10^3 Hz)$
Scattering diffusion rate of the sphere	$\gamma_s^{sc}$	$2\pi(6.0 \times 10^3 Hz)$
Momentum diffusion rate of the atoms	$\gamma_{at}^{diff}$	$2\pi(3.0 Hz)$
Trap frequency	$\omega_{at}, \omega_s$	$2\pi(1.6 \times 10^6 Hz)$
Sympathetic cooling rate	$\Gamma_{cool}$	$2\pi(65 Hz)$
Thermal dissipation rate	$\Gamma_{th}$	$2\pi(0.7 Hz)$
Background gas collision rate	$\gamma_g$	$2\pi(1.2 \times 10^{-7} Hz)$
Cavity linewidth	$\kappa$	$2\pi(7.5 \times 10^6 Hz)$
Steady state phonon number	$n_{ss}$	146

Table 5.4: Derived parameters with measured values on current sympathetic cooling setup.

## CHAPTER 6

### SPHERE'S EXPERIMENTAL SETUP

The sympathetic cooling of beads with atoms experiment is divided into two parts: the cold atom part and the levitated bead part. The hardware for the cold atom portion has already been built as it is the same setup used in the cold atoms coupled to a cantilever experiment. The bead portion of the experiment has all been designed and built in house.

#### 6.1 Trapped Atoms in an Optical Lattice

For this experiment, the atoms will not be magnetically trapped but optically trapped in a one-dimensional optical lattice. To create this optical lattice, we use a home-built 780 nm external-cavity diode-laser. An anti-reflection coated Fabry-Perot laser, tunable from 770 nm to 790 nm, was used for this purpose (Eagleyard photonics: EYP-RWE-0790-04000-0750-SOT01-0000). Construction was done following the design discussed by Cook, et al [135] which is freely available and thoroughly documented online at <http://atomoptics-nas.uoregon.edu/unilaser/>. This laser is seeded into a homebuilt optical amplifier constructed using a design provided by Dr. David Weld with a commercial tapered amplifier chip (Eagleyard: EYP-TPA-0780-01000-3006-CMT03-0000).

##### 6.1.1 Optical Layout

As seen on figure 6.1, a 780 nm homebuilt laser with an output power of about 15 mW is ran through an optical isolator to prevent back-reflections. The beam is split into

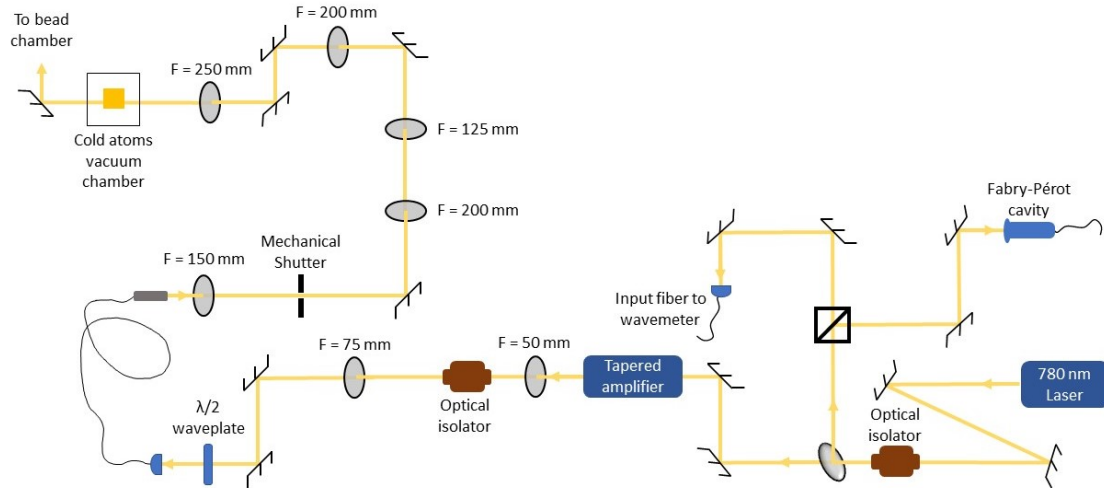


Figure 6.1: Optical layout of lattice beam. A 780 nm laser seeds a tapered amplifier which is coupled into a fiber to optimize the beam profile on its output. The beam is then resized before being tightly focused.

two by a beam sampler; while most of the power continues straight through the beam sampler, a portion of the beam is reflected and split again into 2 beams by a 50/50 beam splitter cube. The beam that gets reflected is coupled into a Fabry-Pérot cavity (Thorlabs: SA200 -5B) which is used to lock the laser to a single mode of the laser. The beam that gets transmitted through the cube is coupled into an optical fiber which is connected to a wavemeter (Bristol instruments: 521), this allows monitoring of the homebuilt laser's frequency, which has been determined to remain stable. The beam that gets transmitted through the beam sampler is seeded into a homebuilt tapered amplifier which outputs about 700 mW. A cylindrical lens of focal length 50 mm is used to collimate one of the axis of the beam which is then ran through an optical isolator to prevent back-reflections into the amplifier. A second cylindrical lens of focal length 75 mm is then used to collimate the other axis of the beam. Before coupling the beam into an optical fiber, a  $\lambda/2$  waveplate is used to manipulate the polarization axis. The purpose of the optical fiber is to "clean" the beam profile as

the input beam is elongated on one of the axes. This affects the coupling into the fiber which is why only about 30 % of the input power is coupled into the optical fiber. On the output side of the fiber, the beam has a Gaussian profile which is desired when focusing the beam down to a tight waist. A 150 mm and a 200 mm lens magnify the beam by 1.3x. In between these lenses a mechanical shutter (Uniblitz electronics: LS3T2) controls the beam on or off. A second telescope magnifies the beam by 1.6 x. This telescope is made with lenses of focal length 125 mm and 200 mm. Finally, an aspheric lens of focal length 250 mm, focuses the beam into the vacuum chamber, parallel to the chip surface, where the waist is aligned with the center of the MOT. On the output side of the vacuum chamber, the beam is collimated and sent to the bead chamber.

### 6.1.2 Trapped Atoms Characterization

In the final experiment, the optical lattice will be produced by retro-reflecting the laser on the back mirror of an optical cavity in the bead chamber. Although the cavity has not been installed into the vacuum chamber yet, an optical lattice has been created by retro-reflecting the beam on a mirror located near the position where the cavity will be installed. Doing this has allowed characterization of the optical trap and of the cloud of trapped atoms. Figure 6.2 contains a front image of the atoms, taken using the method illustrated in fig. 3.11. As expected, the trap is long in one direction, corresponding to the axis along the laser propagation. Radially, we expect the trap to be narrow because of the strong radial gradient, this is seen on 6.3 which is a radial cross-section of the cloud. Plotting the trap profile from the images horizontally and vertically, and subsequently fitting a Gaussian function to the data, yields information on the width and the optical density along each axis, this data is

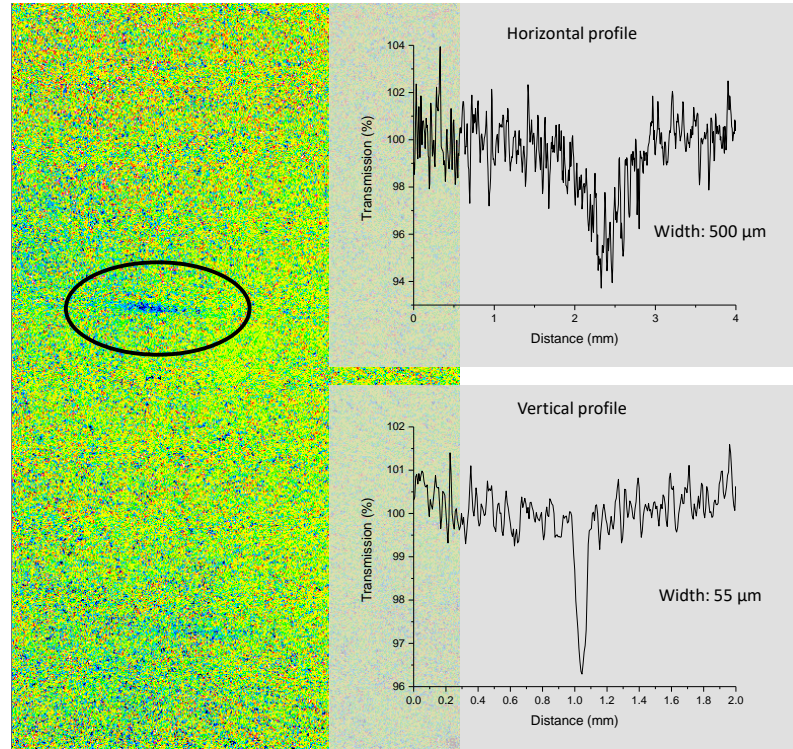


Figure 6.2: Front image of optical lattice. Top right: East-west profile of lattice. Bottom right: Vertical profile of lattice.

summarized on table 6.1. Using the equations on section 3.6.2 and the data on table 6.1, a density of  $10^9$  atoms/ $cm^3$ , and a total atom population of  $10^4$  atoms is obtained. Although  $10^4$  atoms is not enough to reach the ground state, improvements in the optical lattice trap depth, and initial MOT population and temperature can increase the total number of atoms trapped. Furthermore,  $10^4$  atoms is enough to observe some level of cooling of the sphere, this would provide proof of the functioning of this method of cooling.



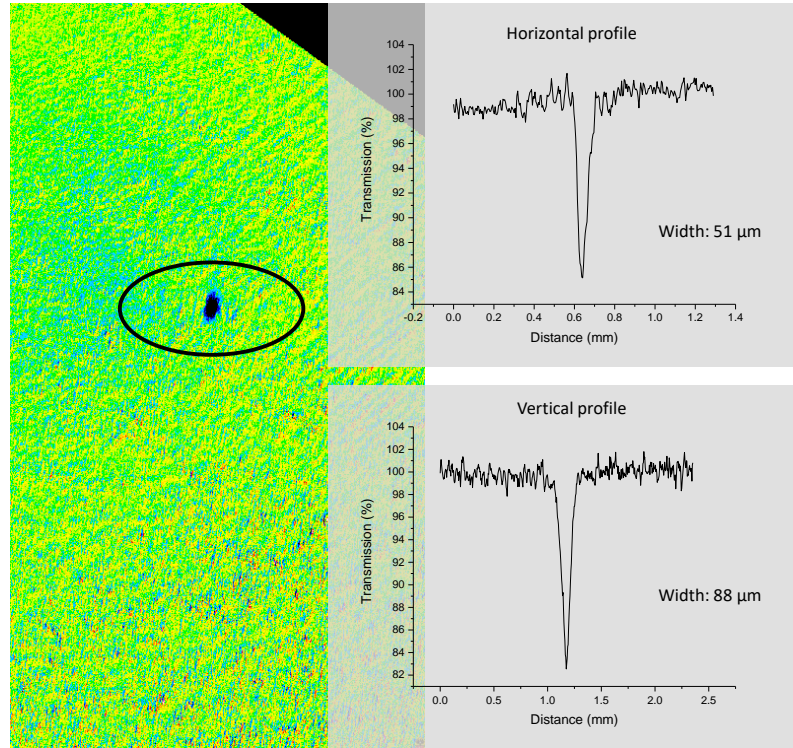


Figure 6.3: Side image of optical lattice. Top right: North-south profile of lattice. Bottom right: Vertical profile of lattice.

Axis	Optical Density	Cloud Width ( $\mu\text{m}$ )
East-West	0.157	500
North-South	0.025	51
Vertical	0.043	88

Table 6.1: Optical lattice atom trap characterization.

## 6.2 Vacuum Chamber

Custom design of a vacuum chamber for the levitated bead portion of the experiment was done by Apryl Witherspoon, an undergraduate student in our research group. As seen on figures 6.4 and 6.5, two large windows with anti-reflective coating provide optical access to the chamber, the top of the chamber also contains a window used for imaging with a CCD camera. The inside of the chamber holds a  $5'' \times 5''$  optical

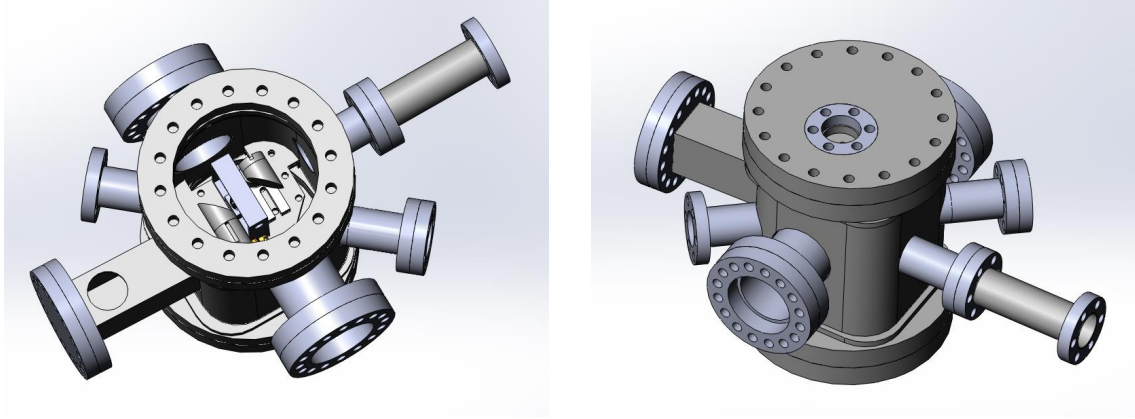


Figure 6.4: (Adapted from ref. [136].) Solid Works rendering of bead vacuum chamber. (Left) Top view of chamber. The lasers enter and exit the chamber through the two big windows on the top left and bottom right of the picture. The square tube on the left houses the diving board. (Right) Bottom view of chamber. A small window on the bottom provides optical access for imaging.

breadboard where the optical components are mounted.

### 6.2.1 V-Block

The dipole trap in which the beads are levitated is done by focusing a 1596 nm laser beam with a  $1/e^2$  radius of 3.4 mm by use of a aspheric lens with a numerical aperture of 0.5 and a focal length of 8 mm. An identical lens is used to collimate the outgoing beam. To maintain the height of the two lenses from the optical breadboard equal, a monolithic block of aluminum containing two 'v'-shaped channels was built to hold the two lenses (figure 6.6). The two lenses are mounted inside an aluminum cylinder. The lens holders are glued to the V-block with a vacuum compatible epoxy (Epo-TEK 353ND).

To finely tune the location of the trap waist, before striking the first lens, the beam

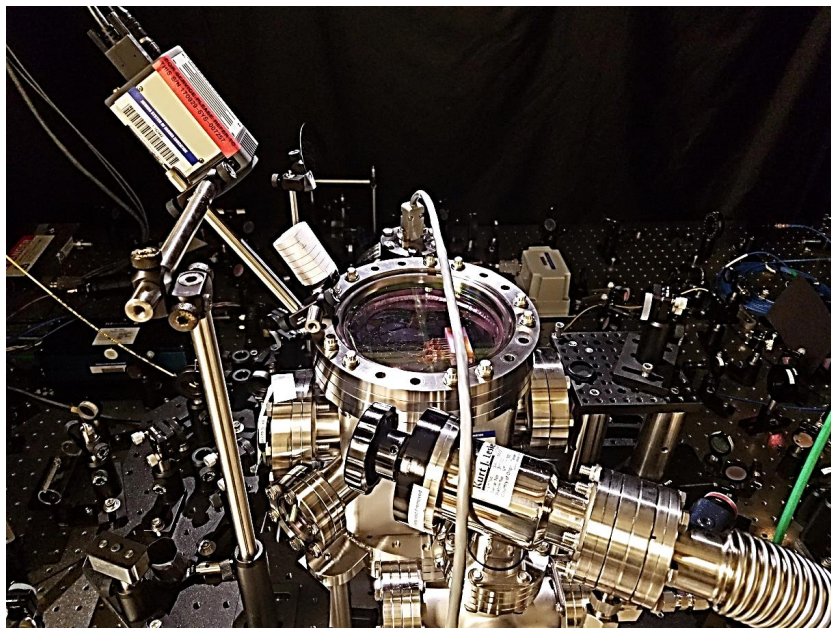


Figure 6.5: Bead vacuum chamber. A top window provides optical access to a CCD camera. Two side windows provide optical access for the lasers in the experiment.

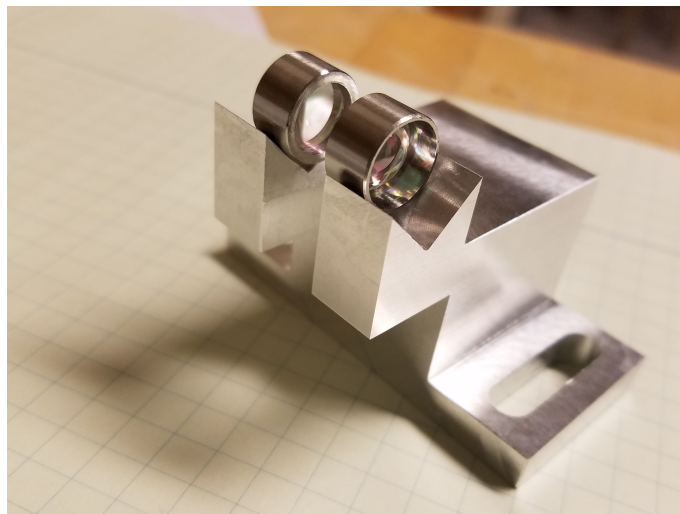


Figure 6.6: V-block holder for the trap lenses.

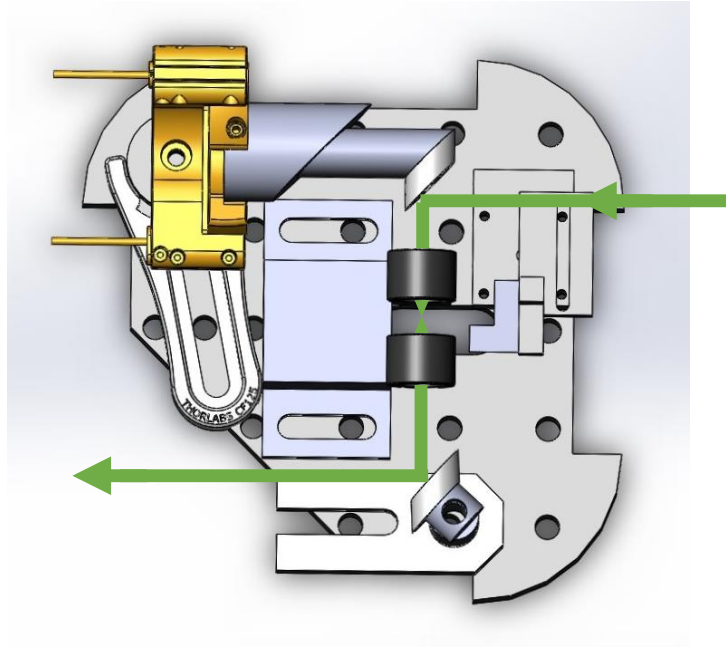


Figure 6.7: Optical layout inside bead chamber. A 1596 nm laser beam enters from the right and bounces on a piezo-controlled mirror before going through a focusing lens which creates the optical trap and a collimating lens. The beam exits the chamber through the left window by bouncing on a mirror.

is reflected on a mirror attached to a piezo-controlled mount (figure 6.7). Directly below the lenses, the optical breadboard has an opening providing optical access from a bottom window on the vacuum chamber.

### Beam Waist

Using equation 4.7, for a wavelength of 1596 nm, a focal length lens of 8 mm, and an input beam with diameter 3.4 mm, we calculate a diffraction limited waist of  $1.2 \mu\text{m}$ . To measure the actual waist, the sharp edge of a razor blade mounted on a micrometer stage was used to systematically block the laser near the focus. A power meter located after the collimating lens is used to record the laser power that is not being blocked by the razor blade. As observed on figure 6.8, performing a mathematical derivation

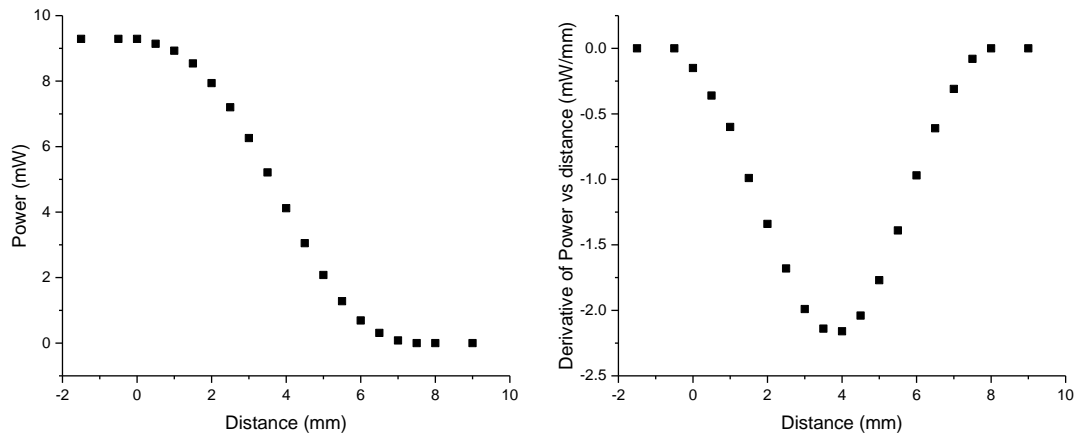


Figure 6.8: Beam width measurement done using a razor blade to systematically block the laser while monitoring the power.

of the laser power as a function of micrometer position yields a Gaussian curve that describes the laser's cross-section profile at the location where the razor blade was positioned. As seen on figure 6.9, recording the  $1/e^2$  radius ( $w(z)$  as defined by equation 4.4) of the beam's profile in a few locations before and after the focal spot allows the study of the beam's spot size evolution, which should match equation 4.4. From this data, the beam waist can be easily deducted. In our setup, the measured beam waist is  $1.4 \mu\text{m}$ , which is very close the diffraction limited waist of  $1.2 \mu\text{m}$ , calculated using equation 4.7.

### 6.2.2 Optical Cavity

Although it has not been installed yet, the optical cavity has been built from monolithic Invar, which is a nickel-iron alloy with a very low coefficient of thermal expansion, this is particularly useful in an optical cavity because its temperature doesn't need to be controlled to achieve high stability. Figure 6.10 shows the optical cav-

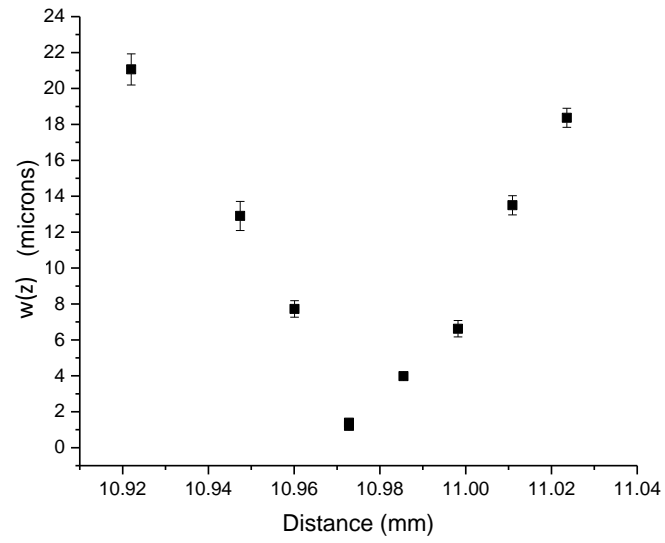


Figure 6.9: Beam width measurements near waist used to deduce a beam waist of  $1.4 \mu\text{m}$ .

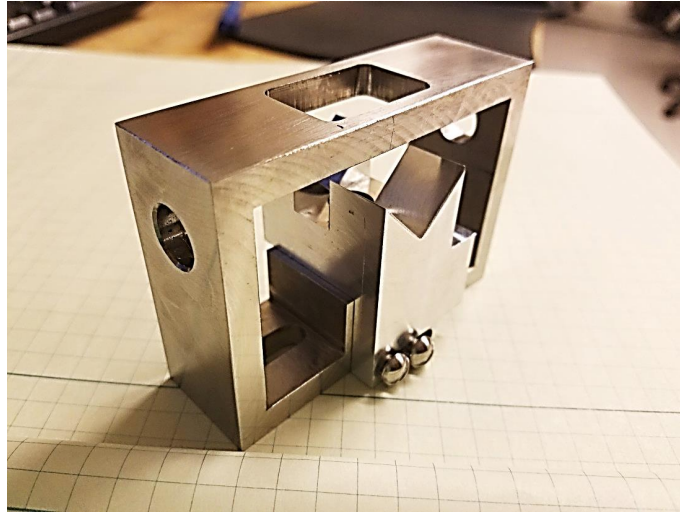


Figure 6.10: Invar optical cavity and V-block. The lenses on the V-block and the mirrors on each side of the cavity are not shown in the picture.

ity with the V-block integrated onto it. This design allows positioning the bead trap along the optical cavity's axis by sliding the V-block along the cavity. Horizontal variations in the bead's trap position perpendicularly to the cavity axis can be achieved by varying the collimation of the beam before striking the lens. Finally, small variations in the vertical plane along the cavity axis can be done by adjusting the input beam's angle with the piezo-controlled mirror.

### Cavity Dimensions

As can be seen on figure 6.11, the distance between the cavity walls before adding the mirrors is 66.50 mm. The thickness of the cavity mirrors is 6.35 mm, but because they are concave, the front face on the center of the mirror is receded 0.040 mm, so the net thickness at the center of the mirror is 6.31 mm. One of the mirrors is glued on a 2 mm thick piezoelectric transducer. Additionally, we must take into consideration the thickness of the epoxy used to attach the piezo to the cavity, the mirror to the piezo, and the second mirror to the cavity. Each layer of epoxy is about 25  $\mu\text{m}$  thick, for a total epoxy thickness of 75  $\mu\text{m}$ . Adding all these components, and subtracting from the distance between the cavity walls gives the cavity length

$$l_{\text{cavity}} = d_{\text{walls}} - (t_{\text{piezo}} + 2t_{\text{mirror}} + 3t_{\text{epoxy}}) \quad (6.1)$$

$$l_{\text{cavity}} = 51.81\text{mm}. \quad (6.2)$$

### Bead Chamber Optical Layout

Two laser beams will go through the cavity. To trap the beads, a 1596 nm beam crosses the cavity perpendicularly along the channels of the V-block on figure 6.10.



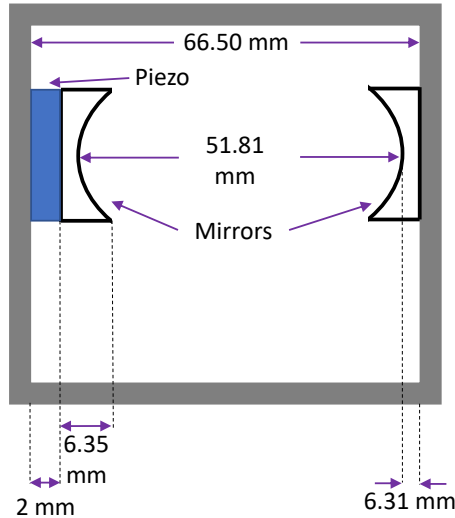


Figure 6.11: Optical cavity diagram. We assume a  $25\ \mu\text{m}$  layer of epoxy between the piezo and the cavity wall, as well as between the mirror and the piezo and between the second mirror and the cavity wall.

A 780 nm beam, coupled into the cavity, travels along the cavity axis and strikes the bead to provide the coupling between the bead and the atoms. The 780 nm beam gets retro-reflected by the back mirror of the cavity to produce the optical lattice in which the atoms are trapped in.

### 6.3 Bead Launching

To levitate a bead in our optical trap, the sphere first needs to be released into the vacuum chamber. Adhesion forces act on the spheres and keep the spheres attached to the substrate they are in. These adhesion forces are the Van der Waals force, the electrostatic force, and the capillary force [137]. All of these forces depend on the separation distance between the sphere and the substrate, and on the sphere diameter. The capillary force, the strongest of all 3 in our setup, can be reduced by heating the substrate and spheres, this causes the moisture to evaporate. The electrostatic



force is also not very relevant in our experiment as most of the beads have a neutral charge [138]. Therefore, the Van der Waals force is the predominant force keeping the spheres attached to the substrate.

### 6.3.1 Van der Waals Force

The Van der Waals force is a result of repulsive and attractive forces between atoms and molecules. For a sphere in proximity to a flat surface [137]:

$$F_{vdw} = \left( \frac{\delta}{\delta + r/2} \right)^2 \left( \frac{Hd}{16\pi\delta^2} + \frac{H\rho^2}{8\pi\delta^3} \right), \quad (6.3)$$

where  $\delta$  is the distance between the sphere and the surface,  $r$  is the roughness of the surface,  $H$  is the Lifshitz-Van der Waals constant,  $d$  is the sphere's diameter, and  $\rho$  is the radius of the adhesion surface area.

As can be seen from equation 6.3, there is a linear dependence on the radius of the sphere and the Van der Waals force. The acceleration required to remove the sphere from the surface it is adhered to is

$$a \propto \frac{a}{m_s}, \quad (6.4)$$

where  $m_s$  is the mass of the sphere.

$$a \propto \frac{a}{\frac{4}{3}\rho_s a^3} \propto \frac{1}{a^2}, \quad (6.5)$$

where  $\rho_s$  is the density of the sphere. Considering we use 170 nm spheres, we require an acceleration of approximately  $10^9 \text{ m/s}^2$  [139], much larger than the acceleration due to gravity, which explains why the spheres remain attached to the substrate.

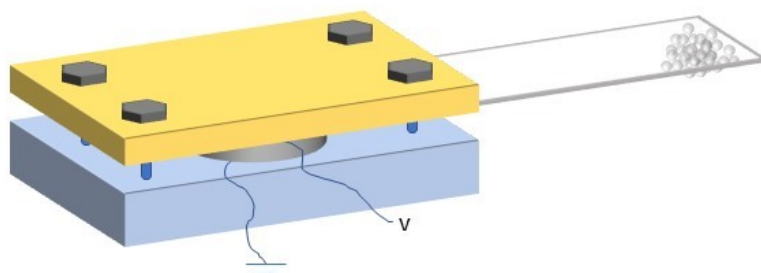


Figure 6.12: Diving board assembly diagram. A glass slide containing spheres on its tip is placed on top of a piezoelectric ring, both of which are clamped between two plates. As the piezoelectric material vibrates, the glass slide acts like a diving board providing enough acceleration to release the spheres.

### 6.3.2 Diving Board Launcher

#### Bead Preparation

In our setup, we use non-porous silica ( $SiO_2$ ) spheres with a diameter of 170 nm (Bangs Laboratories: SS02000). A glass slide is used to transfer the spheres from the aqueous solution in which they are purchased, to the chamber. A few drops of the bead-containing solution are placed on a glass slide which is then heated on a hot plate for 1 hour at 150 °C to evaporate the solution and turn it into a powder. A portion of the bead powder is then scraped using a tungsten probe tip onto a second slide which is heated on a hot plate for 20 minutes at 150 °C to eliminate moisture. To avoid ambient moisture from re-accumulating around the spheres, the slide must be re-baked if its not under vacuum within 15 minutes of its removal from the hot plate.

## Diving Board Assembly

The glass slide containing beads on its tip is placed on top of a piezoelectric transducer ring (APC international: 70-2221). This piezoelectric transducer is manufactured from PZT ceramic (Pb: lead, Zr: zirconium, Ti: titanium). The glass slide and the piezoelectric ring are both clamped between two plates. The bottom plate is electrically connected to the bottom side of the piezoelectric transducer which is connected to ground. The top plate is made of Techtron, a plastic with very low electrical conductivity. The insulating properties of Techtron prevent electrical arcing between the top plate and the grounded bottom plate [140]. The top side of the piezoelectric transducer is connected to a variable voltage which causes the material to expand and contract, this produces the tip of the glass slide to act as a diving board providing enough force to release the beads into the air. The piezoelectric ring has many ultrasonic vibrational modes, but greater accelerations can be achieved at higher frequencies [139]. Typically, in our setup we use the resonance frequency of 141 kHz.

## Diving Board Driver

To achieve the high power needed to drive the piezoelectric ring, a large current is required due to the low resonance impedance [139]. A high power pulse generator has been built for this purpose, using the design on figure 6.13. A function generator drives a power MOSFET which controls the high current pulses sent to the piezoelectric transducer.

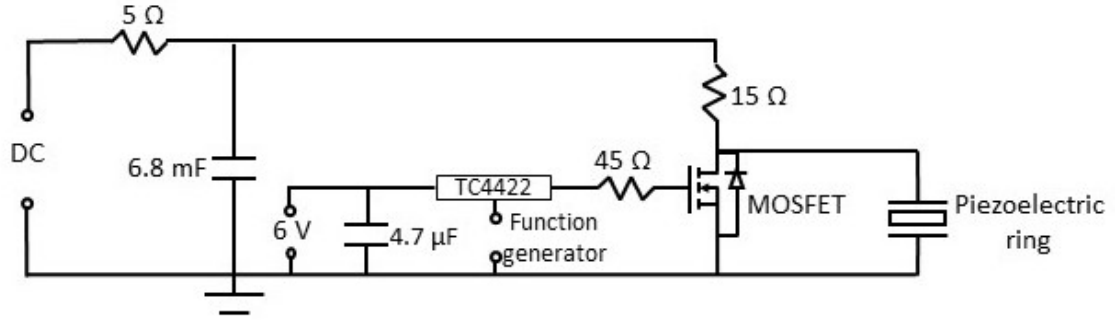


Figure 6.13: (Adapted from ref. [139].) Circuit diagram of diving board launcher driver. A function generator drives a MOSFET which controls high power pulses across the piezoelectric transducer.

### 6.3.3 Trapping of Beads

When the piezoelectric transducer is driven on resonance, the tip of the glass slide, which contains beads on the bottom side, oscillates like a diving board providing enough force to shake the beads off the glass slide. Each pulse is only done for a period of 0.3 to 1.5 s followed by a rest period of about 50 s. Once the beads are airborne, they will fall due to gravity. If the rest period is too short, a bead might get trapped but knocked out of the trap by other airborne spheres. The launching of beads is done at a pressure of about 7 Torr. At this pressure, there is enough air in the chamber to provide damping which will reduce the sphere's velocity, this makes it easier to catch beads. On the other hand, if the pressure is too high, air instabilities might knock beads out of the trap.

#### Bead Clumps

On every pulse, many beads are released to increase the chances of one bead falling at the trapping region. As can be seen on figure 6.14, the potential energy required

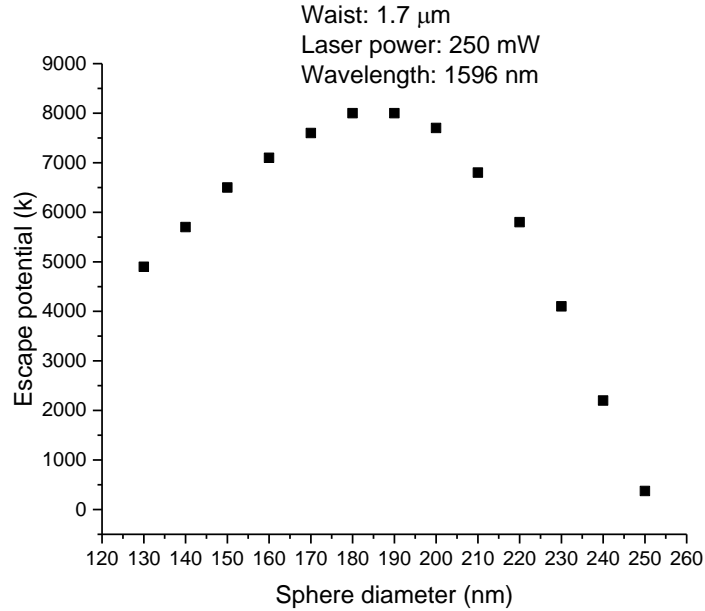


Figure 6.14: Trap escape potential on axial direction as a function of bead size for 1596 nm laser with a power of 250 mW and a waist of 1.7  $\mu\text{m}$ .

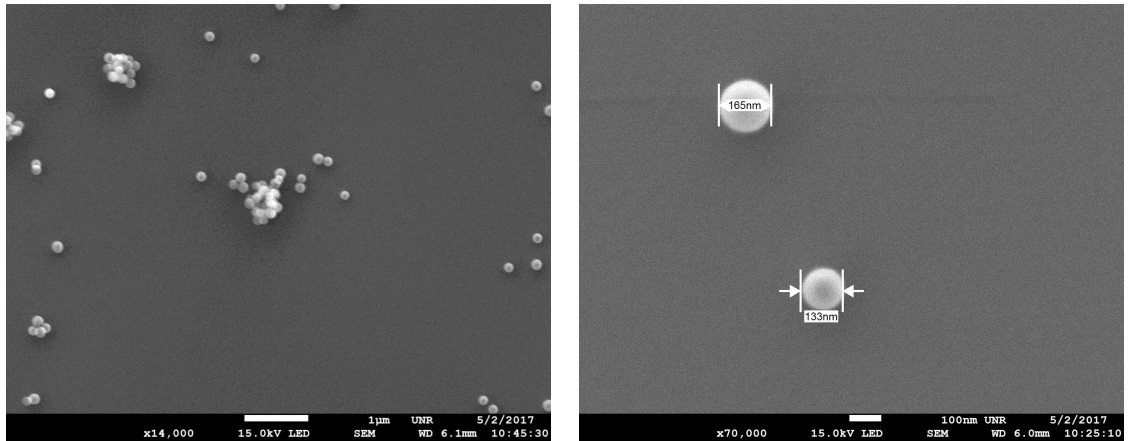


Figure 6.15: SEM images of launched spheres. (Left) Single spheres and clumps of spheres are launched with the diving board method. (Right) Two launched single spheres of slightly different sizes.

to escape the trap on the axial direction, sharply decreases for beads larger than 200 nm. This effect is a result of the scattering force increasing more rapidly than the gradient force as the former scales as  $a^6$ , while the latter as  $a^3$ , where  $a$  is the radius of the sphere. As the beads are released from the glass slide, they occasionally fall adhered to each other in groups, or clumps. Due to the fact that in our setup, big spheres can't be trapped, we don't need to worry about trapping these clumps of beads. However, if a majority of the launched beads are released in clumps, the flux of launched beads might look good, but none would be trapped. A solution to reduce clumps is spin coating the slide on a centrifuge, this produces a mono-layer of beads [140].

To determine whether clumps of spheres would be an issue, a microscope slide was placed directly under the diving board from which the beads are launched. After several pulses of the diving board, the slide was removed and taken to a scanning electron microscope (SEM) to study how frequently clumps are launched vs single spheres. Figure 6.15 shows two SEM images depicting launched beads. The image on the left shows both, single beads and clumps of beads, suggesting we do in fact launch singles and there is no need to spin coat the slides. The image on the right shows two different beads with diameters 165 nm and 133 nm. This variation in size is surprising as the sphere's manufacturer reports a 10% variation in diameter. Nevertheless, a 20% variation in size can be tolerated in our setup, since spheres 20% larger or smaller can still be trapped, as can be deducted from figure 6.14.

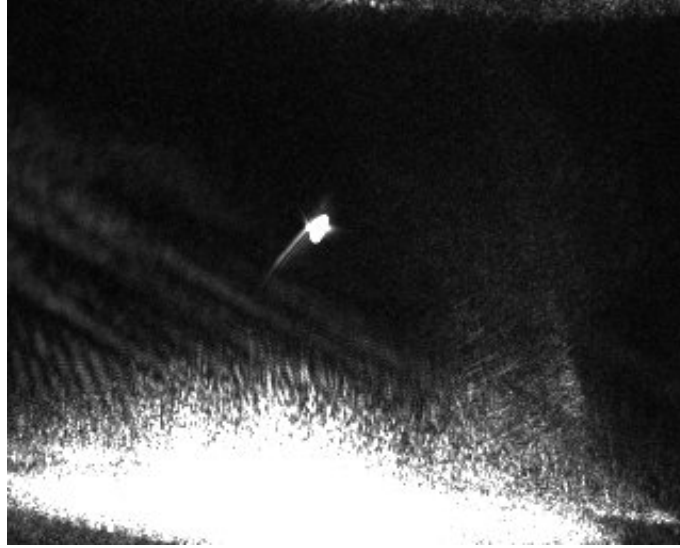


Figure 6.16: CCD image taken with an InGaAs camera of a 170 nm bead trapped at 7 Torr with a 1596 nm laser focused to a waist of  $1.7\ \mu\text{m}$ .

## 6.4 Bead Imaging

The trapped spheres are imaged in two different ways: using a camera to see the sphere live, and using photodetectors to study the motion of the sphere.

### 6.4.1 Live Imaging

#### InGaAs Camera

A CCD InGaAs camera (Hamamatsu: C14041-10U) is used to look at the trap live. This camera is highly sensitive to light with a wavelength from 950 nm to 1700 nm, with a pixel size of  $20\ \mu\text{m}$ . The camera is pointed at the trap, when the spheres pass through the laser, light is scattered from them, which can be seen on the CCD camera, because we use a 1596 nm laser to trap the spheres. Figure 6.16 shows a 170

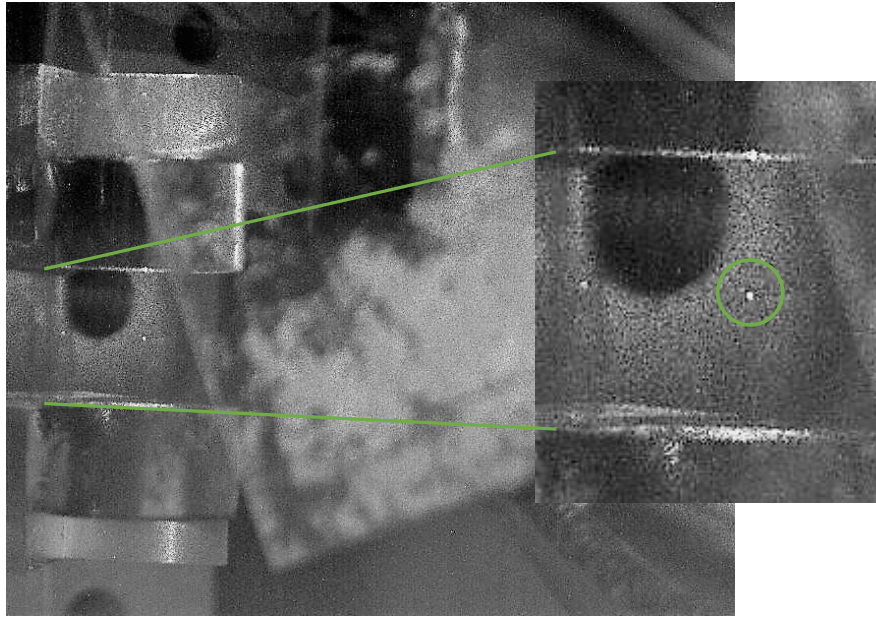


Figure 6.17: CCD image of trapped sphere, taken using Si camera sensitive to 632 nm light. On the left side of the picture the two lenses can be seen, in between them the trapped sphere. Near the center of the image, from the top to the bottom of the picture, the glass slide with beads on it is captured. (Inset) Zoomed in image of trapped 170 nm sphere.

nm trapped sphere, on this image, the laser enters from the top, the bright region on the bottom of the image is light scattered from the collimating lens. Having a live image of the trap when launching the spheres is used to gauge the flux of beads as the diving board is shaken. Typically when the flux is low, the slide needs to be changed. Also, this live image is used to determine when a bead gets caught in the trap. Although the trapping rate varies, with a power of 250 mW, and a fresh slide in the system, trapping occurs after only a few shakes of the diving board, usually within 10 minutes.



## Si Camera

Before using the InGaAs camera, live imaging was performed using a Si CCD camera (Chameleon: CMLN-13S2M). This camera is sensitive to light of wavelength 300 nm to 900 nm, therefore it is not sensitive to the scattered trap light. A HeNe laser (Melles Griot: 25-LHP-151) with a power of 5 mW and a wavelength of 632.8 nm was aligned collinear to the trapping 1596 nm laser with the purpose of imaging the light scattered from this laser, rather than from the trapping laser. Although, as seen on figure 6.17, we successfully imaged spheres using this method, we encountered two main issues: low laser power and difficulty aligning the two focal spots.

The HeNe laser only outputs 5 mW of power, so the image from the light scattered from the sphere isn't very bright on the camera. In fact, the brightness of the sphere was comparable with the intensity fluctuations of the pixels surrounding the sphere. To distinguish the sphere from surrounding fluctuations, several pictures were taken and averaged. This process was slow and inefficient. The second problem we encountered was the focal spots of both, the 1596 nm laser and the HeNe laser, must overlap to successfully image the trap. Chromatic aberrations made this task difficult: if both laser beams strike the trap lens collimated, the focal spots will occur at different distances from the lens. From table 6.2, it can be noted that the waist of the HeNe laser will occur about  $267\text{ }\mu\text{m}$  before the 1596 nm laser's waist. To push the focal spot further from the lens, the input beam collimation can be deliberately modified such that the beam is diverging. Although possible, in practice, getting the HeNe beam to focus 8 mm away from the lens is difficult, as a small change in the distance between the two resizing lenses that produce the diverging beam moves the focal spot by a significant amount.

Wavelength (nm)	Focal length (mm)
405	7.652
633	7.929
670	7.950
780	8.000
810	8.011
830	8.018
980	8.062
1064	8.083
1550	8.196

Table 6.2: Focal length of Thorlabs A240-C aspheric lens for various wavelengths [141].

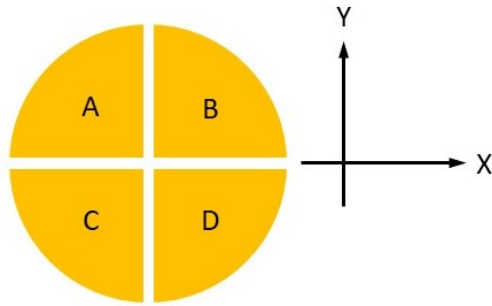


Figure 6.18: Segmented photodiode diagram. Light incident on each active area is processed individually, allowing measurement of beam displacement along the photodiode.

#### 6.4.2 Bead Spectra

After verifying that the bead is trapped, the spectra of the sphere is studied to determine its frequency. This is done by imaging the transmitted light or the scattered light onto a photodetector.

## Quadrant Photodetector

A photodiode is a device that converts light into an electrical current proportional to the intensity of the input beam. A photodiode in combination with an electronic circuit that turns the photocurrent into a voltage readable by an oscilloscope is called a photodetector [91]. A quadrant photodetector is composed by a segmented photodiode (figure 6.18) containing 4 active areas. The displacement of a beam relative to the center of these 4 areas is easily obtained in such a setup, this makes quadrant photodetectors ideal for applications regarding beam displacement, or displacement of a portion of a beam.

Each active area produces a voltage proportional to the intensity incident on it. To measure beam displacement along the X-axis on figure 6.18, the voltages from sections A and C must be added and subtracted from the addition of sections B and D. Similarly, to measure the displacement along the Y-axis, sections C and D are subtracted from sections A and B.

The quadrant photodetector used in our setup was homebuilt using a commercial InGaAs photodiode (Hamamatsu: G6849-01) with a peak sensitivity at 1550 nm. Figure 6.19 shows the circuit diagram used. The photocurrent from each section of the photodiode is amplified and converted into a voltage using a trans-impedance amplifier configuration. The amplified signal is then sent to a processing circuit with three outputs: a sum and 2 difference signals, corresponding to the horizontal and vertical axis of the photodiode.

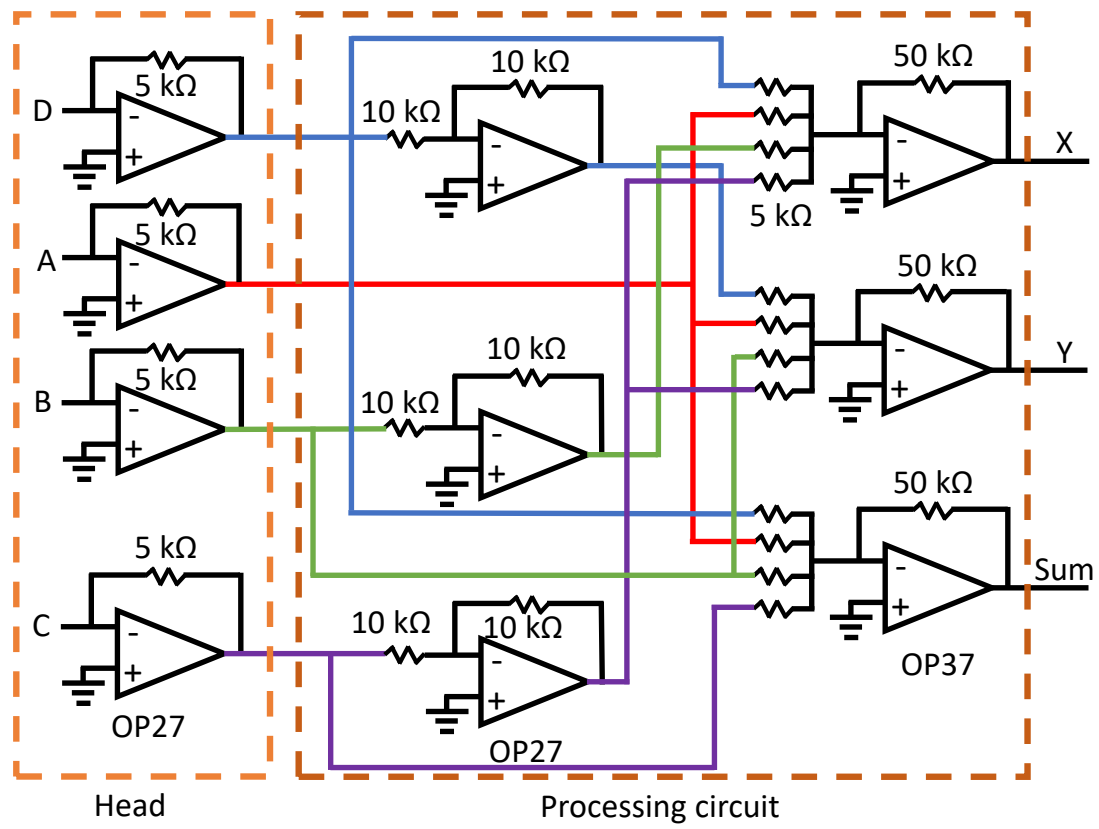


Figure 6.19: (Figure adjusted from ref. [91].) Diagram of quadrant photodetector circuit.

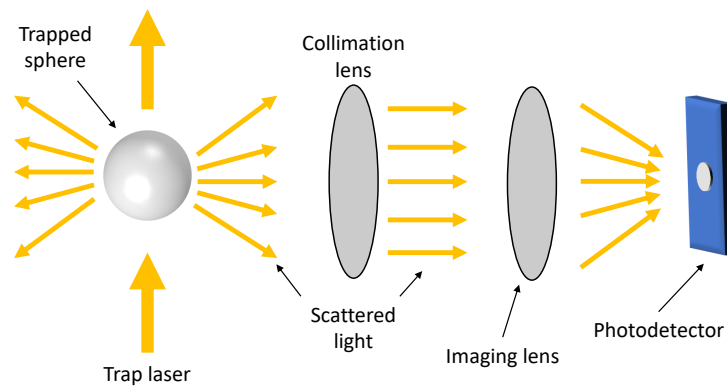


Figure 6.20: Imaging of light scattered by bead. A lens collects a portion of the scattered light and collimates it, to be sent to the photodetector.

## Imaging using Scattered Light

A trapped bead will scatter light in all directions, this scattered light contains information on the sphere's motion as it spatially varies with the sphere's movement. A lens with a focal length of 25 mm is placed 25 mm away from the trap site. This way, the scattered light that makes its way to the lens, exits the lens collimated. After collimating the scattered light, the beam is directed to a photodetector for processing. An issue with this method is that only a portion of the scattered light is collected, so the signal is very weak. Proper amplification of the signal must be done on the photodetector which limits the detectors bandwidth.

In our setup, the lens has a diameter of 12.5 mm, so its area is  $123 \text{ mm}^2$ . The lens is positioned 25 mm away from the trap site, so the lens only covers a small portion of the light sphere. The total light sphere area for a radius of 25 mm is  $7853 \text{ mm}^2$ , so the lens only collects about 1.5% of the scattered light. For the parameters on our setup we expect a total scattered power of about 4 mW. The total power on the lens would then be about  $60 \text{ }\mu\text{W}$ .

A quadrant photodetector is used to image the bead using the scattered light. To image the sphere onto the photodetector, a lens with a focal length of 150 mm is used. To achieve the sensitivity required, the transimpedance amplifiers on figure 6.19 were adjusted to have the desired gain by changing the resistors from 5 k $\Omega$  to 667 k $\Omega$ . At this gain, we have determined an output voltage to input laser power of  $7.5 \text{ V}/\mu\text{W}$ . As discussed on section 4.2.3, the expected bead frequency is 7 kHz and 32 kHz. To make sure the photodetector can sense these frequencies, an LED was flashed at various frequencies, while the output signal from the photodetector was monitored. A bandwidth of 190 kHz was measured, which is enough for our frequencies.

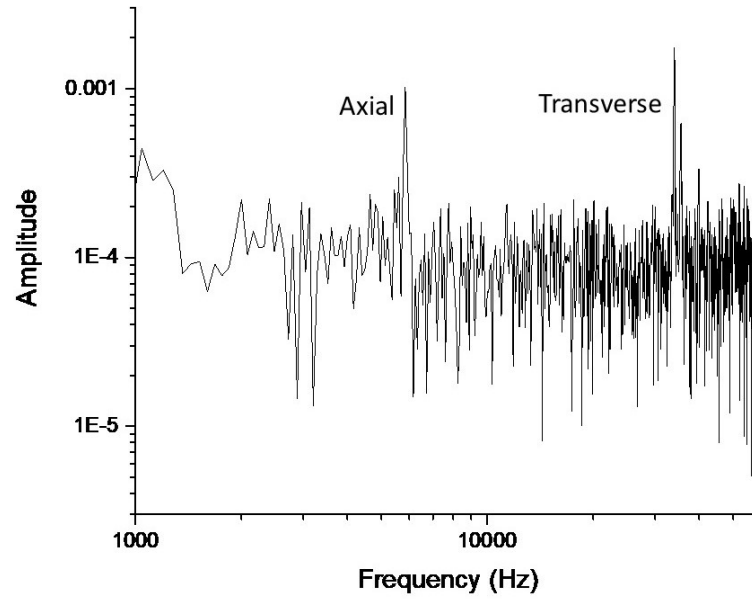


Figure 6.21: Bead spectra at a pressure of  $10^{-4}$  Torr. The data was obtained by imaging the light scattered by the trapped sphere onto a quadrant photodetector.

## Results

A Fast-Fourier Transform (FFT) of the signal from the light scattered by the sphere (figure 6.21) shows two frequency peaks corresponding to the axial and the transverse center of mass motions of the sphere. An axial frequency of 6 kHz, and a transverse frequency of 36 kHz were measured which agree with our expected values. Calculations of the mechanical quality factor could not be performed from this data because of insufficient data points due to a slow sampling rate. Future work includes measuring the mechanical quality factor as a function of the pressure in the vacuum chamber. It is expected that as the pressure decreases, the gas damping also decreases and therefore the quality factor increases. The damping coefficient can be calculated by experimental measurements of the trap frequency,  $\omega_0$ ; and the mechanical quality factor,  $Q$  with the following equation:  $\Gamma_0 = \omega_0/Q$ . Theoretically, the gas damping

coefficient is given by [142]

$$\Gamma_{gas} = \frac{6\pi\eta R}{m} \frac{0.619}{0.619 + K_n} (1 + c_k), \quad (6.6)$$

where  $\eta$  is the viscosity coefficient,  $R$  is the radius of the sphere,  $m$  is the mass of the sphere.  $c_k$  is given by

$$c_k = \frac{0.31K_n}{0.785 + 1.152K_n + K_n^2}. \quad (6.7)$$

$K_n$  is the Knudsen number defined as

$$K_n = \frac{l}{R}, \quad (6.8)$$

where  $l$  is the mean free path of the gas molecules.

## 6.5 Current State of the Experiment and Next Steps

At the time of writing this dissertation, 170 nm diameter spheres can be trapped in an optical tweezer created with a 1596 nm laser. The frequencies of the center of mass motion of the sphere can be monitored, and the pressure in the chamber can be decreased to  $10^{-5}$  Torr before losing the sphere. Next, the optical cavity must be installed in the vacuum chamber, and the 780 nm laser coupled to it. By coupling the 780 nm laser to the cavity, the beam is retro-reflected and the optical lattice is created. Pre-cooling of the sphere's motion is needed to maintain the sphere trapped at high vacuum pressures, this can be achieved using parametric feedback cooling.

### 6.5.1 Parametric Feedback Cooling

Parametric feedback cooling is a mechanism that allows cooling of the center of mass motion of a sphere in a dipole trap using a single laser beam. This cooling is achieved

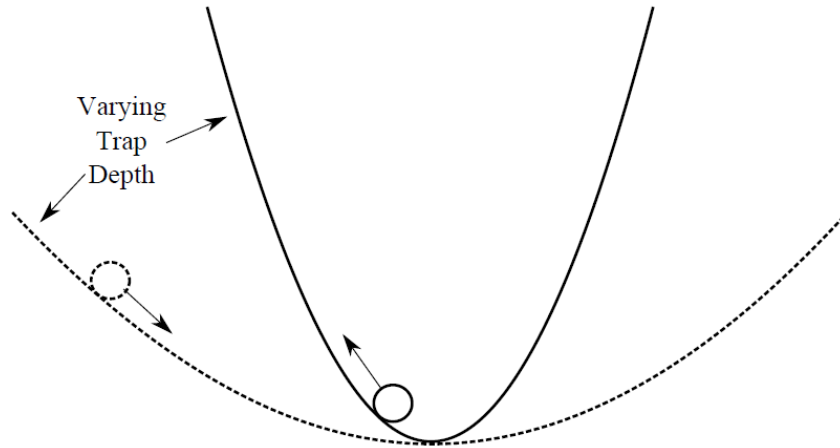


Figure 6.22: (Figure reproduced from ref. [140].) Parametric feedback cooling works by varying the trap depth depending on the sphere's position.

by modulating the optical trap's stiffness at twice the trap frequency: increasing it whenever the sphere moves away from the trap center, and reducing it as the sphere moves back to the center (figure 6.22) [125]. As can be seen from equations 4.21 and 4.22, the trap stiffness can be modulated by changing the trap laser's intensity, this can be done using an Electro-Optical Modulator (EOM) which is a device that uses the electro-optical effect for this purpose: applying an electric field to a nonlinear crystal, modifies its refractive index, which can be used to control the phase, polarization or power of a laser going through the crystal. Figure 6.23 shows a simplified diagram of the feedback cooling circuitry.



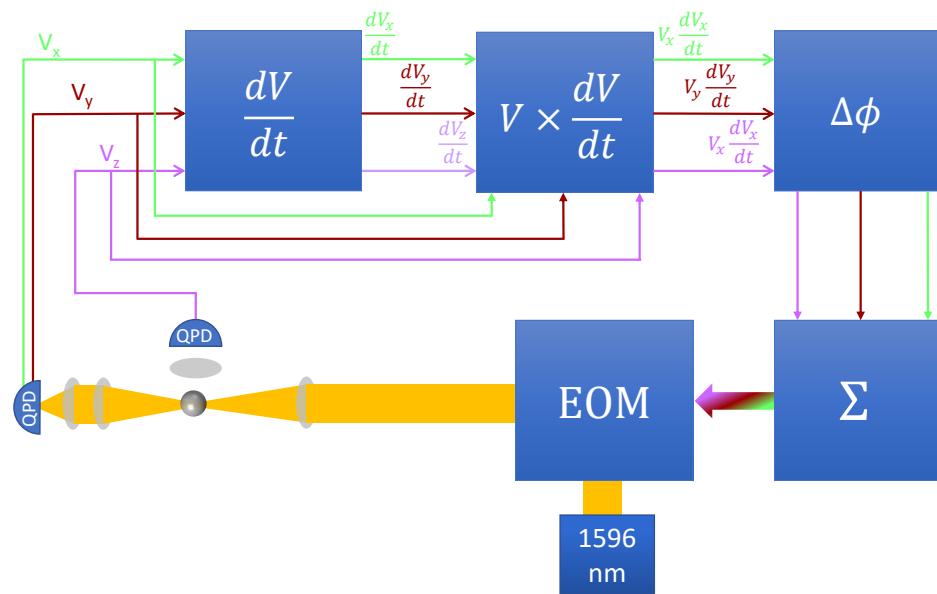


Figure 6.23: (Adapted from ref. [143].) Parametric feedback cooling diagram. Quadrant photodetectors produce a velocity dependent signal. Each of the signals from the photodetectors is processed through a derivative circuit, a multiplier circuit and a phase shifting circuit. All 3 processed signals are summed and fed to an EOM to modify the power of the laser.

## CHAPTER 7

### FUTURE OUTLOOK

In the field of precision sensing, cooled levitated spheres have been proposed for studying gravitational waves [144], where a cooled levitated particle inside a medium-finesse cavity is used for detection at the 50-300 kHz frequency range which is not limited to photon shot noise. The levitated particle's isolation from the thermal bath, robust decoupling from internal vibrations, and lack of clamping mechanism result in a very high mechanical quality factor [145]. This allows levitated particles to be used as a sensing tool for short range forces. Measurement times of  $10^5$  s, and force sensitivity of  $10^{-21}$  N have been reported when using levitated silica spheres, which could be used for measurement of gravitational forces [52], and Coulomb forces [124]. Geraci and Goldman [146] recently proposed that by using ground-state cooled levitated spheres, acceleration sensing at the  $10^{-8} m/s^2$  level is possible. In their proposed matter-wave interference setup, illustrated in figure 7.1, the cooled sphere interacts with a mass as it is dropped nearby. By recording the position of the sphere after it falls in repeated experiments, an interference pattern is created which will vary if the density of the test mass is changed, as this will change the gravitational acceleration between the mass and the sphere. Such an experiment could be used to perform searches for Yukawa type potentials at the  $5 \mu m$  level scale.

As a way of improving sensitivity, recent research has been devoted to squeezing of mechanical oscillators [147, 148], where the oscillator is at the limit of the Heisenberg uncertainty principle; i.e.,  $\Delta x \Delta p = \hbar/2$ . A classical analog of this effect was first reported by Rugar and Grütter in 1991 [149] where the thermal noise (Brownian motion) of a cantilever was reduced below the usual thermal equilibrium value. Quantum squeezing of mechanical oscillators has already been achieved [150, 151],

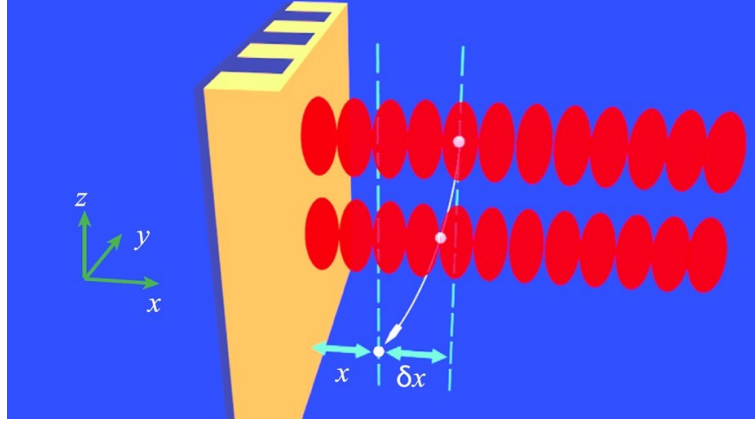


Figure 7.1: (Figure reproduced from ref. [146].) Illustration of matter-wave interference experiment proposed by Geraci and Goldman for short range sensing. A ground-state cooled levitated nanosphere is dropped near a mass. After some time, a light grating is applied. Measurements of the sphere's final position reveal an interference pattern dependent on the acceleration due to gravitational interaction with the nearby mass.

and a squeezing technique has been demonstrated which could be used in pre-cooled levitated optomechanics [152].

Coupling the sphere to internal states of atoms [54] could allow projecting the atoms-sphere system into an Einstein-Podolsky-Rosen (EPR) entangled state, which could be used for teleportation of collective spin states of the atom to the sphere [56].

To realize experiments of this kind, cooling of beads to the ground state must first be repeatably demonstrated. Sympathetic cooling via cold atoms expands the possible ways of reaching this, and because the sphere does not need to be pre-cooled, this setup is beneficial when cryogenic operation is not practical. An other practical advantage is the requirement of a medium-finesse cavity for this kind of experiment, as opposed to high-finesse cavities needed in cavity cooling. Sympathetic cooling also enables the possibility of ground state cooling of smaller spheres than cavity cooling, which is limited to spheres with a diameter of  $1\text{ }\mu\text{m}$  or larger [153]. Thermal contact

with the environment limits the isolation of the mechanical motion of an oscillator; levitated particles provide an improvement over other mechanical systems as they are mechanically isolated from the environment, providing long coherence times [154].

## APPENDIX A

### LABVIEW PROGRAM USED IN MAGNETIC COUPLING EXPERIMENT

To control the analog and digital signals on both the magnetic and the optical coupling experiments, a Labview virtual instrument (VI) is used. This program controls a sequence of events, each event lasting a different length of time. The program therefore has three parts: a state table that controls the analog outputs, a voltage table that controls the digital outputs, and a time table that sets the times for each event. In this appendix, a description of the sequence VI for the atoms magnetically coupled to a cantilever is provided.

#### A.1 State Table

The state table has the ability to control 16 analog outputs, but only the first 8 are used in our experiment:

1. MOT anti-helmholtz coils
2. (Not used)
3. Imaging shutter
4. Cooling beam shutter
5. Hyperfine depump beam shutter
6. Optical pumping shutter
7. Camera trigger
8. Analog output board trigger

## A.2 Time Table

The time table sets the duration of each event in milliseconds, with a precision of 0.1 ms.

## A.3 Voltage Table

15 digital signals are controlled with the voltage table. Each line on the voltage table corresponds to an event on the state table and time table. The outputs controlled are the following:

1. Detuning of the cooling beam (controlled via an AOM)
2. Detuning of the repump laser (controlled via an AOM)
3. Current on the P-wire
4. Current on the U-wire
5. Diagonal bias field
6. East-west bias field
7. Vertical bias field
8. South anti-helmholtz coil
9. Guide wire
10. Guide wire
11. North anti-helmholtz coil
12. Detuning of the hyperfine depump beam (controlled via an AOM)
13. Amplitude of the hyperfine depump beam (controlled via an AOM)
14. (Not used)
15. Amplitude of the cooling beam (controlled via an AOM)

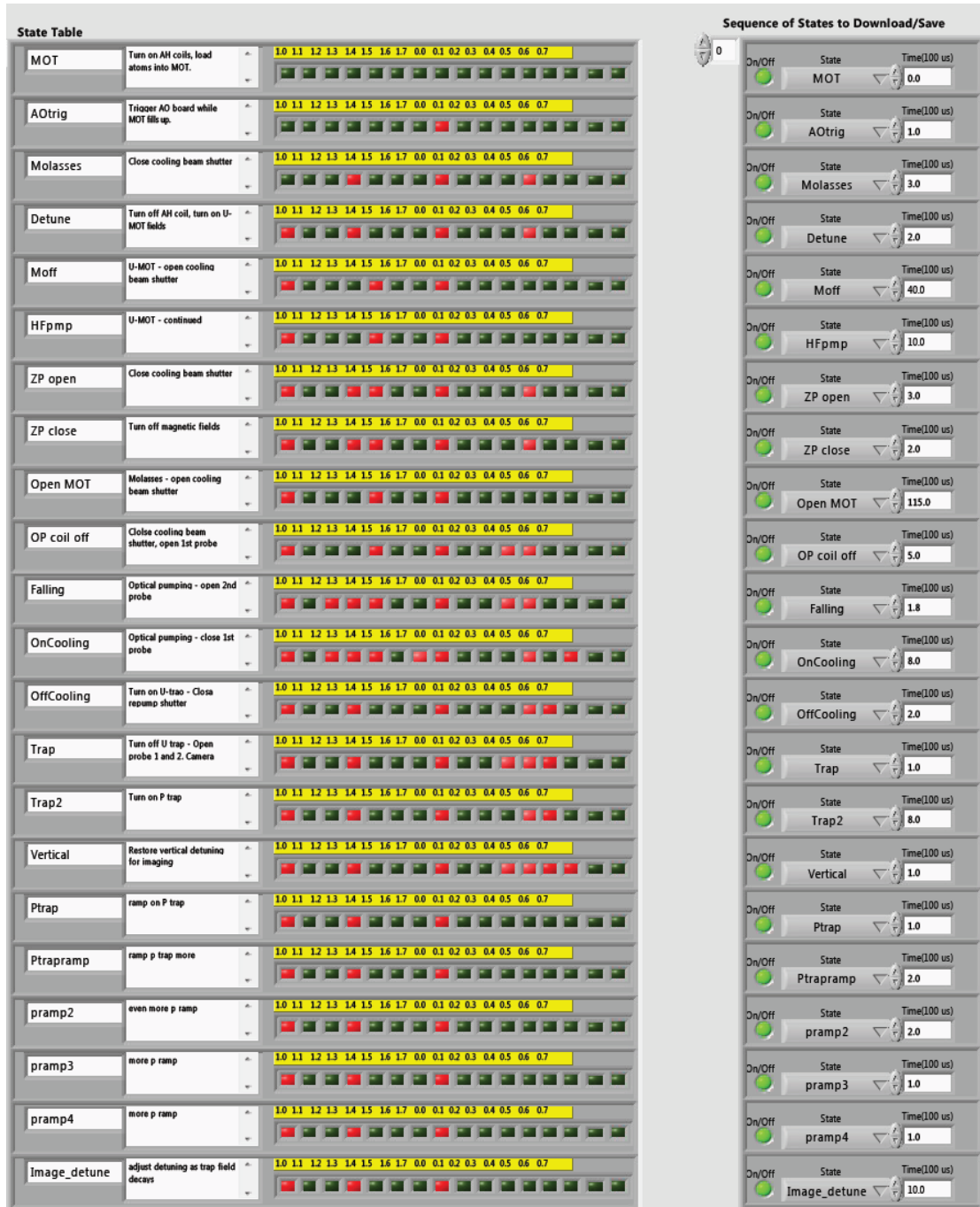


Figure A.1: Sequence state table and time table. Each column corresponds to a different analog output.



Figure A.2: Sequence state table and time table. Each column corresponds to a different analog output.



	Trap laser detuning	Repump detuning	P-wire 1v=0.9a	U-wire	Diagonal bias1	EW bias	Vertical bias	S AH	Guide Wires (1,2)	N AH	HF pump detuning	HF pump AMPL	dead	Trap laser AMPL	
0	4.1	5.86	0	0	-0.147	-0.015	-0.185	0	0	0	2.28	0	0	1.04	
0	1.8	5.86	0	0	-0.147	-0.015	-0.185	0	0	0	2.28	0	0	1.04	
	1.8	5.86	0	-0.4	0.043	-0.04	-0.22	0	0	0	2.28	0	0	1.04	
	4	5.86	0	-0.4	0.043	-0.04	-0.22	0	0	0	2.28	0	0	1.04	
	4	3.25	0	-0.4	0.043	-0.04	-0.22	0	0	0	2.28	0	0	1.04	
	1.8	3.25	0	-0.4	0.043	-0.04	-0.22	0	0	0	2.28	0	0	1.04	
	1.8	5.86	0	0	-0.045	-0.04	-0.09	0	0	0	2.28	0	0	1.04	
	1.8	5.86	0	0	-0.045	-0.04	-0.09	0	0	0	2.28	0	0	1.04	
Op coil off	1.8	5.86	0	0	-0.045	-0.04	-0.09	0	0	0	2.28	0	0	1.04	
	1.8	5.86	0	0	-0.045	-0.04	-0.09	0	0	0	2.28	0	0	1.04	
	5.4	5.86	0	0	-0.045	-0.04	-0.09	0	0	0	2.28	0	0	1.04	
	1.8	5.86	0	0	0.705	-0.04	-0.65	0	0	0	2.28	0	0	1.04	
	1.8	5.86	0	-0.8	0.553	-0.04	-0.52	0	0	0	2.28	0	0	1.04	
Trap2	1.8	5.86	0	-0.8	0.324	-0.04	-0.32	0	0	0	2.28	0	0	1.04	
	1.8	5.86	0	-0.75	0.324	-0.04	-0.32	0	0	0	2.28	0	0	1.04	
	1.8	5.86	0	-0.7	0.324	-0.04	-0.32	0	0	0	2.28	0	0	1.04	
	1.8	5.86	0	-0.65	0.324	-0.04	-0.32	0	0	0	2.28	0	0	1.04	
	1.8	5.86	0	-0.6	0.324	-0.04	-0.32	0	0	0	2.28	0	0	1.04	
pramp3	1.8	1	3	-0.4	0.324	-0.02	-0.313	0	-0.018	-0.018	2.28	0	0	0	
	1.8	1	3	-0.2	0.324	-0.02	-0.306	0	-0.018	-0.018	2.28	0	0	0	
	1.8	1	3	0	0.324	-0.02	-0.3	0	-0.018	-0.018	2.28	0	0	0	
Current ramp	1.8	1	3	0	0.324	-0.02	-0.3	0	-0.018	-0.018	2.28	0	0	0	
	1.8	1	3	0	0.052	-0.7	-0.24	0	-0.018	-0.018	2.28	0	0	0	
Trap High	1.8	1	3	0	0.052	-0.7	-0.24	0	-0.018	-0.018	2.28	0	0	0	
	1.8	1	3	0	0.052	-0.7	-0.24	0	-0.018	-0.018	2.28	0	0	0	
	1.8	3.25	3	0	0.052	-0.7	-0.24	0	-0.018	-0.018	2.28	0	0	1.04	
	1.8	3.25	0	0	-0.043	-0.7	-0.07	0	0	0	2.28	0.5	0	0	
AH4	1.8	3.25	0	0	-0.043	-0.7	-0.07	0	0	0	2.28	0	0	0	
	5.4	3.25	0	0	-0.043	-0.7	-0.07	0	0	0	2.28	0	0	1.04	
	1.8	5.86	0	0	-0.043	-0.7	-0.07	0	0	0	2.28	0	0	0	
CurrentRamp2	1.8	1	0	0	-0.5	-0.7	0	0	0	0	2.28	0	0	0	
	1.8	1	0	0	-0.6	-0.7	0	0	0	0	2.28	0	0	0	
CurrentRamp3	1.8	1	0	0	-0.6	-0.7	0	-3.2	0.3	-0.3	-2.6	2.28	0	0	0
	1.8	1	0	0	-0.6	-0.7	0	0	0	0	2.28	0	0	0	
	1.8	1	0	0	-0.6	-0.7	0	0	0	0	2.28	0	0	0	
AH3	1.8	1	0	0	-0.043	-0.06	-0.07	0	0	0	2.28	0	0	0	
	1.8	1	0	0	-0.043	-0.06	-0.07	0	0	0	2.28	0	0	0	
	1.8	1	0	0	-0.043	-0.06	-0.07	0	0	0	2.28	0	0	0	
	1.8	1	0	0	-0.043	-0.06	-0.07	0	0	0	2.28	0	0	0	
	4.1	5.86	0	0	-0.147	-0.015	-0.185	0	0	0	2.28	0	0	1.04	

Figure A.3: Sequence voltage table. Each column corresponds to a different digital output. Each line on the voltage table corresponds to a line in the sequence table.

## APPENDIX B

### MINIMUM DETECTABLE FORCE OF A HARMONIC OSCILLATOR

A mechanical oscillator in a thermal bath will receive random collisions from the surrounding gas. When the mechanical oscillator is used as a force sensor, these thermal fluctuations limit its sensitivity.

#### B.0.1 Cantilever Response

The equation of motion for a cantilever with mass  $m$ , and spring constant  $k$  is given by

$$\ddot{x} + \gamma\dot{x} + \omega_0^2 x = \frac{F(t)}{m} \quad (\text{B.1})$$

where  $F(t)$  is the force applied on the cantilever, and  $\gamma$  is the damping coefficient, and  $\omega_0 = \sqrt{k/m}$  is the mechanical resonance frequency of the cantilever. For a harmonic driving force:  $F(t) = f_0 e^{-i\omega t}$ , the above equation can be rewritten as

$$\ddot{x} + \gamma\dot{x} + \omega_0^2 x = \frac{f_0 e^{-i\omega t}}{m} \quad (\text{B.2})$$

The cantilever's response is then

$$x(t) = x_0 e^{-i\omega t} \quad (\text{B.3})$$

substituting equation B.3 into B.2, we obtain

$$-\omega^2 x_0 e^{-i\omega t} - i\omega\gamma x_0 e^{-i\omega t} + \omega_0^2 x_0 e^{-i\omega t} = \frac{f_0 e^{-i\omega t}}{m}. \quad (\text{B.4})$$

The cantilever susceptibility is

$$\chi(\omega) = \frac{x}{f} = \frac{1}{m} \frac{1}{\omega_0^2 - \omega^2 - i\omega\gamma} \quad (\text{B.5})$$

$$|\chi(\omega)| = \frac{1}{m} \frac{1}{\sqrt{(\omega_0^2 - \omega^2)^2 + \omega^2 \omega_0^2 / Q}} \quad (\text{B.6})$$

where the substitution  $\gamma = \omega_0/Q$  was performed, and  $Q$  is the mechanical quality factor of the cantilever.

## B.0.2 Thermal Noise Limitation

The cantilever position fluctuations are given by

$$\langle x^2 \rangle = \frac{1}{k^2} \int_0^\infty S_x(f) df = \frac{1}{k^2} \int_0^\infty |\chi(f)|^2 S_F(f) df \quad (\text{B.7})$$

where  $S_x(f)$  and  $S_F(f)$  are the displacement and force spectral density, respectively.

Substituting equation B.6 into equation B.7 and performing the integral, we obtain

$$\langle x^2 \rangle = \frac{\pi Q f_0}{2k^2} S_F \quad (\text{B.8})$$

using  $x_{rms} = \sqrt{\langle x^2 \rangle}$ , this equation can be expressed as

$$S_F^{1/2} = \left( \frac{2}{\pi Q f_0} \right)^{1/2} k x_{rms}. \quad (\text{B.9})$$

From the equipartition theorem [155]

$$\frac{1}{2} k_B T = \frac{1}{2} k \langle x^2 \rangle \quad (\text{B.10})$$

where  $k_B$  is Boltzmann's constant. Substituting equation B.9 into B.10, and using  $f_0 = \omega_0/2\pi$ , we obtain

$$S_F^{1/2} = \left( \frac{4k k_B T}{Q \omega_0} \right)^{1/2}. \quad (\text{B.11})$$

The minimum detectable force in a bandwidth  $b$  is

$$F_{min} = \sqrt{S_F b} = \left( \frac{4k k_B T b}{Q \omega_0} \right)^{1/2}. \quad (\text{B.12})$$

As expected, this force is limited by the temperature, and the mechanical quality factor of the cantilever.

## APPENDIX C

### MATHEMATICA CODE USED TO NUMERICALLY CALCULATE FIELD FROM MAGNET

In section 3.5.1, the field produced by a magnet was derived by approximating the field as a dipole. This approximation is only valid at large distances compared to the size of the magnet. For a more realistic estimate, we numerically integrated over the magnet geometry, assuming a single domain [90]. The Mathematica code used was the following:

```

Φz = Simplify[
(FullSimplify[Integrate[1/Sqrt[(y-yp)^2+(x-(xx1-aa/2))^2+(z-
zp)^2],yp]]/.{yp->(yy1+bb/2)})
-(FullSimplify[Integrate[1/Sqrt[(y-yp)^2+(x-(xx1-aa/2))^2+(z-
zp)^2],yp]]/.{yp->(yy1-bb/2)})
];

```

```

Φzboth = Simplify[Φz-(Φz/.{aa->-aa})];

```

```

Φ=Simplify[
(Simplify[Integrate[Φzboth,zp]]/.{zp->zz1+cc/2})
-(Simplify[Integrate[Φzboth,zp]]/.{zp->zz1-cc/2})
];

```

```

M0 =1*4.5*10^4;

```

```

μ0=4*π*10^-7;

```

```

Bx=μ0*M0/4/π*D[Φ,x];

```

```

By=μ0*M0/4/π*D[Φ,y];

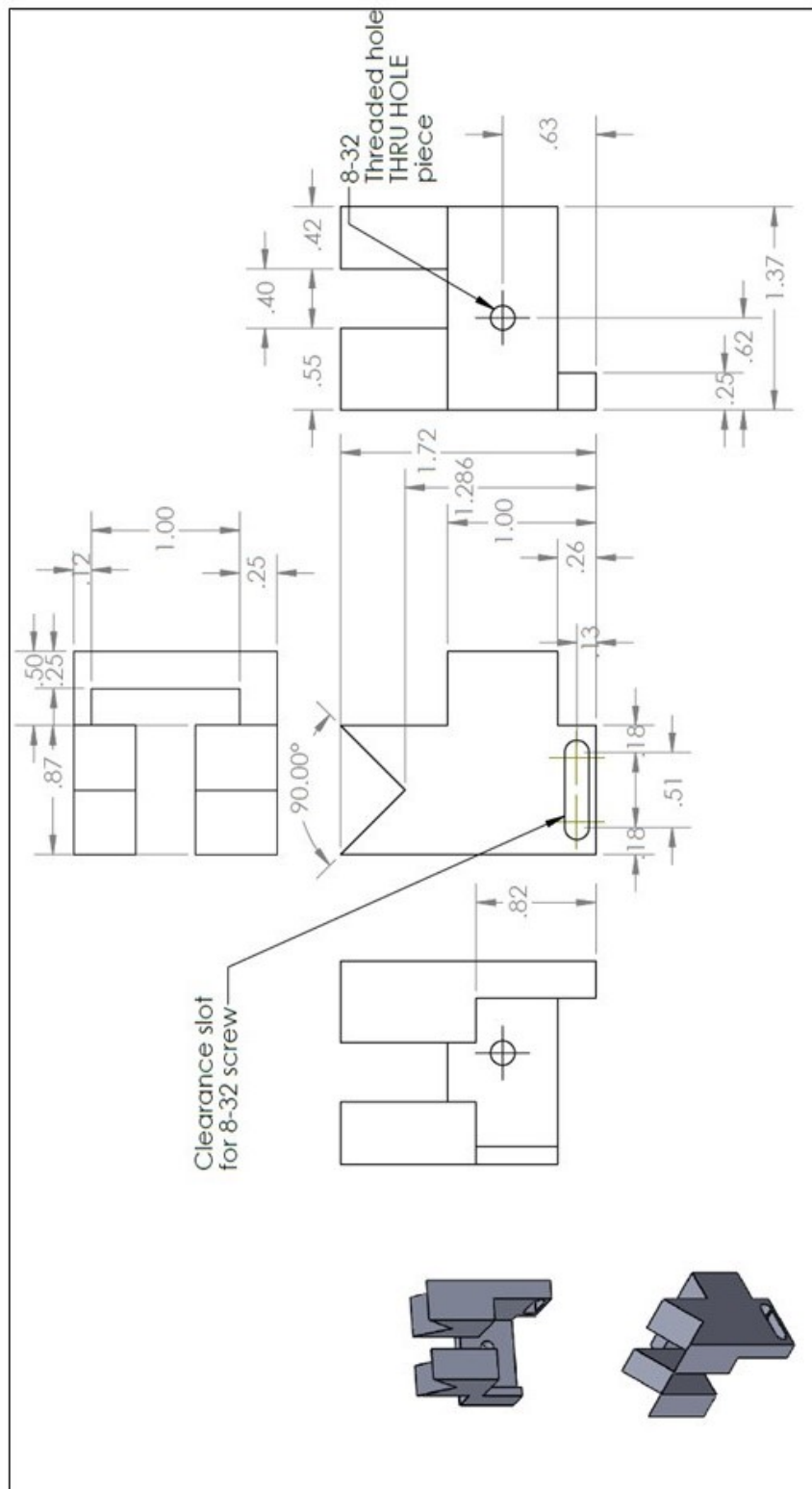
```

```

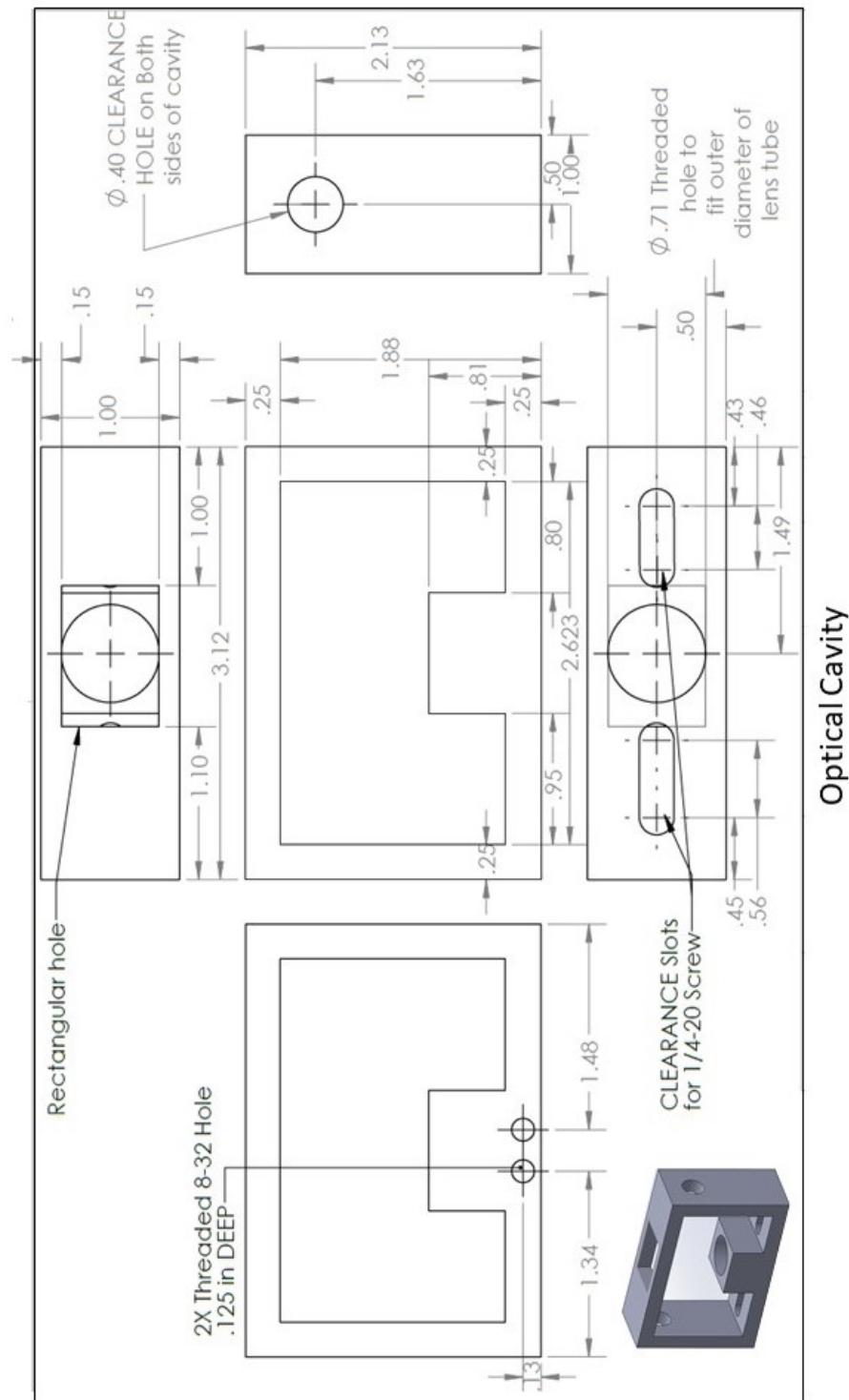
Bz=μ0*M0/4/π*D[Φ,z];

```

APPENDIX D  
OPTICAL CAVITY AND V-BLOCK DESIGN



V-Block





## APPENDIX E

### NANOFABRICATION OF CANTILEVER AND DRIVE MASS FOR GRAVITY EXPERIMENT

Experimental progress has been made to measure short-range forces using cooled optically levitated micro-spheres. As illustrated on E.1, in the ongoing experiment in our lab, a mass source, with periodical gold lines embedded in silicon is used. Near this surface, a silica micro-sphere is optically trapped. Gravity-like forces on the sphere due to the source mass can then be studied when the sphere is mostly interacting with the silicon or with the gold structure [145]. In this section, the fabrication of a cantilever and a drive mass for this short-range force experiment is discussed. Although it does not have an impact on the two projects discussed in this dissertation, this gravity experiment provides an example of an application of levitated spheres, and the fabrication steps are very similar to the ones used to fabricate the cantilever and the atom chip previously discussed.

#### E.1 Cantilever Fabrication

The drive mass will be oscillated by gluing it onto a capacitively driven cantilever at a resonance frequency determined by the physical dimensions of the cantilever. The cantilevers are made of silicon; to fabricate them we use silicon-on-insulator (SOI) wafers which have a layer of silicon dioxide buried in the wafer, the top layer of the SOI wafers set the height of the cantilever, the bottom layer sets the height of the handle. A layer of gold is evaporated onto the top of the finished cantilever to make its surface electrically conducting.

The fabrication of the cantilevers is divided into two processes: the front side of the wafer and the back side of the wafer, both processes are very similar and the

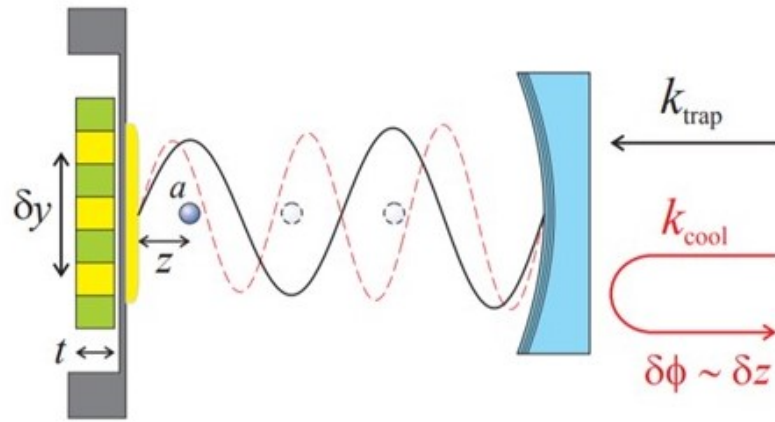


Figure E.1: (Adapted from ref. [145].) Geometry for a short-range force measurement experiment.

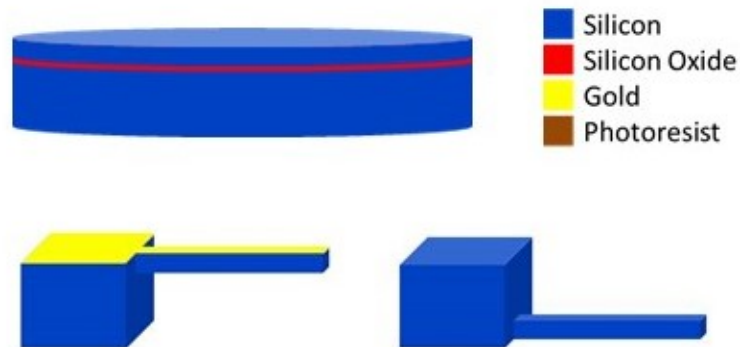


Figure E.2: The cantilevers are etched from a silicon-on-insulator substrate (Top left). (Bottom left) top view of cantilever coated with a layer of gold. (Bottom right) Bottom view of cantilever.

procedure is summarized as follows.

### E.1.1 Cantilever fabrication steps

#### Front Side

Step	Tool	Description
1	Wbclean	Clean wafers on SC1 and SC2 baths to eliminate organics and metals
2	YES oven	Dehydrates wafers and primes them to allow better adhesion between oxides and resist
3	SVGcoat	Coat front of wafer with 3 microns of SPR-220-3 resist. Let wafer sit on litho room for 12 hours before continuing
4	KarlSuss	Pattern wafers using front side mask
5	SVGDev	Develop patterned wafers
6	110 ° C Oven	Bake developed wafers for 30 minutes
7	STSetch	Etch front side of wafer until the front silicon is gone and the oxide is exposed
8	Gasonics	Remove resist from front side of wafer
9	Wbclean	Piranha clean wafers to remove resist residue followed by dump rinse and spin dry
10	Wbclean	Clean wafers on SC1 and SC2 baths to eliminate organics and metals
11	Tylanbpsg	Deposit oxide to protect front side of wafers from scratches during back side fabrication/manipulation

Table E.1: Fabrication steps for the front side of the cantilever.

## Back Side

Step	Tool	Description
12	AMTetch	Etch oxide from the back side of the wafer (but leave oxide on front)
13	YES oven	Dehydrates wafers and primes them to allow better adhesion between oxides and resist
14	SVGcoat	Coat back of wafer with 10 microns of SPR-220-7 resist. Most 10 micron coating recipes only bake wafer on hotplate for 100 s, if so bake wafer on hotplate for an additional 4 minutes. Let wafer sit on litho room for 24 hours before continuing
15	KarlSuss	Pattern wafers using back side mask
16	SVGDev	Develop patterned wafers
17	110 ° C Oven	Bake developed wafers for 30 minutes
18	STSetch	Etch back side of wafer until the back silicon is gone and the oxide is exposed
19	Wbclean	Etch oxide by dipping wafers into 6:1 BOE, followed by dump rinse. Dry wafers manually to prevent the cantilevers from falling off on the spin drier
20	Wbsolvent	Clean resist off cantilevers with acetone by individually spraying them, manually air dry cantilevers

Table E.2: Fabrication steps for the back side of the cantilever.

## Front Side

Step	Tool	Description
21	Innotec	Evaporate a binding layer of titanium onto front of cantilevers followed by a layer of gold

Table E.3: Final cantilever fabrication step.

## E.2 Drive Mass Fabrication

The drive mass is also fabricated on a silicon-on-insulator substrate where several masses are etched on a single wafer. The top silicon layer is 5  $\mu\text{m}$  thick which defines the depth of the gold pits, the bottom silicon layer is 500  $\mu\text{m}$  thick, and will be polished down to a few microns after the pits are filled with gold.

### E.2.1 Drive Mass Fabrication steps

#### Front Side

Step	Tool	Description
1	Wbclean	Clean wafers on SC1 and SC2 baths to eliminate organics and metals
2	Thermconitride	Coat wafers with silicon nitride to insulate the top of the trenches
3	YES oven	Dehydrates wafers and primes them to allow better adhesion between oxides and resist
4	SVGcoat	Coat front of wafer with 3 microns of SPR-220-3 resist. Let wafer sit on litho room for 12 hours before continuing
5	KarlSuss	Pattern wafers using front side mask
6	SVGDev	Develop patterned wafers
7	110 ° C Oven	Bake developed wafers for 30 minutes
8	Drytek2	Etch front side of silicon nitride until silicon is exposed
9	STSetch	Etch front side of wafer until the front silicon is gone and the oxide is exposed

Table E.4: Fabrication steps for the front side of drive mass.

## Back Side

Step	Tool	Description
10	SVGcoat	Coat back of wafer with 10 microns of SPR-220-7 resist. Do not bake on hotplate because the front side of the wafer still has resist
11	110 ° C Oven	Bake wafers for 1.5 hours in a cassette with resist side up, wafers must be horizontal so the resist doesn't fall out. Let wafer sit on litho room for 24 hours before continuing
12	KarlSuss	Pattern wafers using back side mask, soft contact
13	SVGDev	Develop patterned wafers
14	110 ° C Oven	Bake developed wafers for 30 minutes
15	Drytek2	Etch back side of silicon nitride until silicon is exposed
16	STSetch	Etch back side of wafer until the back silicon is gone and the oxide is exposed

Table E.5: Fabrication steps for the back side of drive mass.

## Front Side

Step	Tool	Description
17	Innotec	Evaporate a binding layer of titanium onto front of wafers followed by a layer of gold
18	Wbsolvent	Clean resist off masses by soaking wafer in acetone overnight, rinse with methanol

Table E.6: Final mass fabrication steps.

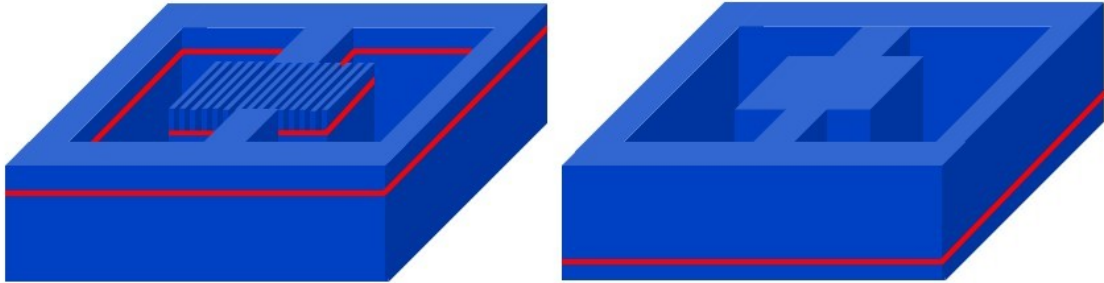


Figure E.3: Drive mass before gold coat. The red line represents the silicon dioxide buried layer. (Left) Front view of drive mass. (Right) Bottom view of drive mass.

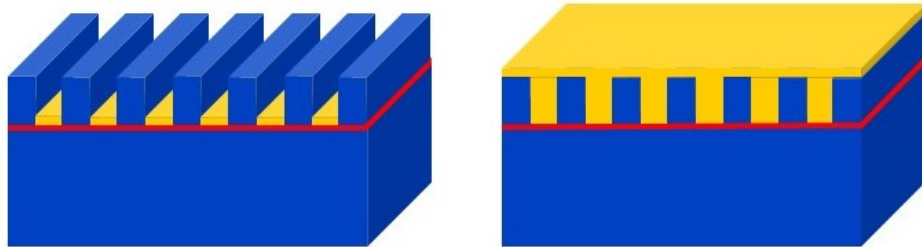


Figure E.4: (Left) Mass with evaporated gold on bottom of trenches. (Right) Electroplated mass.



## APPENDIX F

### ELECTROPLATING AND POLISHING OF DRIVE MASS

The masses for the gravity experiment are done at Stanford Nanofabrication Facility as described in section E.2. The last step of the process done at Stanford is evaporating a seed layer of gold on a titanium binding layer. The wafers are then transported to our lab where sections of it are scribed and gold is electroplated on them to fill the 5 micron trenches previously etched. After filling the trenches with gold, a polishing step must also be performed to obtain the desired mass thickness.

#### F.1 Electroplating

To electroplate gold, we use a cyanide-free gold plating solution (Technic Inc.: Elevate gold 7990). The process must be done under a fume hood and proper eye and skin protection must be worn.

##### F.1.1 Preparing the Samples

The wafers must be scribed into pieces with an area of about  $5 \text{ cm}^2$ . The top of the trenches have a layer of photoresist on them when the gold is evaporated; this allows removal of the gold everywhere, except for the bottom of the trenches, by soaking the wafer in acetone overnight. To remove any gold from the top of the trenches that did not get taken out during the acetone dip (figure F.1), the wafers must be sonicated for 10 minutes in acetone. If the top of the trenches have gold on them, gold will be electroplated at a faster rate near the top corner than at the bottom of the trenches. This will produce the trench to close prematurely leaving a void in the trenches as can be observed on figure F.1.

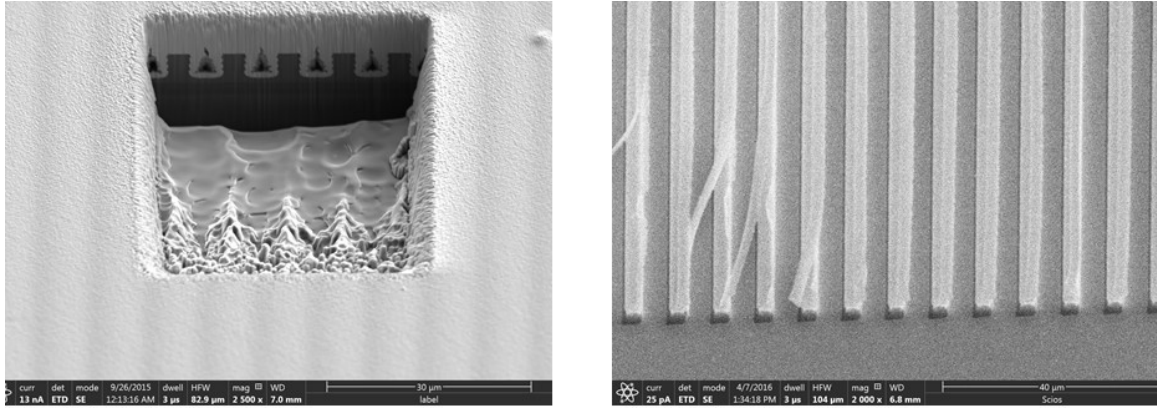


Figure F.1: SEM images of drive mass. (Left) Cross section of electroplated mass presenting voids inside the trenches. (Right) Mass before electroplating with leftover gold peeling from the top of the trenches, which is removed by sonicating the mass.

### F.1.2 Deposition Time Calculation

The gold solution we use, Elevate gold 7990, has a deposition rate of 122 mg/(A min). We usually run 0.004 A/cm<sup>2</sup>, following the recommended current density of 0.1-0.8 ASD (Amperes per square decimeter). From experience, we have learned that a slower current density yields a smoother finish. To calculate the deposition time, we first need to estimate the area of the sample to be gold coated, and then calculate the deposition current I

$$I = Ja \quad (\text{F.1})$$

where I is the deposition current in amperes (A), J is the current density in A/cm<sup>2</sup> (usually, 0.004 A/cm<sup>2</sup>), and a is the sample area in cm<sup>2</sup>.

The mass deposition rate is given by

$$k_m = k_s I \quad (\text{F.2})$$

where the mass deposition rate has units of mg/min, and the solution's deposition rate,  $k_s$  is in mg/(A min) (for our solution  $k_s = 122\text{mg}/(\text{Amin})$ ). The thickness

deposition rate is given by

$$k_t = \frac{k_m}{\rho a} \quad (\text{F.3})$$

where  $\rho$  is the density of gold ( $19.32 \text{ g/cm}^3$ ), and the thickness deposition rate,  $k_t$  has units of cm/min.

### F.1.3 Materials

1. Gold solution Elevate 7990
2. Platinum anode
3. Hot plate with magnetic stirring capability
4. Magnetic stirrer
5. Thermometer
6. Voltmeter
7. 2.5 V power supply
8. Two 500 ml beakers
9. Resistor
10. Plastic block
11. Vise
12. Di-ionized water
13. Lab coat
14. Lab safety goggles
15. Gloves
16. Watch
17. Chemical waste bucket

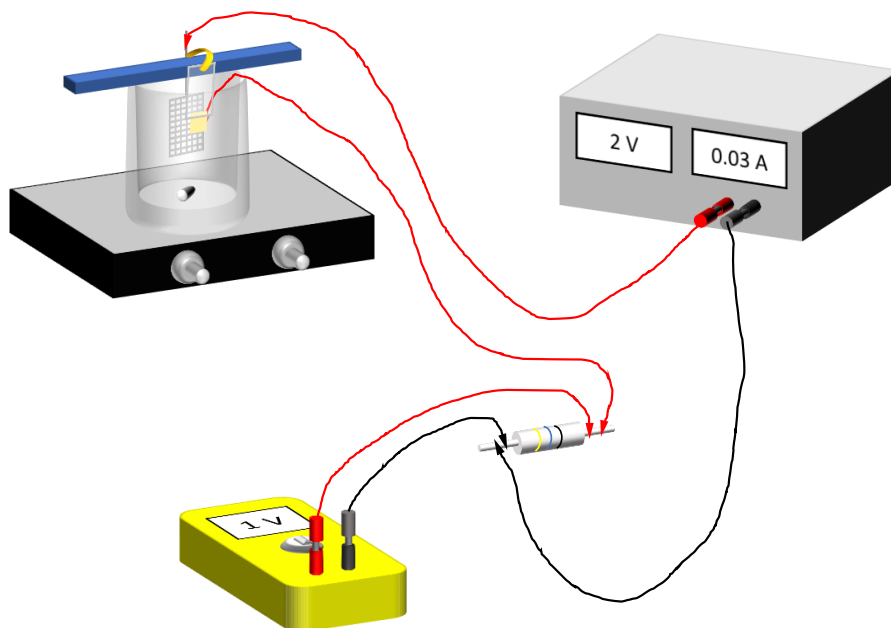


Figure F.2: Typical electroplating setup. A resistor is used to measure the voltage and monitor the current across it.

18. Kim wipes
19. Microscope glass slide
20. Kapton tape
21. Alligator clip wires

#### F.1.4 Procedure

Make sure to wear a lab coat, safety goggles and gloves at all time. Also, closed-toe shoes should be worn while electroplating. The gold solution leaves a black stain on fabrics. Make sure the connections have the right polarity; otherwise the gold might be stripped off the sample instead of deposited onto it. The following steps must be done under a fume hood.

1. With DI-water, rinse beakers, thermometer, anode, magnetic stirrer, plastic block, and microscope slide.
2. Use kapton tape to attach sample to a microscope glass slide.
3. Use vise to clamp anode to one side of plastic block and the glass slide on the opposite side of the block.
4. Place plastic block/anode/sample assembly on one of the beakers. Attach a wire to the top of the gold coated portion of the sample. Connect the other end of the wire to a (46 Ohm) resistor.
5. Connect a wire from the resistor to the negative output of the power supply.
6. Use an alligator clip to connect the anode to the positive terminal of the power supply.
7. Use a voltmeter to monitor the voltage drop across the (46 ohm) resistor.
8. Fill a beaker with 450 ml of gold solution. Put the beaker on a hot plate.
9. Put thermometer in the gold solution.
10. Turn the magnetic stirrer on (on the corning hotplate, we set the stirring to 6)
11. Slowly raise and monitor the temperature of the solution until 60 °C is reached (we start with the knob at the “3.5” mark). This step takes about 50 minutes.
12. When the temperature has stabilized to 60 °C, set the voltage on the power supply to about 1.0 V. Turn power supply on.
13. Insert anode/sample assembly into gold solution. Adjust the voltage on the power supply to match the desired current by monitoring the voltage drop across the resistor.
14. Monitor and adjust, if necessary, the solution’s temperature, it should remain around 60 °C.

15. After deposition, remove assembly from solution and place it on a beaker. Turn power supply off.
16. Turn off hotplate and stirrer.
17. Wait for solution to cool down to less than 30 °C. Return excess solution back into bottle.
18. Use DI water to rinse on a beaker all of the equipment that came in contact with gold solution including the sample.
19. Dump the water used to rinse the equipment into the chemical waste bucket.
20. Rinse equipment with isopropanol and wrap it in aluminum foil to keep it clean.

## F.2 Polishing of Drive Mass

The final mass has a thickness of 500  $\mu\text{m}$  of silicon, 5  $\mu\text{m}$  of silicon/gold pattern, and additional electroplated gold, as illustrated in figure F.3.

To obtain a 1-3  $\mu\text{m}$  smooth layer of silicon above the gold/silicon trenches, the underlaying silicon is polished. After polishing, the silicon must be coated with gold to provide electrostatic shielding for the gravity experiment.

### F.2.1 Materials

1. Indicator
2. Diamond scribe
3. Diamond file
4. Polisher
5. Di-ionized water

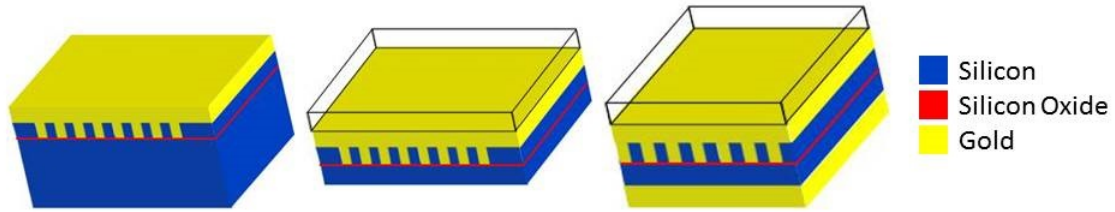


Figure F.3: Representation of drive mass. From left to right: Drive mass before polishing, polished drive mass with glass attached to it for structural support, polished drive mass with gold evaporated onto it.

6. Lab wipes
7. Polishing pads
8. Polishing solution
9. Wax
10. Hotplate

## F.2.2 Procedure

### Preparing the samples

1. Using a diamond scribe, cut 5 “pieces”, each containing one gold coated source mass. These pieces must be smaller than  $1\text{ cm} \times 1\text{ cm}$ .
2. Using an indicator with an accuracy of  $2.5\text{ }\mu\text{m}$ , measure the height of the silicon piece (silicon + gold).
3. Using indicator, measure the height of a previously cut  $1\text{ cm} \times 1\text{ cm}$  glass square. The glass squares are obtained by cutting a 500 microns thick quartz wafer using a wafer saw.
4. Epoxy gold-side of the piece to glass square using 353ND epoxy.

5. Using indicator, measure silicon + epoxy + glass.
6. Using indicator, measure the polishing puck's height at the different spots where the pieces will be placed.
7. Use wax to attach glass side of pieces to polishing puck. Attach a piece of Kapton tape to puck before waxing; take tape out after wax has hardened to keep an area of the puck without wax. Measure height of clean area, then "zero" the indicator at clean area.
8. Using indicator, measure silicon + epoxy + glass + wax + puck combo. Each piece should have its own combo measurement.
9. Subtract clean height from combo measurement since all of the following measurements will be done referenced from this height. Subtract silicon height too, this is the background for each piece = epoxy + glass + wax + (puck - clean height). To find out height of silicon, measure the height from clean area to top of silicon and subtract background. Each piece should have its own background.
10. Use a diamond file to bevel the edges of each piece, this will prevent chipping of the silicon. There is no need (and in practice it is too difficult!) to file the edges of the mass itself or the frame around the mass.

## Polishing

To perform the polishing, we have purchased pads from [www.metallographic.com](http://www.metallographic.com). The pads we have used are Polypad (Catalog number: PP-6008) for the 9  $\mu\text{m}$  suspension and Goldpad (Catalog number: GP-4008) for 6 and 3  $\mu\text{m}$  and for the colloidal silica.

The polishing solution we have used (purchased from [www.buehler.com](http://www.buehler.com)) is a diamond suspension MetaDi Ultra sold in a spray bottle. We have used 9  $\mu\text{m}$  (Part



number: 406533), 6  $\mu\text{m}$  (Part number: 406532), and 3  $\mu\text{m}$  (Part number: 406531) solutions.

1. Attach appropriate polishing pad to polishing plate.
2. Use deionized water to lubricate polishing pad.
3. Spray some polishing solution to pad.
4. Mount polishing puck onto spinning arm and lower it to pad.
5. Start polisher at lowest speed.
6. Periodically stop the polisher to measure how much silicon has been removed. Before and after measuring, rinse the pieces with DI water. Check the pieces for chipping or cracking and bevel the edges with a diamond file if needed. Rinse with DI water after beveling.
7. Take a note of the polishing speed. We have experienced speeds of about 64  $\mu\text{m}/\text{hour}$  with the 9  $\mu\text{m}$  solution and 30  $\mu\text{m}/\text{hour}$  with the 6  $\mu\text{m}$  solution. The 3  $\mu\text{m}$  solution is too slow and varies too much to determinate the polishing speed. Use the 9  $\mu\text{m}$  solution until about 50  $\mu\text{m}$  of silicon (omitting the gold layer and trenches which are usually 10 microns tall) are left or until pieces start cracking or breaking, whatever happens first. Use 6  $\mu\text{m}$  solution until about 20  $\mu\text{m}$  of silicon are left. The 3  $\mu\text{m}$  solution removes material slowly, stop frequently and measure until target height is reached. Sometimes, when using 3  $\mu\text{m}$  solution, very little silicon is removed so we can't determine, with the indicator, how much silicon is being removed. However, if the mass is looked at under a microscope differences can be noticed after each polishing run. In this case, polish the piece until the desired height using the 6  $\mu\text{m}$  solution. Use the 3  $\mu\text{m}$  solution to polish out the surface imperfections. Continue polishing

and periodically looking at mass under a microscope until polishing does not improve surface smoothness.

Polishing pad must be changed every time the diamond solution is changed. If an air bubble is left between the polishing plate and the pad, the pad might rip, avoid this by flattening the pad out with a piece of glass (we used a blank window) If pad tears, it must be changed.

8. Polish until about 50  $\mu\text{m}$  of silicon is left.
9. Unwax pieces from the polishing puck.
10. Look at mass in a scanning electron microscope at a 45 degree angle and determine how much silicon is left by measuring the height of one sidewall of the mass (multiply that measurement by  $\sqrt{2}$  to account for the angle). Before loading the mass onto the SEM, it must be sputter coated with gold or carbon to electrically ground all parts of it.
11. Wax piece back onto polishing puck.
12. Measure silicon + epoxy + glass + wax + (puck - clean height) and subtract remaining silicon as measured on SEM, this is the new calibrated background for this piece.
13. Continue polishing until desired height is reached. In most cases, each piece gets polished at different speeds, so while one piece might be at desired height, another one might not; stop when first piece is ready.
14. When 10  $\mu\text{m}$  of silicon is left, the pieces must be cut with a focused ion beam to study the cross section of the masses. This is a much more accurate measurement of the silicon left.
15. Continue polishing until 1-3  $\mu\text{m}$  of silicon is left.

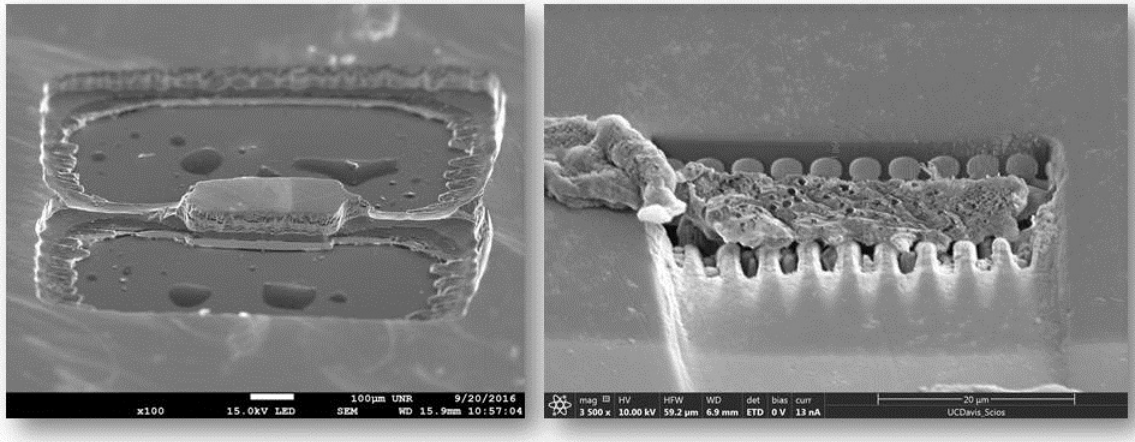


Figure F.4: Scanning electron microscope image of drive mass. (Left) Drive mass before being polished. (Right) Carved cross-section of the mass, where  $2\text{ }\mu\text{m}$  of silicon remain above the gold trenches.

16. Change pad to a Goldpad and use colloidal silica to finish smoothing the surface, this should only take about 10 minutes.

## BIBLIOGRAPHY

- [1] C. Montoya, J. Valencia, A. A. Geraci, M. Eardley, J. Moreland, L. Hollberg, and J. Kitching, “Resonant interaction of trapped cold atoms with a magnetic cantilever tip,” *Physical Review A*, vol. 91, p. 063835, June 2015.
- [2] G. Ranjit, C. Montoya, and A. A. Geraci, “Cold atoms as a coolant for levitated optomechanical systems,” *Physical Review A*, vol. 91, p. 013416, Jan. 2015.
- [3] L. Abdurakhimov, R. Yamashiro, A. Badrutdinov, and D. Konstantinov, “Strong Coupling of the Cyclotron Motion of Surface Electrons on Liquid Helium to a Microwave Cavity,” *Physical Review Letters*, vol. 117, p. 056803, July 2016.
- [4] M. Arndt and K. Hornberger, “Testing the limits of quantum mechanical superpositions,” *Nature Physics*, vol. 10, p. nphys2863, Apr. 2014.
- [5] G. t. Hooft, “Physics on the boundary between classical and quantum mechanics,” *Journal of Physics: Conference Series*, vol. 504, no. 1, p. 012003, 2014.
- [6] I. Katz, A. Retzker, R. Straub, and R. Lifshitz, “Signatures for a Classical to Quantum Transition of a Driven Nonlinear Nanomechanical Resonator,” *Physical Review Letters*, vol. 99, p. 040404, July 2007.
- [7] J. Raftery, D. Sadri, S. Schmidt, H. Türeci, and A. Houck, “Observation of a Dissipation-Induced Classical to Quantum Transition,” *Physical Review X*, vol. 4, p. 031043, Sept. 2014.
- [8] A. Blank, C. R. Dunnam, P. P. Borbat, and J. H. Freed, “High resolution electron spin resonance microscopy,” *Journal of Magnetic Resonance*, vol. 165, pp. 116–127, Nov. 2003.
- [9] S. Nimmrichter, K. Hornberger, and K. Hammerer, “Optomechanical Sensing of Spontaneous Wave-Function Collapse,” *Physical Review Letters*, vol. 113, p. 020405, July 2014.
- [10] D. Rugar, R. Budakian, H. J. Mamin, and B. W. Chui, “Single spin detection by magnetic resonance force microscopy,” *Nature*, vol. 430, p. nature02658, July 2004.
- [11] I. Katz, R. Lifshitz, A. Retzker, and R. Straub, “Classical to quantum transition of a driven nonlinear nanomechanical resonator,” *New Journal of Physics*, vol. 10, no. 12, p. 125023, 2008.

- [12] A. D. O’Connell, M. Hofheinz, M. Ansmann, R. C. Bialczak, M. Lenander, E. Lucero, M. Neeley, D. Sank, H. Wang, M. Weides, J. Wenner, J. M. Martinis, and A. N. Cleland, “Quantum ground state and single-phonon control of a mechanical resonator,” *Nature*, vol. 464, p. nature08967, Mar. 2010.
- [13] J. D. Teufel, T. Donner, D. Li, J. W. Harlow, M. S. Allman, K. Cicak, A. J. Sirois, J. D. Whittaker, K. W. Lehnert, and R. W. Simmonds, “Sideband cooling of micromechanical motion to the quantum ground state,” *Nature*, vol. 475, pp. 359–363, July 2011.
- [14] J. Chan, T. P. M. Alegre, A. H. Safavi-Naeini, J. T. Hill, A. Krause, S. Gröblacher, M. Aspelmeyer, and O. Painter, “Laser cooling of a nanomechanical oscillator into its quantum ground state,” *Nature*, vol. 478, pp. 89–92, Oct. 2011.
- [15] T. H. Maiman, “Stimulated Optical Radiation in Ruby,” *Nature*, vol. 187, p. 493, Aug. 1960.
- [16] A. Ashkin, “Acceleration and Trapping of Particles by Radiation Pressure,” *Physical Review Letters*, vol. 24, pp. 156–159, Jan. 1970.
- [17] S. Chu, J. E. Bjorkholm, A. Ashkin, and A. Cable, “Experimental Observation of Optically Trapped Atoms,” *Physical Review Letters*, vol. 57, pp. 314–317, July 1986.
- [18] A. L. Migdall, J. V. Prodan, W. D. Phillips, T. H. Bergeman, and H. J. Metcalf, “First Observation of Magnetically Trapped Neutral Atoms,” *Physical Review Letters*, vol. 54, pp. 2596–2599, June 1985.
- [19] “The Nobel Prize in Physics 1997.” Nobel-prize.org. Nobel Media AB 2014. Web. 24 Nov 2017. <[http://www.nobelprize.org/nobel\\_prizes/physics/laureates/1997/](http://www.nobelprize.org/nobel_prizes/physics/laureates/1997/)>.
- [20] M. H. Anderson, J. R. Ensher, M. R. Matthews, C. E. Wieman, and E. A. Cornell, “Observation of Bose-Einstein Condensation in a Dilute Atomic Vapor,” *Science*, vol. 269, pp. 198–201, July 1995.
- [21] T. P. Heavner, E. A. Donley, F. Levi, G. Costanzo, T. E. Parker, J. H. Shirley, N. Ashby, S. Barlow, and S. R. Jefferts, “First accuracy evaluation of NIST-F2,” *Metrologia*, vol. 51, no. 3, p. 174, 2014.

- [22] A. D. Ludlow, M. M. Boyd, J. Ye, E. Peik, and P. Schmidt, “Optical atomic clocks,” *Reviews of Modern Physics*, vol. 87, pp. 637–701, June 2015.
- [23] F. Marquardt and S. M. Girvin, “Trend: Optomechanics,” *Physics*, vol. 2, May 2009.
- [24] T. P. Purdy, P.-L. Yu, R. W. Peterson, N. S. Kampel, and C. A. Regal, “Strong Optomechanical Squeezing of Light,” *Physical Review X*, vol. 3, p. 031012, Sept. 2013.
- [25] M. Aspelmeyer, P. Meystre, and K. Schwab, “Quantum optomechanics,” *Physics Today*, vol. 65, pp. 29–35, July 2012.
- [26] C. M. Caves, “Quantum-Mechanical Radiation-Pressure Fluctuations in an Interferometer,” *Physical Review Letters*, vol. 45, pp. 75–79, July 1980.
- [27] V. B. Braginsky, Y. I. Vorontsov, and K. S. Thorne, “Quantum nondemolition measurements,” *Science (New York, N.Y.)*, vol. 209, pp. 547–557, Aug. 1980.
- [28] M. T. Jaekel and S. Reynaud, “Casimir force between partially transmitting mirrors,” *Journal de Physique I*, vol. 1, pp. 1395–1409, Oct. 1991.
- [29] A. F. Pace, M. J. Collett, and D. F. Walls, “Quantum limits in interferometric detection of gravitational radiation,” *Physical Review A*, vol. 47, pp. 3173–3189, Apr. 1993.
- [30] P. F. Cohadon, A. Heidmann, and M. Pinard, “Cooling of a Mirror by Radiation Pressure,” *Physical Review Letters*, vol. 83, pp. 3174–3177, Oct. 1999.
- [31] M. Poggio, C. L. Degen, H. J. Mamin, and D. Rugar, “Feedback Cooling of a Cantilever’s Fundamental Mode below 5 mK,” *Physical Review Letters*, vol. 99, p. 017201, July 2007.
- [32] R. Kanegae and Y. Kawamura, “Feedback damping of a microcantilever at room temperature to the minimum vibration amplitude limited by the noise level,” *Scientific Reports*, vol. 6, p. 27843, June 2016.
- [33] V. B. Braginsky, S. E. Strigin, and S. P. Vyatchanin, “Parametric oscillatory instability in Fabry–Perot interferometer,” *Physics Letters A*, vol. 287, pp. 331–338, Sept. 2001.

- [34] T. J. Kippenberg, H. Rokhsari, T. Carmon, A. Scherer, and K. J. Vahala, “Analysis of Radiation-Pressure Induced Mechanical Oscillation of an Optical Microcavity,” *Physical Review Letters*, vol. 95, p. 033901, July 2005.
- [35] H. Rokhsari, T. J. Kippenberg, T. Carmon, and K. J. Vahala, “Radiation-pressure-driven micro-mechanical oscillator,” *Optics Express*, vol. 13, pp. 5293–5301, July 2005.
- [36] T. Carmon, H. Rokhsari, L. Yang, T. J. Kippenberg, and K. J. Vahala, “Temporal Behavior of Radiation-Pressure-Induced Vibrations of an Optical Microcavity Phonon Mode,” *Physical Review Letters*, vol. 94, p. 223902, June 2005.
- [37] O. Arcizet, P.-F. Cohadon, T. Briant, M. Pinard, and A. Heidmann, “Radiation-pressure cooling and optomechanical instability of a micromirror,” *Nature*, vol. 444, pp. 71–74, Nov. 2006.
- [38] A. Zeilinger, D. Bäuerle, F. Blaser, G. Langer, H. R. Böhm, J. B. Hertzberg, K. C. Schwab, M. Aspelmeyer, M. Paternostro, and S. Gigan, “Self-cooling of a micromirror by radiation pressure,” *Nature*, vol. 444, p. 67, Nov. 2006.
- [39] M. Aspelmeyer, T. J. Kippenberg, and F. Marquardt, “Cavity optomechanics,” *Reviews of Modern Physics*, vol. 86, pp. 1391–1452, Dec. 2014.
- [40] A. Jöckel, A. Faber, T. Kampschulte, M. Korppi, M. T. Rakher, and P. Treutlein, “Sympathetic cooling of a membrane oscillator in a hybrid mechanical–atomic system,” *Nature Nanotechnology*, vol. 10, p. nnano.2014.278, Nov. 2014.
- [41] M. Karuza, C. Molinelli, M. Galassi, C. Biancofiore, R. Natali, P. Tombesi, G. D. Giuseppe, and D. Vitali, “Optomechanical sideband cooling of a thin membrane within a cavity,” *New Journal of Physics*, vol. 14, no. 9, p. 095015, 2012.
- [42] J. D. Thompson, B. M. Zwickl, A. M. Jayich, F. Marquardt, S. M. Girvin, and J. G. E. Harris, “Strong dispersive coupling of a high-finesse cavity to a micromechanical membrane,” *Nature*, vol. 452, pp. 72–75, Mar. 2008.
- [43] S. Ribeiro and H. Terças, “Sympathetic laser cooling of graphene with Casimir-Polder forces,” *Physical Review A*, vol. 94, p. 043420, Oct. 2016.
- [44] I. Favero, S. Stapfner, D. Hunger, P. Paulitschke, J. Reichel, H. Lorenz, E. M. Weig, and K. Karrai, “Fluctuating nanomechanical system in a high finesse optical microcavity,” *Optics Express*, vol. 17, pp. 12813–12820, July 2009.

- [45] O. Basarir, S. Bramhavar, and K. L. Ekinici, “Monolithic integration of a nanomechanical resonator to an optical microdisk cavity,” *Optics Express*, vol. 20, pp. 4272–4279, Feb. 2012.
- [46] C. Doolin, P. H. Kim, B. D. Hauer, A. J. R. MacDonald, and J. P. Davis, “Multidimensional optomechanical cantilevers for high-frequency force sensing,” *New Journal of Physics*, vol. 16, no. 3, p. 035001, 2014.
- [47] Y. Liu, H. Miao, V. Aksyuk, and K. Srinivasan, “Wide cantilever stiffness range cavity optomechanical sensors for atomic force microscopy,” *Optics Express*, vol. 20, pp. 18268–18280, July 2012.
- [48] D. Hunger, S. Camerer, T. W. Hänsch, D. König, J. P. Kotthaus, J. Reichel, and P. Treutlein, “Resonant Coupling of a Bose-Einstein Condensate to a Micromechanical Oscillator,” *Physical Review Letters*, vol. 104, p. 143002, Apr. 2010.
- [49] V. S. Ilchenko, M. L. Gorodetsky, X. S. Yao, and L. Maleki, “Microtorus: a high-finesse microcavity with whispering-gallery modes,” *Optics Letters*, vol. 26, pp. 256–258, Mar. 2001.
- [50] E. Verhagen, S. Deléglise, S. Weis, A. Schliesser, and T. J. Kippenberg, “Quantum-coherent coupling of a mechanical oscillator to an optical cavity mode,” *Nature*, vol. 482, p. nature10787, Feb. 2012.
- [51] P. Asenbaum, S. Kuhn, S. Nimmrichter, U. Sezer, and M. Arndt, “Cavity cooling of free silicon nanoparticles in high vacuum,” *Nature Communications*, vol. 4, p. ncomms3743, Nov. 2013.
- [52] G. Ranjit, M. Cunningham, K. Casey, and A. A. Geraci, “Zeptonewton force sensing with nanospheres in an optical lattice,” *Physical Review A*, vol. 93, p. 053801, May 2016.
- [53] Z.-q. Yin, T. Li, X. Zhang, and L. M. Duan, “Large quantum superpositions of a levitated nanodiamond through spin-optomechanical coupling,” *Physical Review A*, vol. 88, p. 033614, Sept. 2013.
- [54] F. Bariani, S. Singh, L. F. Buchmann, M. Vengalattore, and P. Meystre, “Hybrid optomechanical cooling by atomic lambda systems,” *Physical Review A*, vol. 90, p. 033838, Sept. 2014.
- [55] X. Chen, Y.-C. Liu, P. Peng, Y. Zhi, and Y.-F. Xiao, “Cooling of macroscopic



- mechanical resonators in hybrid atom-optomechanical systems,” *Physical Review A*, vol. 92, p. 033841, Sept. 2015.
- [56] K. Hammerer, M. Aspelmeyer, E. S. Polzik, and P. Zoller, “Establishing Einstein-Poldosky-Rosen Channels between Nanomechanics and Atomic Ensembles,” *Physical Review Letters*, vol. 102, p. 020501, Jan. 2009.
  - [57] F. Bariani, H. Seok, S. Singh, M. Vengalattore, and P. Meystre, “Atom-based coherent quantum-noise cancellation in optomechanics,” *Physical Review A*, vol. 92, p. 043817, Oct. 2015.
  - [58] Y.-J. Wang, M. Eardley, S. Knappe, J. Moreland, L. Hollberg, and J. Kitching, “Magnetic Resonance in an Atomic Vapor Excited by a Mechanical Resonator,” *Physical Review Letters*, vol. 97, p. 227602, Dec. 2006.
  - [59] A. Tretiakov and L. J. LeBlanc, “Magnetic-field-mediated coupling and control in hybrid atomic-nanomechanical systems,” *Physical Review A*, vol. 94, p. 043802, Oct. 2016.
  - [60] H. Metcalf and P. van der Straten, *Laser Cooling and Trapping*. Graduate Texts in Contemporary Physics, Springer New York, 2001.
  - [61] T. W. Hänsch and A. L. Schawlow, “Cooling of gases by laser radiation,” *Optics Communications*, vol. 13, pp. 68–69, Jan. 1975.
  - [62] D. J. Wineland and W. M. Itano, “Laser cooling of atoms,” *Physical Review A*, vol. 20, pp. 1521–1540, Oct. 1979.
  - [63] S. Chu, L. Hollberg, J. E. Bjorkholm, A. Cable, and A. Ashkin, “Three-dimensional viscous confinement and cooling of atoms by resonance radiation pressure,” *Physical Review Letters*, vol. 55, pp. 48–51, July 1985.
  - [64] C. Foot, *Atomic Physics*. Oxford Master Series in Physics, Oxford, New York: Oxford University Press, Feb. 2005.
  - [65] Y. Castin, H. Wallis, and J. Dalibard, “Limit of Doppler cooling,” *JOSA B*, vol. 6, pp. 2046–2057, Nov. 1989.
  - [66] D. A. Steck, “Rubidium 87 D line data,” Jan. 2015. Available online at <http://steck.us/alkalidata>.

- [67] J. Dalibard and C. Cohen-Tannoudji, “Laser cooling below the Doppler limit by polarization gradients: simple theoretical models,” *JOSA B*, vol. 6, pp. 2023–2045, Nov. 1989.
- [68] E. L. Raab, M. Prentiss, A. Cable, S. Chu, and D. E. Pritchard, “Trapping of Neutral Sodium Atoms with Radiation Pressure,” *Physical Review Letters*, vol. 59, pp. 2631–2634, Dec. 1987.
- [69] J. D. Weinstein and K. G. Libbrecht, “Microscopic magnetic traps for neutral atoms,” *Physical Review A*, vol. 52, pp. 4004–4009, Nov. 1995.
- [70] J. Reichel, W. Hänsel, and T. W. Hänsch, “Atomic Micromanipulation with Magnetic Surface Traps,” *Physical Review Letters*, vol. 83, pp. 3398–3401, Oct. 1999.
- [71] M. Keil, O. Amit, S. Zhou, D. Groswasser, Y. Japha, and R. Folman, “Fifteen Years of Cold Matter on the Atom Chip: Promise, Realizations, and Prospects,” *Journal of Modern Optics*, vol. 63, pp. 1840–1885, Oct. 2016. arXiv: 1605.04939.
- [72] W. Hänsel, P. Hommelhoff, T. W. Hänsch, and J. Reichel, “Bose–Einstein condensation on a microelectronic chip,” *Nature*, vol. 413, p. 35097032, Oct. 2001.
- [73] A. Kasper, S. Schneider, C. v. Hagen, M. Bartenstein, B. Engeser, T. Schumm, I. Bar-Joseph, R. Folman, L. Feenstra, and J. Schmiedmayer, “A Bose–Einstein condensate in a microtrap,” *Journal of Optics B: Quantum and Semiclassical Optics*, vol. 5, no. 2, p. S143, 2003.
- [74] Y.-j. Lin, I. Teper, C. Chin, and V. Vuletić, “Impact of the Casimir-Polder Potential and Johnson Noise on Bose-Einstein Condensate Stability Near Surfaces,” *Physical Review Letters*, vol. 92, p. 050404, Feb. 2004.
- [75] R. Folman, “Material science for quantum computing with atom chips,” *Quantum Information Processing*, vol. 10, p. 995, Dec. 2011.
- [76] P. Treutlein, A. Negretti, and T. Calarco, “Quantum Information Processing with Atom Chips,” in *Atom Chips* (J. Reichel and V. Vuletić, eds.), pp. 283–308, Wiley-VCH Verlag GmbH & Co. KGaA, 2011. DOI: 10.1002/9783527633357.ch9.
- [77] D. M. Harber, J. M. Obrecht, J. M. McGuirk, and E. A. Cornell, “Measurement of the Casimir-Polder force through center-of-mass oscillations of a Bose-Einstein condensate,” *Physical Review A*, vol. 72, p. 033610, Sept. 2005.

- [78] J. M. Obrecht, R. J. Wild, M. Antezza, L. P. Pitaevskii, S. Stringari, and E. A. Cornell, “Measurement of the Temperature Dependence of the Casimir-Polder Force,” *Physical Review Letters*, vol. 98, p. 063201, Feb. 2007.
- [79] J. Esteve, J.-B. Trebbia, T. Schumm, A. Aspect, C. I. Westbrook, and I. Bouchoule, “Observations of Density Fluctuations in an Elongated Bose Gas: Ideal Gas and Quasicondensate Regimes,” *Physical Review Letters*, vol. 96, p. 130403, Apr. 2006.
- [80] S. Hofferberth, I. Lesanovsky, B. Fischer, T. Schumm, and J. Schmiedmayer, “Non-equilibrium coherence dynamics in one-dimensional Bose gases,” *Nature*, vol. 449, pp. 324–327, Sept. 2007.
- [81] B. Rauer, P. Grišins, I. Mazets, T. Schweigler, W. Rohringer, R. Geiger, T. Langen, and J. Schmiedmayer, “Cooling of a One-Dimensional Bose Gas,” *Physical Review Letters*, vol. 116, p. 030402, Jan. 2016.
- [82] B. Yuen, I. J. M. Barr, J. P. Cotter, E. Butler, and E. A. Hinds, “Enhanced oscillation lifetime of a Bose–Einstein condensate in the 3d/1d crossover,” *New Journal of Physics*, vol. 17, no. 9, p. 093041, 2015.
- [83] J. Fortagh, A. Grossmann, C. Zimmermann, and T. W. Hänsch, “Miniaturized Wire Trap for Neutral Atoms,” *Physical Review Letters*, vol. 81, pp. 5310–5313, Dec. 1998.
- [84] R. Folman, P. Kruger, J. Schmiedmayer, J. Denschlag, and C. Henkel, “Microscopic atom optics: from wires to an atom chip,” arXiv:0805.2613 [quant-ph], May 2008. arXiv: 0805.2613.
- [85] A. A. Geraci and J. Kitching, “Ultracold mechanical resonators coupled to atoms in an optical lattice,” *Physical Review A*, vol. 80, p. 032317, Sept. 2009.
- [86] F. Steiger, “Radioactive Dating,” 1996. <http://chem.tufts.edu/science/FrankSteiger/radioact.>
- [87] M. Eardley, Unpublished. PhD Dissertation.
- [88] H. J. Cho and C. H. Ahn, “A bidirectional magnetic microactuator using electroplated permanent magnet arrays,” *Journal of Microelectromechanical Systems*, vol. 11, pp. 78–84, Feb. 2002.
- [89] D. J. Griffiths, *Introduction to Electrodynamics*. Prentice Hall, 1999.

- [90] J. D. Jackson, Classical electrodynamics. Wiley, Oct. 1975.
- [91] D. Zuro, “Measuring the motion of micro-scale objects using light.” Senior thesis, May 2013.
- [92] T. V. Roszhart, “The effect of thermoelastic internal friction on the  $Q$  of micromachined silicon resonators,” in IEEE 4th Technical Digest on Solid-State Sensor and Actuator Workshop, pp. 13–16, June 1990.
- [93] K. Y. Yasumura, T. D. Stowe, E. M. Chow, T. Pfafman, T. W. Kenny, B. C. Stipe, and D. Rugar, “Quality factors in micron- and submicron-thick cantilevers,” *Journal of Microelectromechanical Systems*, vol. 9, pp. 117–125, Mar. 2000.
- [94] J. R. Rubbmark, M. M. Kash, M. G. Littman, and D. Kleppner, “Dynamical effects at avoided level crossings: A study of the Landau-Zener effect using Rydberg atoms,” *Physical Review A*, vol. 23, pp. 3107–3117, June 1981.
- [95] C. Zener, “Non-Adiabatic Crossing of Energy Levels,” *Proceedings of the Royal Society of London. Series A, Containing Papers of a Mathematical and Physical Character*, vol. 137, no. 833, pp. 696–702, 1932.
- [96] C. K. Law and J. H. Eberly, “Arbitrary Control of a Quantum Electromagnetic Field,” *Physical Review Letters*, vol. 76, pp. 1055–1058, Feb. 1996.
- [97] P. Rabl, S. J. Kolkowitz, F. H. L. Koppens, J. G. E. Harris, P. Zoller, and M. D. Lukin, “A quantum spin transducer based on nanoelectromechanical resonator arrays,” *Nature Physics*, vol. 6, pp. 602–608, Aug. 2010.
- [98] C. A. Regal and K. W. Lehnert, “From cavity electromechanics to cavity optomechanics,” *Journal of Physics: Conference Series*, vol. 264, no. 1, p. 012025, 2011.
- [99] A. H. Safavi-Naeini and O. Painter, “Proposal for an optomechanical traveling wave phonon–photon translator,” *New Journal of Physics*, vol. 13, no. 1, p. 013017, 2011.
- [100] K. Stannigel, P. Rabl, A. S. Sørensen, P. Zoller, and M. D. Lukin, “Optomechanical Transducers for Long-Distance Quantum Communication,” *Physical Review Letters*, vol. 105, p. 220501, Nov. 2010.

- [101] J. C. Maxwell, *A Treatise on Electricity and Magnetism*. Clarendon Press, 1873. Google-Books-ID: 92QSAAAAIAAJ.
- [102] E. F. Nichols and G. F. Hull, “The Pressure Due to Radiation,” *Proceedings of the American Academy of Arts and Sciences*, vol. 38, no. 20, pp. 559–599, 1903.
- [103] P. W. Milonni and J. H. Eberly, *Laser Physics*. John Wiley & Sons, Apr. 2010.
- [104] A. E. Siegman, *Lasers*. University Science Books, 1986.
- [105] A. Ashkin, J. M. Dziedzic, J. E. Bjorkholm, and S. Chu, “Observation of a single-beam gradient force optical trap for dielectric particles,” *Optics Letters*, vol. 11, pp. 288–290, May 1986.
- [106] W. H. Wright, G. J. Sonek, Y. Tadir, and M. W. Berns, “Laser trapping in cell biology,” *IEEE Journal of Quantum Electronics*, vol. 26, pp. 2148–2157, Dec. 1990.
- [107] A. Ashkin and J. M. Dziedzic, “Optical trapping and manipulation of viruses and bacteria,” *Science (New York, N.Y.)*, vol. 235, pp. 1517–1520, Mar. 1987.
- [108] Y. Tadir, W. H. Wright, O. Vafa, T. Ord, R. H. Asch, and M. W. Berns, “Micromanipulation of sperm by a laser generated optical trap,” *Fertility and Sterility*, vol. 52, pp. 870–873, Nov. 1989.
- [109] A. Ashkin, “Optical trapping and manipulation of neutral particles using lasers,” *Proceedings of the National Academy of Sciences*, vol. 94, pp. 4853–4860, May 1997.
- [110] Y. Harada and T. Asakura, “Radiation forces on a dielectric sphere in the Rayleigh scattering regime,” *Optics Communications*, vol. 124, pp. 529–541, Mar. 1996.
- [111] A. Faber, *Sympathetic cooling and self-oscillations in a hybrid atom-membrane system*. PhD Dissertation, Basel University, 2016.
- [112] M. Greiner, *Ultracold quantum gases in three-dimensional optical lattice potentials*. PhD Dissertation, München, University, 2003.
- [113] C. Genes, D. Vitali, P. Tombesi, S. Gigan, and M. Aspelmeyer, “Ground-state cooling of a micromechanical oscillator: Comparing cold damping and cavity-assisted cooling schemes,” *Physical Review A*, vol. 77, p. 033804, Mar. 2008.

- [114] K. W. Murch, K. L. Moore, S. Gupta, and D. M. Stamper-Kurn, “Observation of quantum-measurement backaction with an ultracold atomic gas,” *Nature Physics*, vol. 4, pp. 561–564, July 2008.
- [115] A. Naik, O. Buu, M. D. LaHaye, A. D. Armour, A. A. Clerk, M. P. Blencowe, and K. C. Schwab, “Cooling a nanomechanical resonator with quantum back-action,” *Nature*, vol. 443, pp. 193–196, Sept. 2006.
- [116] A. Schliesser, R. Rivière, G. Anetsberger, O. Arcizet, and T. J. Kippenberg, “Resolved-sideband cooling of a micromechanical oscillator,” *Nature Physics*, vol. 4, pp. 415–419, May 2008.
- [117] K. Hornberger, S. Uttenthaler, B. Brezger, L. Hackermüller, M. Arndt, and A. Zeilinger, “Collisional Decoherence Observed in Matter Wave Interferometry,” *Physical Review Letters*, vol. 90, p. 160401, Apr. 2003.
- [118] O. Romero-Isart, A. C. Pflanzer, F. Blaser, R. Kaltenbaek, N. Kiesel, M. Aspelmeyer, and J. I. Cirac, “Large Quantum Superpositions and Interference of Massive Nanometer-Sized Objects,” *Physical Review Letters*, vol. 107, p. 020405, July 2011.
- [119] S. Felicetti, S. Fedortchenko, R. Rossi, S. Ducci, I. Favero, T. Coudreau, and P. Milman, “Quantum communication between remote mechanical resonators,” *Physical Review A*, vol. 95, p. 022322, Feb. 2017.
- [120] F.-Y. Hong, J.-L. Fu, Y. Wu, and Z.-Y. Zhu, “Room-temperature spin-photon interface for quantum networks,” *Quantum Information Processing*, vol. 16, p. 43, Feb. 2017.
- [121] L. Tian and Z. Li, “Nonreciprocal quantum-state conversion between microwave and optical photons,” *Physical Review A*, vol. 96, p. 013808, July 2017.
- [122] B. Vogell, K. Stannigel, P. Zoller, K. Hammerer, M. T. Rakher, M. Korppi, A. Jöckel, and P. Treutlein, “Cavity-enhanced long-distance coupling of an atomic ensemble to a micromechanical membrane,” *Physical Review A*, vol. 87, p. 023816, Feb. 2013.
- [123] A. Ashkin and J. M. Dziedzic, “Optical levitation in high vacuum,” *Applied Physics Letters*, vol. 28, pp. 333–335, Mar. 1976.
- [124] D. Hempston, J. Vovrosh, M. Toroš, G. Winstone, M. Rashid, and H. Ul-

- bricht, “Force sensing with an optically levitated charged nanoparticle,” *Applied Physics Letters*, vol. 111, p. 133111, Sept. 2017.
- [125] J. Gieseler, B. Deutsch, R. Quidant, and L. Novotny, “Subkelvin Parametric Feedback Cooling of a Laser-Trapped Nanoparticle,” *Physical Review Letters*, vol. 109, p. 103603, Sept. 2012.
  - [126] S. Kuhn, B. A. Stickler, A. Kosloff, F. Patolsky, K. Hornberger, M. Arndt, and J. Millen, “Optically driven ultra-stable nanomechanical rotor,” *Nature Communications*, vol. 8, p. 1670, Nov. 2017.
  - [127] G. Raithel, W. D. Phillips, and S. L. Rolston, “Collapse and Revivals of Wave Packets in Optical Lattices,” *Physical Review Letters*, vol. 81, pp. 3615–3618, Oct. 1998.
  - [128] D. E. Chang, C. A. Regal, S. B. Papp, D. J. Wilson, J. Ye, O. Painter, H. J. Kimble, and P. Zoller, “Cavity opto-mechanics using an optically levitated nanosphere,” *Proceedings of the National Academy of Sciences*, vol. 107, pp. 1005–1010, Jan. 2010.
  - [129] R. Grimm, M. Weidemüller, and Y. B. Ovchinnikov, “Optical Dipole Traps for Neutral Atoms,” in *Advances In Atomic, Molecular, and Optical Physics* (B. Bederson and H. Walther, eds.), vol. 42, pp. 95–170, Academic Press, Jan. 2000. DOI: 10.1016/S1049-250X(08)60186-X.
  - [130] J. M. Dobrindt, I. Wilson-Rae, and T. J. Kippenberg, “Parametric Normal-Mode Splitting in Cavity Optomechanics,” *Physical Review Letters*, vol. 101, p. 263602, Dec. 2008.
  - [131] S. Gröblacher, K. Hammerer, M. R. Vanner, and M. Aspelmeyer, “Observation of strong coupling between a micromechanical resonator and an optical cavity field,” *Nature*, vol. 460, p. nature08171, Aug. 2009.
  - [132] S. Haroche, “Nobel Lecture: Controlling photons in a box and exploring the quantum to classical boundary,” *Reviews of Modern Physics*, vol. 85, pp. 1083–1102, July 2013.
  - [133] J. Millen, T. Deesuwan, P. Barker, and J. Anders, “Nanoscale temperature measurements using non-equilibrium Brownian dynamics of a levitated nanosphere,” *Nature Nanotechnology*, vol. 9, p. 425, June 2014.
  - [134] J. S. Bennett, L. S. Madsen, M. Baker, H. Rubinsztein-Dunlop, and W. P.

- Bowen, “Coherent control and feedback cooling in a remotely coupled hybrid atom–optomechanical system,” *New Journal of Physics*, vol. 16, no. 8, p. 083036, 2014.
- [135] E. C. Cook, P. J. Martin, T. L. Brown-Heft, J. C. Garman, and D. A. Steck, “High passive-stability diode-laser design for use in atomic-physics experiments,” *Review of Scientific Instruments*, vol. 83, p. 043101, Apr. 2012.
  - [136] A. Witherspoon, “A Method for Transferring Nanospheres from a Dipole Trap into an Optical Lattice.” Senior thesis, May 2017.
  - [137] B. K. Chen, Y. Zhang, and Y. Sun, “Active Release of Microobjects Using a MEMS Microgripper to Overcome Adhesion Forces,” *Journal of Microelectromechanical Systems*, vol. 18, pp. 652–659, June 2009.
  - [138] I. Rodriguez, “Manipulation of the Electric Charge on Optically Levitated Microspheres.” Senior thesis, May 2017.
  - [139] M. Beck, “Overcoming ”stiction” forces: Launching silica microspheres into an optical trap.” Senior thesis, May 2012.
  - [140] D. P. Atherton, Sensitive force measurements with optically trapped microspheres in high vacuum. PhD Dissertation, University of Nevada, Reno, 2015.
  - [141] “Molded Glass Aspheric Lenses: Uncoated,” tech. rep., Feb. 2010. [https://www.thorlabs.com/newgroup-page9.cfm?objectgroup\\_id=3809&pn=A240#3817](https://www.thorlabs.com/newgroup-page9.cfm?objectgroup_id=3809&pn=A240#3817).
  - [142] S. A. Beresnev, V. G. Chernyak, and G. A. Fomyagin, “Motion of a spherical particle in a rarefied gas. Part 2. Drag and thermal polarization,” *Journal of Fluid Mechanics*, vol. 219, pp. 405–421, Oct. 1990.
  - [143] J. Fausett, “Assembly and testing of a feedback system for parametric cooling of an optically trapped nano-sphere.” Senior thesis, May 2017.
  - [144] A. Arvanitaki and A. A. Geraci, “Detecting High-Frequency Gravitational Waves with Optically Levitated Sensors,” *Physical Review Letters*, vol. 110, p. 071105, Feb. 2013.
  - [145] A. A. Geraci, S. B. Papp, and J. Kitching, “Short-Range Force Detection Using Optically Cooled Levitated Microspheres,” *Physical Review Letters*, vol. 105, p. 101101, Aug. 2010.



- [146] A. Geraci and H. Goldman, “Sensing short range forces with a nanosphere matter-wave interferometer,” *Physical Review D*, vol. 92, p. 062002, Sept. 2015.
- [147] K. Jähne, C. Genes, K. Hammerer, M. Wallquist, E. S. Polzik, and P. Zoller, “Cavity-assisted squeezing of a mechanical oscillator,” *Physical Review A*, vol. 79, p. 063819, June 2009.
- [148] A. Pontin, M. Bonaldi, A. Borrielli, F. Cataliotti, F. Marino, G. Prodi, E. Serra, and F. Marin, “Squeezing a Thermal Mechanical Oscillator by Stabilized Parametric Effect on the Optical Spring,” *Physical Review Letters*, vol. 112, p. 023601, Jan. 2014.
- [149] D. Rugar and P. Grütter, “Mechanical parametric amplification and thermomechanical noise squeezing,” *Physical Review Letters*, vol. 67, pp. 699–702, Aug. 1991.
- [150] J.-M. Pirkkalainen, E. Damskägg, M. Brandt, F. Massel, and M. Sillanpää, “Squeezing of Quantum Noise of Motion in a Micromechanical Resonator,” *Physical Review Letters*, vol. 115, p. 243601, Dec. 2015.
- [151] E. E. Wollman, C. U. Lei, A. J. Weinstein, J. Suh, A. Kronwald, F. Marquardt, A. A. Clerk, and K. C. Schwab, “Quantum squeezing of motion in a mechanical resonator,” *Science*, vol. 349, pp. 952–955, Aug. 2015.
- [152] M. Rashid, T. Tufarelli, J. Bateman, J. Vovrosh, D. Hempston, M. Kim, and H. Ulbricht, “Experimental Realization of a Thermal Squeezed State of Levitated Optomechanics,” *Physical Review Letters*, vol. 117, p. 273601, Dec. 2016.
- [153] T. Li, Fundamental tests of physics with optically trapped microspheres. PhD Dissertation, University of Texas, Austin, May 2011.
- [154] O. Romero-Isart, A. C. Pflanzer, M. L. Juan, R. Quidant, N. Kiesel, M. Aspelmeyer, and J. I. Cirac, “Optically levitating dielectrics in the quantum regime: Theory and protocols,” *Physical Review A*, vol. 83, p. 013803, Jan. 2011.
- [155] K. Huang, *Statistical mechanics*. Wiley, 1987.